STEADY STATE PHOTOTHERMALIZATION AND HOT ELECTRON DYNAMICS IN NOBLE METALS

A Dissertation

by

NICKI LYNNE HOGAN

Submitted to the Office of Graduate and Professional Studies of
Texas A&M University
in partial fulfillment of the requirements for the degree of

DOCTOR OF PHILOSOPHY

Chair of Committee,	Matthew Sheldon
Committee Members,	Dong Hee Son
	James Batteas
	Christi Madsen
Head of Department,	Simon North

August 2020

Major Subject: Chemistry

ABSTRACT

There has been significant recent interest in using the resonant absorption in plasmonic nanostructures to produce transiently excited populations of photo-excited non-equilibrium hot electrons that can then be utilized in a variety of applications including photocatlysis and optoelectronic energy conversion. Traditional studies of these hot electrons are done using high power, pulsed excitation, though there is particular interest in being able to expand the current understanding to conditions of continuous wave excitation that may be more directly relevant to conditions used in emerging applications, such as solar fuel production.

I show that it is possible to systematically understand and control photothermalization in plasmonic materials by quantifying the connection between absorption, relaxation, and thermal emission. Using fundamental principles, the phononic temperature of a material can be predicted based on its absorption and emission properties, which then allows for optimization of the nanostructure geometry to maximize temperature for thermal applications. Increases in phononic temperature can in turn be used to inform the electronic temperature. By fitting to anti-Stokes Raman spectra, I develop a model that describes electrons in equilibrium with both the phononic and electronic temperature as well as giving a quantitative measure of the number of hot electrons. Additional analysis allows further insight into the hot electron dynamics inside the material including electron-phonon coupling and hot electron lifetime. Longer lifetimes increase the chance that hot electrons can be used in power cycles or chemical reactions.

Using this spectroscopic technique, I explore how the hot electron population in nanostructures is dependent on shape and material composition. Increased hot electron reactivity with surface species in copper is promising for photocatalytis. In contrast, gold nanostruc-

tures are less reactive and reached higher temperatures which has increased utility for solar-thermal applications. Further, variations in nanostructure geometry modified access of the hot electrons to the environment which changes not only the coupling constant but also the electronic temperature. This information opens opportunities for optimization of not only phononic temperature, but additionally rational design of nanostructures to have hot electrons with longer lifetimes or higher energies, properties which are extremely useful in developing hot electron technologies.

ACKNOWLEDGMENTS

First and foremost I would like to acknowledge everything my advisor, Matthew Sheldon, has done to help me grow during my time in the program. His endless optimism about results (even the negative, horribly inconsistent ones) kept me going through every experiment. The rest of the Sheldon group was just as important as well with all of our discussions in the office, both when we were procrastinating and when we talked science.

I'd also like to thank my undergraduate research advisor, Spencer Slattery, for his encouragement. He once told me grad school was a free adventure to explore science, and he was right.

I'd like to give special mention to my friends over the years, especially Benjamin Roman and Mary Phillips. Without that friendship, and the hobbies and distractions that they shared with me, I would not have made it through grad school nearly as sane as I did.

Perhaps most importantly, I would like to thank my parents, Lynne and William Hogan. Their endless support for my dreams and encouragement to always be the best I could be is what got me this far.

CONTRIBUTORS AND FUNDING SOURCES

Contributors

This work was supported by a dissertation committee consisting of chair Professor Matthew Sheldon from the Department of Chemistry and Department of Material Science & Engineering as well as Professor James Batteas of the Department of Chemistry and Department of Material Science & Engineering, Professor Dong Hee Son of the Department of Chemistry, and Professor Christi Madsen of the Department of Electrical & Computer Engineering.

Construction of thermionic power converters using my plasmonic nanostructure along with all corresponding electrical measurements in Chapters 3 and 4 were conducted by Shengxiang Wu, a fellow member of the Sheldon research group.

All other fabrication, measurement and calculation for the dissertation were completed independently.

Funding Sources

Research presented in this work was funded under grants from: the Air Force Office of Scientific Research (FA9550-16-1-0154), the Welch Foundataion (A-1886), and the Gordon and Betty Moore Foundataion (GBMF6882).

TABLE OF CONTENTS

Page

LIST OF FIGURES

FIGURE Page

1. INTRODUCTION

1.1 Introduction to Plasmons

One interesting phenomenon that can arise from the interaction of light with a surface is the generation of a plasmon. A plasmon is the bulk oscillation of the electron cloud inside a material in response to an external electric field. This occurs whenever there is a change in the sign of the real portion of the permittivity function at an interface, for example at the interface between a metal and a dielectric.[1] The exact wavelengths of light with which a plasmon can be excited is dependent on both the refractive index of the material as well as its physical geometry. When incident on a structure that is extremely sub-wavelength, a resonant electric field can cause the electron density to oscillate within the structure, shown in Figure 1.1a.[2] This resonant oscillation is a non-propagating phenomenon. Perhaps the simplest case of this is demonstrated in spherical metal nanoparticles which have a clearly defined peak in their absorption spectra corresponding to a plasmon mode called the localized surface plasmon resonance (LSPR).

In a film, however, the mode is no longer confined by the geometry and can instead propagate along the surface. This mode is called a surface plasmon polariton (SPP) and is schematically demonstrated in Figure 1.1b.[2] Exciting a SPP on a flat surface is made difficult by a momentum mismatch between free space light and the plasmon modes in the film. This can be understood by considering the dispersion relation for both. Free space light obeys

$$\omega = ck_x \tag{1.1}$$

where ω is the angular frequency as a function of the wave vector in a given direction,

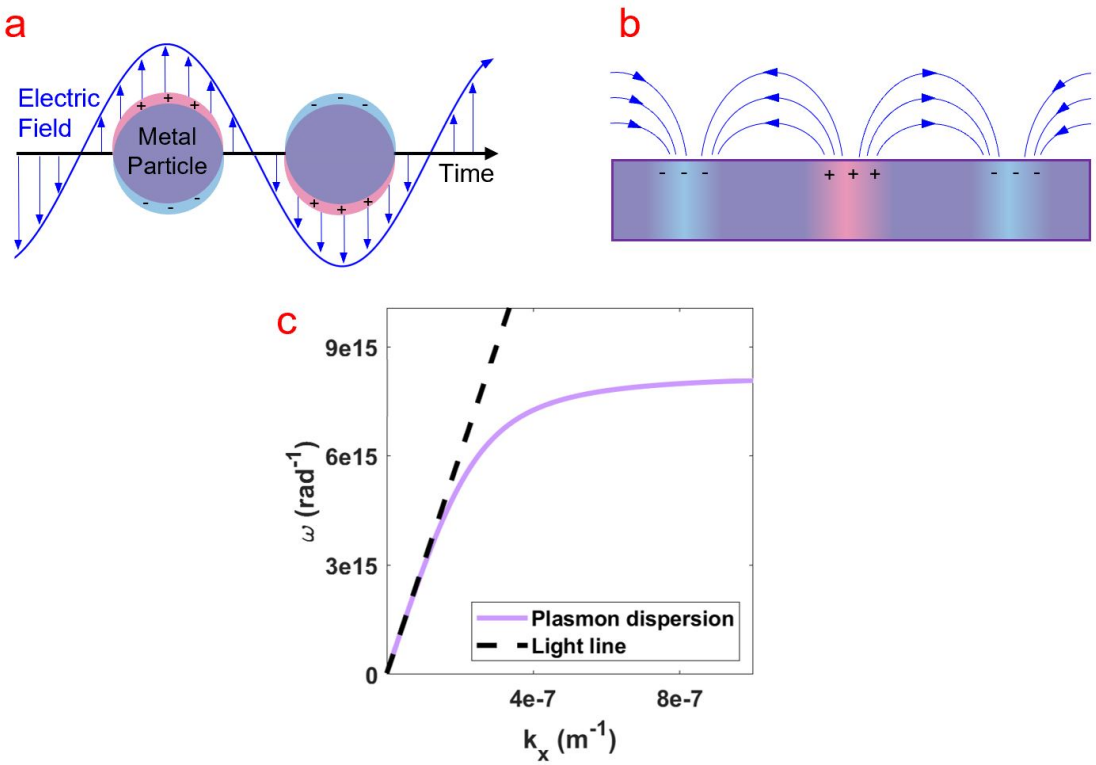

Figure 1.1: Schematics of a LSPR (a) and SPP (b) mode as well as the dispersion relation for a plasmon, in this case a silver film (c).

k_x. In contrast, the plasmon dispersion relation is defined by the relationship between the permittivity function of the metal, (ϵ_1), and of the dielectric medium (ϵ_2).[1]

$$k_x = \frac{\omega}{c}\left(\frac{\epsilon_1\epsilon_2}{\epsilon_1+\epsilon_2}\right)^{1/2} \tag{1.2}$$

Both of these dispersion relations are plotted in Figure 1.1c. The momentum mismatch arises from the fact that neither of these curves intersects, the plasmon dispersion only asymptotically approaches the free space light line at small wave vectors. To couple free space radiation to a SPP in a given material, it is necessary to provide the missing momentum. This is commonly done by using a prism either near or in contact with the surface

in order to couple the free space light into the medium with correct momentum.[3, 4] It is possible also to use a periodic grating on the surface. This grating provides the additional momentum by increasing the parallel component of the wave vector to the surface by an amount dependent on the spacing of the grating.[5] While this requires additional fabrication, the broad tunability during the fabrication of the nanostructured grating allows for careful tailoring of the exactly plasmon wavelength. It is worth noting as well that surface roughness or isolated structures on the surface can also relax momentum constraints enough to allow for coupling of free space light into a plasmon mode.[5]

The quality that has garnered interest is the optical confinement into sub-wavelength volumes. This localization of the plasmon to a small volume causes enhancement of the electric field in that volume as compared to the electric field intensity in free space. These areas of extremely high electric field enhancement are termed 'hot spots' in the material and are often most intense at corners and sharp features in nanostructures.[6] Some of the earliest use of this was surface enhanced Raman spectroscopy (SERS),[7] however it has since found uses in a variety of other applications such as sub-wavelength imaging[8] and detection techniques.[9] The electric field enhancement in hot spots on the surface of metal nanostructures can drastically increase the intensity of weak Raman signals, enough to reach single molecule sensitivity.[10] Similar techniques have been further explored by the development of tip enhanced Raman spectroscopy (TERS), in which a plasmonic metal tip is brought into close proximity to a surface and uses that local field enhancement provided by the tip to enhance the Raman signal.[11]

Across a broader range of disciplines, there have been many studies that have contributed to refining the understanding of the design space for plasmonic materials for systematic control of light-matter interactions, culminating in the development of so called 'metamaterials' composed of plasmonic sub units that support exotic optical responses including near unity absorption,[12] negative index of refraction,[13] pronounced circular

dichroism,[14] or enhancement of a wide variety of non-linear phenomena.[15] Plasmonic metamaterials are not limited to noble metals alone, and there has been work done in tungsten[16, 17] and a variety of conductive ceramics including titanium and zirconium nitrides[18, 19] in addition to the traditional plasmonic metals such as gold, silver, or copper.

An additional application that is of particular interest for plasmonic metals is photothermal applications. Metals exhibit an extremely low efficiency for photoluminescence ($< 10^{-6}$ %),[20] therefore all optical energy absorbed is thermalized as vibrational energy in the metal. Given the ability to tune the absorption of plasmonic metamaterials over a wide spectra range from UV to mid-IR, it is thus possible to concentrate photothermal energy from optically-induced heating. One of the most intriguing developments in plasmonics is the use of plasmonic metal nanostructures to provide extreme localized heating for use in cancer therapy.[21, 22, 23] In addition, it has been shown that the tailorability of the optical response can allow for metamaterials to be leveraged in several types of power cycles, including solar-powered water heating, distillation, and thermoelectric power generation.[24, 25, 26]

1.2 Blackbodies and Planck's Law

A concept fundamental to the understanding of photothermalization in any material is understanding how modifying optical properties can be related to the temperature. It has been long established that the temperature of a surface can be calculated from the power absorbed by a material by considering its absorptivity, as well as the emissivity. The absorptivity, $\alpha(\lambda, \theta, \phi)$, is a function of both the wavelength and angle of the incoming radiation. The thermal emissivity of the material, $\varepsilon(\lambda, \theta, \phi)$, is a property that defines emission of radiation from the surface. Kirchoff's law states that for all angles and wavelengths $\alpha(\lambda, \theta, \phi) = \varepsilon(\lambda, \theta, \phi)$, meaning that absorption and emission are equivalent. The original

derivation of Kirchoff's law assumed thermal equilibrium in objects much larger than the wavelength of light, thus there has been debate on whether it applies at all to plasmonic nanostructures. However, generalizations of Kirchoff's laws have been expanded for non-equilibrium systems by being alternately derived using fluctuational electrodynamics.[27]

A blackbody is a material that absorbs and emits with unity efficiency, ie $\alpha(\lambda, \theta, \phi) = \varepsilon(\lambda, \theta, \phi) = 1$ with a spectrum that is only dependent on its temperature as defined by Planck's law.[28]

$$I(\lambda, T) = \frac{2hc^2}{\lambda^5} \frac{1}{\exp \frac{hc}{\lambda k T} - 1} \tag{1.3}$$

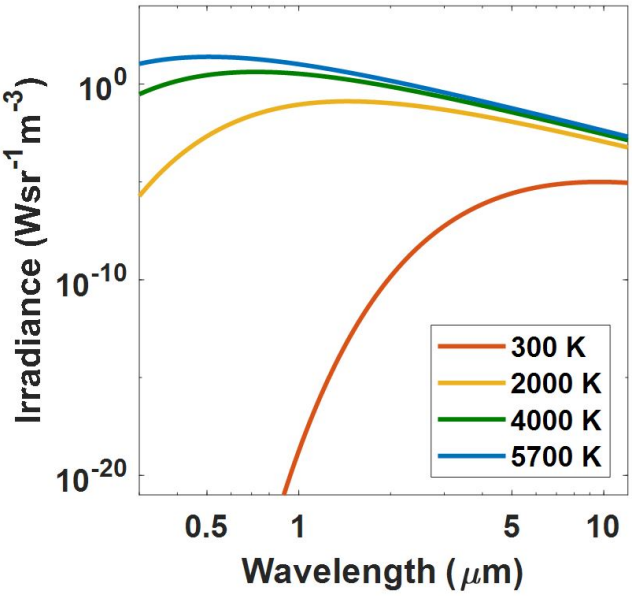

Figure 1.2: The calculated spectral irradiance for a blackbody of various temperatures.

As the temperature of a blackbody increases the spectral distribution of the spectrum shifts towards higher energies. For example the sun can be approximated as a blackbody

at approximately 5700 K which puts the peak in the visible region of the spectrum at 500 nm, while a blackbody at room temperature peaks at 10 μm as can be seen in Figure 1.2. Total integrated power per unit area emitted from a blackbody can be found by integrating Eq. (1.3) over the hemispherical area of the surface at all wavelengths, assuming that the only way the material interacts with the environment is thermal emission and absorption. This is known as the Stefan-Boltzmann law.

$$P = \varepsilon \sigma T^4 \tag{1.4}$$

Where $\sigma = \dfrac{2\pi^5 k^4}{15c^2h^3}$ is the Stefan-Boltzmann constant and ε is the emissivity of the material. In the case of a perfect blackbody, $\varepsilon = 1$. In real materials, the emissivity is defined as the relative emission from the material as compared to a perfect blackbody at an equivalent temperature. The Stefan-Boltzmann law is the simplest case for which the emissivity, and thus the absorptivity, is angle and wavelength independent. Even so, it's clear that changes in emissivity will have a profound affect on temperature in the system.

1.3 Two Temperature Model

Before optical absorption dissipates as vibrational heating in a material, there are several microscopic steps that characterize the relaxation of the short-lived sub-population of photoexcited carriers. As established by a wealth of *ab initio* calculations and confirmed in ultrafast transient absorption (TA) studies, plasmon decay occurs primarily via Landau damping and bulk losses such as interband absorption.[29] Which mechanism dominates is dependent on the size of the nanostructure, with bulk losses dominating in nanostructures with lateral dimensions larger than ~10 nm.[30, 31] Optical excitation instantaneously provides an excited-state distribution of electrons and holes that depends on the frequency of excitation, optical power, and the characteristic transition dipoles of the absorber. Within femtoseconds this non-thermal sub-population of excited carri-

ers undergo electron-electron scattering to achieve a distribution of 'hot' electrons with a characteristic temperature that, during intense ultra-short pulsed excitation, can be several 1000's K greater than the ambient temperature of the metal lattice.[32] Within picoseconds the carriers further relax via electron-phonon coupling to induce vibrational excitation of the metal lattice.

Depending on the thermal impedance with the environment and the absorbed optical power, the phononic temperature, also known as the lattice temperature, of the plasmonic absorber can also be significantly increased. However, given the large difference in the heat capacity of the electron gas compared with the metal lattice, the vibrational temperature increase is usually significantly lower than the electronic temperature increase, with reports of lattice temperature increases of ~1 K to 100's K, depending on optical fluence.[33, 34] Notably, solar-induced vaporization of water around colloidal SiO_2/Au nanoparticles has been reported.[35] In general, increases in phononic temperature also allow for the metal to reach higher electronic temperatures, as will be demonstrated in later chapters.[36]

The physical picture of the dynamics of the hot carriers observed in TA studies is summarized in the well-established two-temperature model (TTM), where the time dependence of energy transfer between the excited electrons and the metal lattice is defined by the electron-phonon coupling constant, G, and the thermal transport away from the absorbing region, depending on the electronic thermal conductivity, k_e, and the electronic and phononic heat capacities, C_e and C_p respectively.[32]

$$C_e(\partial T_e/\partial t) = \Delta[k_e \Delta T_e] - G(T_e - T_p) \tag{1.5}$$

$$C_p(\partial T_p/\partial t) = G(T_e - T_p) \tag{1.6}$$

In the limit that the dimensions of the absorber are on the scale of the penetration depth

into the metal (approximately 20 nm), there is assumed to be a negligible gradient in the electronic temperature, and therefore the $\Delta[k_e \Delta T_e]$ term is considered to be zero.

Some of the most fast-developing recent research in plasmonics explores the opportunities for using the photoexcited carriers for photochemistry or optoelectronic devices in the short period of time before they thermalize with the lattice. Reports of solar-power water splitting and CO_2 reduction, as well as photo-activated plasmonic antenna-reactor systems illustrate the vast interest in these non-equilibrium electrons.[37, 38, 39] Major challenges are two-fold. First, given the short femtosecond lifetime before electron-electron scattering establishes a thermal distribution, T_e, the mean-free path for a photo-excited, non-thermal electron or hole is ~100 nm or less. Thus, carriers with the highest kinetic energy are very short-lived, compared with the hot electrons in the thermal distribution, T_e. Even still, the lifetime of hot carriers is also short, thermalizing with the lattice within picoseconds. Additionally, there is a limited escape cone of electron or hole trajectories with suitable momentum to exit the metal. Notably, nanoscopic confinement increases the probability that a hot electron will both reach the surface and have appropriate momentum for collection in an external device or chemical reaction.

It should be noted that the above system of equations only describes the behavior of the electrons after thermalization due to electron-electron scattering. It is possible to extend the TTM into the so-called 'expanded TTM' which additionally accounts for not only electrons thermalized to T_e and T_p but also the short lived non-thermalized portion of electrons.[36, 40, 41]

1.4 Measuring Hot Electron Dynamics

To date, TA studies of the relaxation of the electron gas after optical excitation using ultrafast pump-probe geometries have been a primary tool for understanding plasmonic photodynamics. In combination with the expanded TTM it is possible to gain a significant

amount of information about the timescales of thermalization, both on the femtosecond scale of electron-electron scattering and on the longer picosecond timescale that encapsulates electron-phonon interactions.[36, 41, 42] These studies have provided a quantitative measure of the lifetime of electrons in the non-equilibrium distribution and the electron-phonon coupling constant, G in Eqs. (1.5) and (1.6), which connects the lifetime to microscopic loss pathways in the metal.[43] This research has also provided several other insights, including evidence for direct excitation into charge-transfer states at the interface of the metal with a semiconductor or molecule[44] and the observation of coherent excitation of vibrational modes in plasmonic nanoparticles after pulsed excitation.[29]

1.5 Summary

While pump-probe studies, including TA spectroscopy, provide a wealth of information about hot electron dynamics, there is also much interest in the hot electron response during continuous wave (CW) optical excitation, such as is achieved with devices or photochemical systems under solar illumination. Under these steady state conditions there will always be present a sub-population of electrical carriers with greater kinetic energy than the electrons that have relaxed and equilibrated with the lattice. Moreover, the dynamics of hot carriers in this prolonged time regime, and at significantly lower optical intensity than in ultrafast pump-probe studies, is much less understood. The goal of the following work is to begin to see how photothermalization and hot electron dynamics can be understood during CW illumination.

In Chapter 2, I explore the limits of the phononic temperature that can be reached in plasmonic nanostructures. Through careful modeling it is possible to show that dependent on the illumination source, it is possible to calculate temperature based only on the absorption and emission properties of the nanostructure. I demonstrate that under solar radiation it is possible to predict what absorption and emission properties are needed in order to

heat the surface to several 100's or even 1000's of K under illumination for use in applications such as solar-thermal water heating. Using this knowledge it is possible to solve Maxwell's equations for arbitrary geometries using finite-difference time-domain optical simulations to design real nanostructures for fabrication that are calculated to reach near the melting point of the metal to allow for continuous operation at maximum temperatures without danger of thermal degradation of the nanostructure.

In Chapter 3, it is shown that the energetic distribution of electrons in these plasmonic nanostructures can be probed during CW excitation using anti-Stokes Raman spectroscopy. This technique provides a quantitative measure of a sustained sub-population of the hot electrons at an elevated temperature, T_e, in addition to electrons that are in equilibrium with the phononic temperature, T_p. Because these populations can be measured simultaneously along with the size of the sub-population of hot electrons, the Raman technique additionally gives information about the electron-phonon coupling constant and hot electron lifetime, for comparison with more-established TA methods.

In Chapter 4, I expand on the framework developed in Chapter 3 in order to begin understanding how to rationally tune the hot electron dynamics in plasmonic metal nanostructures. This begins by understanding how changing the dimensions in a nanostructure can change both the optical properties but also how its hot electron behave under illumination. Following this I also explore how changing the substrate and environment of the nanostructure to modify non-radiative loss pathways can also be used to increase the temperature and size of the hot electron sub-population. Another factor of interest is changing the metal of the nanostructure which impacts which applications it may be most suitable for, with a strong focus on gold for photothermal applications and copper for possible catalytic applications.

I will end with a summary and a few closing words on the topics covered and how they can be connected to the broader research interest in plasmonics. Just as there have

been design rules proposed for maximizing photothermal energy concentration for lattice heating in the literature, my goal is to hopefully lead readers to the conclusion that it is now possible to start developing rules for also modifying the hot electron dynamics for developing applications.

2. LIMITS IN PHONONIC TEMPERATURE AND SOLAR SELECTIVE SURFACES*

2.1 Introduction

Due to their limited fluorescence, metals heat up efficiently under illumination as absorbed light is converted into heat via coupling to the phonons in the material.[20] This photothermalization has been taken advantage of for several applications such as photothermal cancer treatments and solar-thermal water heating.[21, 22, 23, 26] Harnessing solar radiation, in particular, is of interest due to solar-thermal power conversion devices having the potential to bypass some of the traditional efficiency and cost issues of traditional semi-conductor based photovoltaic schemes.[45]

Historically, metamaterials designed for the express purpose of harnessing solar radiation in the form of heat have been known as 'solar selective surfaces'. Their absorption properties are carefully tailored in order to take the maximum advantage of the specific spectral range of the sun. A solar selective surface aims to achieve two different properties. The first is that the surface will absorb the maximum possible amount of energy from the sun, while the second is to minimize the amount of energy lost to thermal radiation.[46] Kirchoff's law demands that absorptivity and emissivity are equal at all wavelengths, so there is a trade off between trying to achieve both of these properties.

There are several materials that intrinsically have absorption properties to match what is required for solar selectivity.[47] However they are far from being ideal, and therefore many solar selective surfaces are designed to leverage the properties of many different materials in geometries such as semiconductor-metal tandems,[48] multi-layer absorbers,[49,

*Part of this chapter is reprinted with permission from "Photothermalization and hot electron dynamics in the steady state" by Nicki Hogan, Shengxiang Wu, and Matthew Sheldon, 2020. Journal of Physical Chemistry C, 124, 4931-4945, Copyright 2020 by the American Chemical Society.

50, 51], and ceramic-metal composites.[52, 53] This is not to say it is not possible to create solar selective surfaces out of single materials. Whereas in the prior examples the emissivity was modified due to thicknesses and sizes of different layers, in the case of a single material solar selective surface it is surface structuring that provides the modifications to the emissivity function. This can be seen in examples including 1D and 2D tungsten, silicon, and molybdenum gratings.[54, 55, 56, 57] One theme prevalent throughout these examples is the use of metals as at least one part of the selective absorber to take advantage of the intrinsically low emissivity of the metal in the IR to help minimize thermal emission. It's also well known that careful tuning of the plasmon resonance in the visible can lead to near unity broadband absorption,[12, 58] which leads to the hypothesis than an entirely metallic nanostructure arrays could serve as a solar selective surface if designed to have the proper absorption characteristics.

In this chapter I outline how the absorption can be calculated and optimized for a metal nanostructure such that it will reach the highest possible phononic temperature under solar illumination, and explore what are the limits of phononic temperature as a function of the emissivity. I then follow with a way to use particle swarm optimization in parallel with modeling in order to use those ideal absorption and emission properties to design specific nanostructures for fabrication.

2.2 Simplest Case: Spherical Nanoparticles

Before considering more complex nanostructures, there is benefit in first exploring the most simplistic case of a plasmonic nanostructure: spherical metal nanoparticles. Not only are they simple to fabricate in a wide variety of materials,[59] they are one of the few geometries which has a simple analytic solution to Maxwell's equations to solve for their absorption properties.

Sub-wavelength nanoparticles have an optical cross section that is many times larger

than their geometrical cross section. The solution to Maxwell's equations used to determine this optical cross section in spherical nanoparticles is known as Mie theory. This says that the absorption cross section, σ_{abs}, can be calculated from the extinction and scattering cross section, σ_{ext} and σ_{scat} respectively.[29]

$$\sigma_{ext} = \frac{2\pi r^2}{x^2} \sum_{n=1}^{\infty} (2n+1) Re[a_n + b_n] \tag{2.1}$$

$$\sigma_{scat} = \frac{2\pi r^2}{x^2} \sum_{n=1}^{\infty} (2n+1)[|a_n|^2 + |b_n|^2] \tag{2.2}$$

$$a_n = \frac{\psi_n'(mx)\psi_n(x) - m\psi_n(mx)\psi_n'(x)}{\psi_n'(mx)\zeta_n(x) - m\psi_n(mx)\zeta_n'(x)} \tag{2.3}$$

$$b_n = \frac{m\psi_n'(mx)\psi_n(x) - \psi_n(mx)\psi_n'(x)}{m\psi_n'(mx)\zeta_n(x) - \psi_n(mx)\zeta_n'(x)} \tag{2.4}$$

$$\psi_n(z) = (\frac{\pi z}{2})^{1/2} \times J_{n+1/2}(z) \tag{2.5}$$

$$\zeta_n(z) = (\frac{\pi z}{2})^{1/2} \times (J_{n+1/2}(z) - iY_{n+1/2}(z)) \tag{2.6}$$

$$\sigma_{abs} = \sigma_{ext} - \sigma_{scat} \tag{2.7}$$

In this set of equations, the absorption of the nanoparticles is calculated as a function of the size parameter $x = 2\pi r n_m/\lambda$ where r is the radius of the particle and $n_m(n_p)$ is the refractive index of the medium (particle). The parameter, m, is defined as the ratio between the refractive index of the particle and the environment. Eqs. (2.5) and (2.6) use the traditional spherical Bessel functions. An example of the calculated σ_{abs} for three sizes of gold nanoparticles is shown in Figure 2.1a showing the plasmon peak at approximately 530 nm, which shifts as the radius of the particle changes.

Using the absorption cross section to calculate the power absorbed by the nanoparticles, it is possible to expand Eq. (1.4) to find the temperature of these particles during

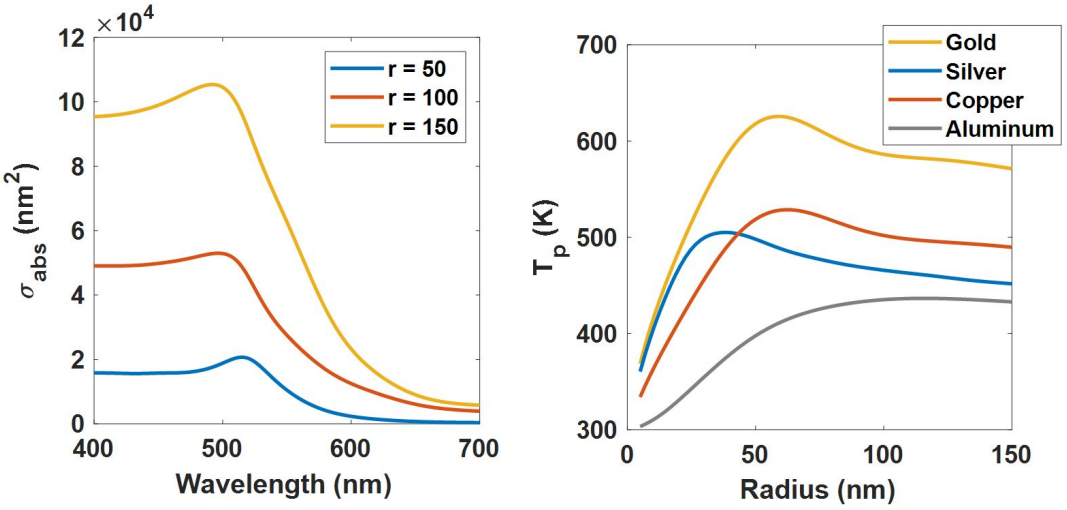

Figure 2.1: The calculated absorption cross section for three different types of gold nanoparticles with differing radii (a) as well as the calculated temperature for nanoparticles in common plasmonic metals as a function of the radius (b).

optical excitation. Due to power balance considerations, the total power absorbed by the material, P_{abs}, has to be equivalent to the power emitted, P_{emit}, over a given area A which corresponds in this case to the surface area of the nanoparticle. From the Stefan-Boltzmann law, the power emitted by the structure is already defined. This is done in the limit of only radiative losses; specifically, no conduction or convection is considered, which is something that will be described in more depth in the following section. For now, let's make the assumption that by keeping the particles in a vacuum environment we have completely removed the effect of non-radiative thermal transport pathways.

$$P_{emit} = A\varepsilon\sigma T^4 \tag{2.8}$$

$$P_{abs} = \int \sigma_{abs} I_{source} d\lambda + A\varepsilon\sigma T_{amb}^4 \tag{2.9}$$

The power absorbed is composed of two terms: the power absorbed from the light source and the power absorbed from the ambient environment at a temperature T_{amb}. Ne-

glecting power absorbed from the environment would indicate that the material would be at absolute zero in the absence of any illumination. Assuming a T_{amb} of 300 K, the power absorbed from the environment is negligible except in the limit of extremely low illumination. The full code for this calculation is shown in Appendix A.

One of the most interesting light sources to consider is the sun. In this case, the particle would be converting the optical energy into thermal energy which has applications such as solar-thermal water heating assuming the temperature reached exceeds 373 K. In this case I_{source} is the standard AM 1.5 solar spectrum as measured by NREL. The refractive index for each metal are pulled from standard experimentally measured values.[60, 61]

Using all of these parameters, I can calculate the temperature reached in spherical metal nanoparticles of different metals as a function of their radius, as is shown in Figure 2.1b. Gold and silver are the two metals most often used in plasmonic applications due to their strong resonances. Silver shows resonances further to the UV than gold does, which minimizes absorption of the solar spectrum, and therefore silver fails to reach temperatures quite as high as gold. Copper is another metal that has been shown to be plasmonic, though not quite to the extent of gold or silver. Due to its increased absorption in the visible it reaches higher maximum temperatures than silver, but it still is not close to being able to match gold. For comparison aluminum is also included. While it is possible to use aluminum to make plasmonic nanostructures, the resonances are weaker and, as with silver, they are further to the UV. One benefit to aluminum over any of the other metals however is that it is extremely cheap and readily available which makes it promising for practical devices.

In the case of all four metals, there is a radius in which there is a maximum temperature that can be reached. This is the point at which smaller particles do not absorb significant enough radiation to reach high temperatures, but larger particles lose a greater fraction of energy to blackbody emission and therefore reach lower temperatures. This tradeoff

between increasing adsorption while minimizing emission becomes the primary design parameter in designing nanostructures that maximize surface temperature.

2.3 Designing Solar Selective Surfaces

While spherical nanoparticles are an interesting simple case that introduces several of the design parameters for maximizing temperature, they are not as useful for real devices as much as planar surfaces are. In these solar selective surfaces, the absorption is tuned such that there is high absorption in the spectral region where there is greatest intensity to the solar spectrum, the visible region, and low emission in the region where there will be thermal emission at the temperatures the device reaches, the IR region. Due to intrinsically low emissivity in the IR and tunable absorption due to plasmon resonances, metal nanostructures are an ideal candidate for solar selective surfaces. For this to be true however, it is necessary to know exactly what sort of emission and absorption properties are most important during design of these nanostructures.

In order to establish the limits for what temperatures could be reached by an ideal solar selective surface, I consider how to calculate the temperature of a surface based on its absorption properties. As with the case of spherical nanoparticles, power absorbed equals power emitted. I no longer consider the emissivity to be an average value and instead use the full wavelength and angle dependent quantity which involves integration over all three dimensions.

$$P_{abs} = P_{sun} + P_{amb} \tag{2.10}$$

$$P_{sun} = \int_{0^\circ}^{360^\circ} \int_{0^\circ}^{0.26^\circ} \int_{0}^{\infty} \alpha(\lambda,\theta,\phi) I_{solar}(\lambda,\theta,\phi) cos\theta sin\theta d\lambda d\theta d\phi \tag{2.11}$$

$$P_{sun} = \int_{0^\circ}^{360^\circ} \int_{0^\circ}^{90^\circ} \int_{0}^{\infty} \alpha(\lambda,\theta,\phi) \frac{2hc^2}{\lambda^5} \frac{1}{\exp\dfrac{hc}{\lambda k T_{amb}} - 1} cos\theta sin\theta d\lambda d\theta d\phi \tag{2.12}$$

In the following calculations, integration over the zenith angle, θ, is limited to a hemispherical area to account for a surface that is only absorbing and emitting from the top face. This is a situation that can be matched when there is a perfect mirror on the underside of the structure. Power absorbed from the sun is only integrated over the solid angle subtended by the sun, 0.26°.[62] The surface will emit according to its emissivity function as well as its temperature, as indicated by $P_{radiative}$. Appendix B shows the code for this calculation. In addition, the absorber may lose power through non-radiative loss pathways, $P_{non-radiative}$. In these calculations it is assumed that $P_{non-radiative}$ is neglible as compared to $P_{radiative}$. While engineering this in a real device is extremely difficult, there are ways to minimize non-radiative losses such as conduction or convection. For example, by working in a vacuum it is possible to minimize convection. Additionally, if the entire nanostructure is illuminated and only small physical bridges are used to connect it to the rest of the device, there will only be conduction away from the nanostructure by those small bridges. Devices of this type will be discussed further in Chapter 4.

$$p_{emit} = P_{radiative} + P_{non-radiative} \tag{2.13}$$

$$P_{radiative} = \int_{0^\circ}^{360^\circ} \int_{0^\circ}^{90^\circ} \int_{0}^{\infty} \varepsilon(\lambda,\theta,\phi) \frac{2hc^2}{\lambda^5} \frac{1}{\exp\dfrac{hc}{\lambda k T_p} - 1} cos\theta sin\theta d\lambda d\theta d\phi \tag{2.14}$$

Assuming $P_{non-radiative}$ is eliminated, or understood, the phononic temperature, T_p of the surface is a unique function of its absorbtivity, and thus also its emissivity. Based on these equations, an ideal blackbody in which $\alpha(\lambda,\theta,\phi) = \varepsilon(\lambda,\theta,\phi) = 1$ in a room temperature environment where $T_{amb} = 298$ K, is expected to reach a temperature of 410 K. This temperature would decrease significantly were there to be significant non-radiative losses, so in all cases it is best to minimize those pathways.

2.3.1 Wavelength Selective Absorber

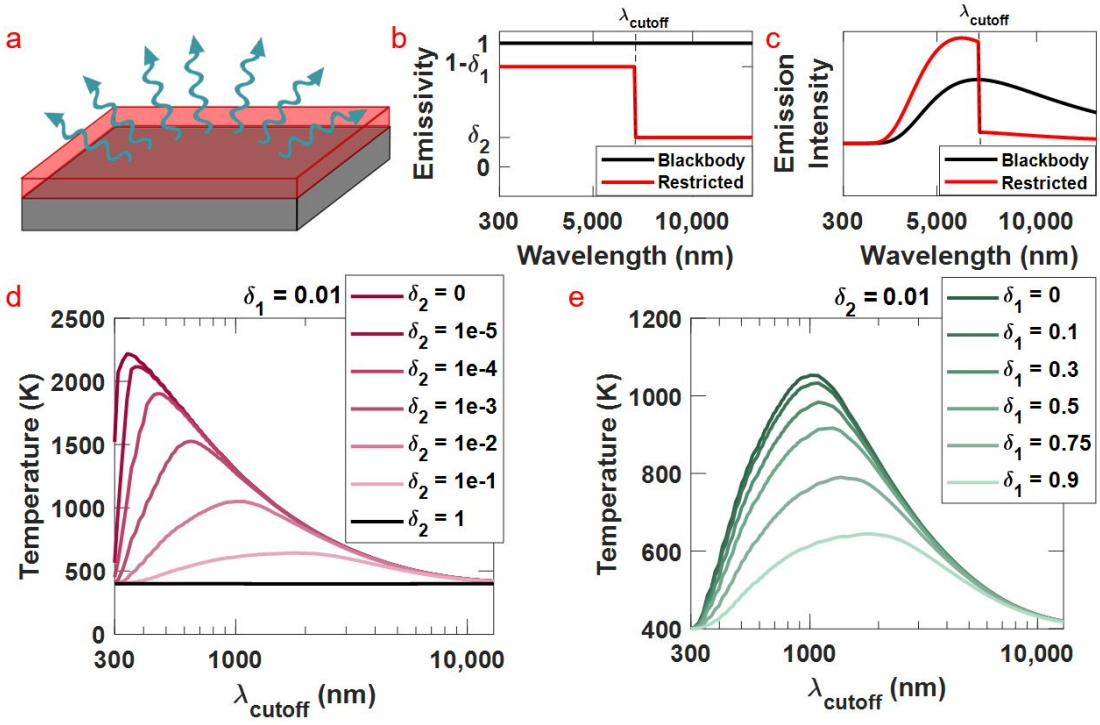

Figure 2.2: (a) Schematic of a selective absorber optimized for solar heating along with (b) the emissivity function (red trace) compared to a blackbody (black trace) and (c) the relative spectra emission intensity compared with a blackbody when both absorbers are in direct sunlight. The blackbody reaches $T_p = 410$ K and the depicted selective absorber with $\delta_1 = \delta_2 = 0.1$ and $\lambda_{cutoff} = 7100$ nm reaches $T_p = 643$ K (d) and (e) show the possible temperatures that can be obtained by modifying emission in either the high or low wavelength region of the spectrum as a function λ_{cutoff}.

To understand the limits of photothermalization, I start by showing how systematic control of the emissivity function leads to dramatic changes in the temperatures that can be reached. As shown in Figure 2.2a, a generalized absorber is considered for which the surface as been modified through nanostrucutring to provide a step function the spectral

absorptivity, and the emissivity equivalently. The surface provides strong absorption for wavelengths below some cutoff, λ_{cutoff}, and weak absorption at longer wavelengths. This is shown mathematically in Figure 2.2b. While the 'ideal' absorber would have unity absorption in the visible and zero emission in the IR, that is not possible to reach in a real material. It is possible to get close however. Near unity absorption has been demonstrated in plasmonic materials in the visible spectral region,[58, 12] and noble metals do have intrinsically low emissivities on the order of $\varepsilon < 0.05$ in the IR. To account for these deviations I define δ_1 as the deviation from unity at short wavelengths and δ_2 as the deviation from zero at longer wavelengths. For comparison, I also show the emissivity of a perfect blackbody.

As can be clearly seen in Figure 2.2c, the presence of the step function in the emissivity profoundly impacts the spectral distribution of the emitted radiation in comparison with the emission from a blackbody. Both the red and black trace in Figure 2.2c show thermal emission due to solar absorption. This change in the emission profile, with more photons emitted at higher energy, entails that the selective absorber is at a higher temperature due to the dependence on temperature in the Planck distribution, and the requirement that both surfaces emit the same total power that they absorb. In this figure the blackbody has reached a temperature of 410 K, while the selective absorber has reached a temperature of 643 K.

In Figure 2.2d and e, I consider how temperature is impacted by the spectral position of λ_{cutoff} as well as the dependence on the magnitude of δ_1 and δ_2. First, as summarized in Figure 2.2d, it is clear that the highest possible temperatures are obtained when the long wavelength emissivity is kept as close as possible to zero. The maximum temperature obtained is highly sensitive to very small changes as δ_2 approaches zero. This indicates that the temperature is more sensitive to small decreases in thermal emission than it is to increases in solar absorption. Decreasing emissivity at long wavelengths also blue shifts

the λ_{cutoff} that provides the maximum temperature, until λ_{cutoff} is shifted so far to the blue that it impedes solar absorption. If however the long wavelength emissivity is fixed at a value comparable to the intrinsic emissivity of a noble metal film, $\varepsilon = 0.01$, as in Figure 2.2e, then the dependence on deviations for perfect absorption at short wavelengths is less pronounced. Across the entire range of values for δ_1, the spectral position of λ_{cutoff} that provides the highest temperature is maintained between 1000-2000 nm, and the maximum temperature is between 600-1200 K. Nonetheless, this is still a significant increase in temperature compared with the temperature of 410 K that a blackbody obtains in full sun.

2.3.2 Angle Selective Absorber

While traditional solar selective surfaces only consider the wavelength restriction described above, another powerful way to affect the thermal energy balance of an optical absorber and increase temperature is to constrain the angular range of thermal emission, as depicted in Figure 2.3a. In analogy with the analysis of modifications to the wavelength dimension of the spectral emissivity, I consider a nanostructured surface that has been designed to strongly absorb and emit radiation only within a specific solid angle range around normal incidence. This solid angle range is defined by α_{cutoff} with absorption or emission into larger angles prohibited. In the analysis that follows, I assume that the sun is at normal incidence so that the radius of the solid angle subtended by the solar disk extends to 0.26° from surface normal.[62] The emissivity function is depicted in profile in polar coordinates in Figure 2.3b, assuming radial symmetry around the normal axis in all calculations. The cos(θ) dependence that characterizes the Lambertian emission of radiation from a point on the surface of a blackbody is also depicted (black trace). Further, deviations from the perfect step function in the angle dependent emissivity are represented by γ_1 at low angles around normal incidence, and γ_2 at high angles. Figure 2.3c shows how

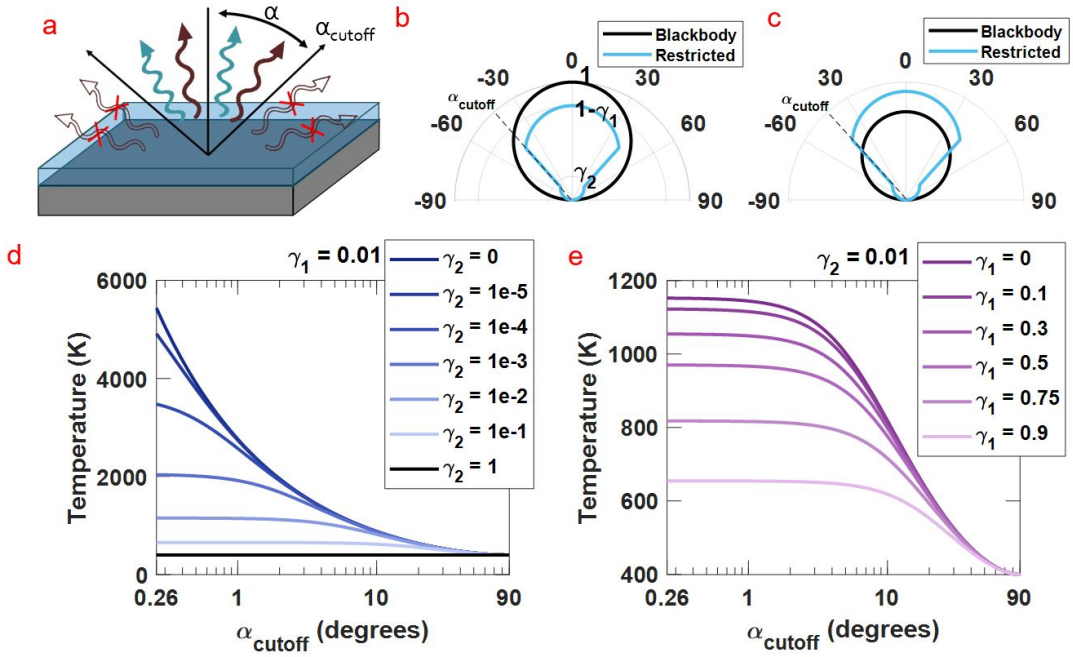

Figure 2.3: (a) Schematic of an angle selective surface along with (b) the emissivity function (blue trace) compared to a blackbody (black trace) and (c) the relative emission intensity compared to a blackbody when both absorbers are under full sun at normal incidence. The blackbody reaches $T_p = 410K$, and the angle selective surface depicted here, with $\gamma_1 = \gamma_2 = 0.2$ and $\alpha_{cutoff} = 40°$ reaches $T_p = 653K$. (d) and (e) show the possible temperatures that can be obtained by modifying emission in either the high or law angle range as a function of α_{cutoff}.

the emission intensity from a surface with $\alpha_{cutoff} = 42°$ is increased at small angles compared with a blackbody, due to the change in the angle dependent emissivity. As above, in accordance with Eqs. (2.11)-(2.14), this increase in emission intensity into some angles entails that this angle selective absorber is at a higher temperature, 653 K, as compared with a blackbody, 410 K, when absorbing light from the sun.

Temperature changes are also analyzed as a function of the choice of α_{cutoff}, including the dependence on γ_1 and γ_2 as depicted in Figure 2.3d and e. As γ_1 and γ_2 both approach zero, the temperature that can be reached by the surface is increased, with higher

temperatures obtained as α_{cutoff} is decreased. The maximum temperature obtained for any combination of γ_1 and γ_2 is reached when $\alpha_{cutoff} = 0.26°$, or when thermal emission is limited into the same solid angle that light is received from the sun. Here also, we see that the temperature response is more sensitive to decreases in thermal emission into large angles, as opposed to increases in solar absorption near normal, hence temperature depends more strongly on γ_2 than γ_1. Note that in the ideal limiting case with $\gamma_2 = 0$ the dependence on α_{cutoff} corresponding to the darkest blue trace in Figure 2.3d is obtained for any value of $\gamma_1 \neq 1$

Unlike the wavelength selective absorber, increasing temperature using only angle selective absorption and emission requires that the correct orientation with respect to the optical source is maintained. For structures heated by sunlight this can be achieved with mechanical solar trackers that move the absorber to follow the sun over the course of the day and year. Similar strategies are employed in solar-thermal power converters and photovoltaic schemes that use external lenses or optical concentrators to increase the intensity of sunlight on the converter, since lenses also require correct orientation. Indeed, restricting angle dependent emission as described here provides the same temperature increases that can be achieved using optical concentrators, because concentrator lenses effectively increase the solid angle of radiation received from the sun, increasing the angle range of the integral describing the power balance in Eq. (2.11). The net effect is equivalent to decreasing the angle dependent emission in Eqs. (2.12) and (2.14). Note that lenses also increase the apparent power from sunlight hitting the absorber, based on the concentration factor of the lens. This dependence on angular range is why the two strategies, concentrator optics or angle restrictive emission, have little theoretical benefit if used in conjunction. However, unlike conventional concentrator lenses, selective absorbers can be designed to have high absorption of sunlight at all angles but lower emission of thermal radiation into any angle, as was previously outlined. Thus, nanostructured surfaces can provide many

advantages in comparison with conventional tracking optics used in solar-thermal concentrator applications.

2.4 Designing a Plasmonic Absorber

With knowledge of the ideal absorption and emission properties that can give rise to the largest temperature increases during photothermalization of direct sunlight, I next show how the spectral and angle dependent emissivity of plasmonic surfaces can be engineered to approximate this ideal response. Further, maximizing the phononic temperature of the metal is a crucial step for also increasing the temperature of the non-equilibrium hot electrons during steady state absorption. There have been several established design motifs among researches in plasmonics and nanophotonics that use periodic sub-wavelength arrays to provide desirable optical attributes, such as strong broadband absorptivity, restricted angular emission, or thermal energy beaming.[63, 64, 65] I used these designs as a starting point in order to begin tailoring my own.

2.4.1 Simulation Methods

While it was possible find an exact solution to Maxwell's equation to calculate the absorption properties of spherical nanoparticles, periodic nanostructures do not have that advantage. It is, however, possible to approximate the exact solution by using alternate simulation methods. Here I use finite-different time-domain (FDTD) method simulations, which are full wave optical solvers which have been well established for modeling plasmonic systems.[66, 67, 68, 69] In this method, Maxwell's equations are solved iteratively in user defined mesh cells across a given geometry at each time step in the simulation. These mesh cells are defined by refractive index and dictate how light propagates through the different cells and out of the simulation. In this way, I define an arbitrary geometry with any given refractive and calculate the absorptivity. This calculated absorptivity approaches the exact solution as the mesh cells get infinitely small, though there is then also

an exponential increase in computational costs. I used a commercially available software to run these simulations (Lumerical).

For these simulations I define the unit cell of a metal nanostructure on top of a film of the corresponding metal on an infinitely thick silicon substrate, which approximates the experimental samples later fabricated. The refractive index for all material was taken from experimental sources and interpolated to match the wavelengths used in the simulation. The data for gold was taken from Johnson and Christy[60] and all other materials taken from Palik.[61] Light was introduced from a plane wave source above the sample with the reflected light being measured at a monitor placed further above the source. The boundaries above and below the nanostructure were perfectly matched boundary (PML) conditions, while the four edges were Bloch boundary conditions. These behave as periodic boundaries such that all light exiting one edge is introduced equivalently on the opposite facing boundary, except they include a phase factor to prevent the irregularities due to angled plane wave sources having a non-zero component of the the wave vector in the plane of the source. Due to the fact that there is no transmission through the substrate, $absorptivity = 1 - reflectivity$ which allows simple calculation of the angle and wavelength dependent absorptivity for any given nanostructure.

2.4.2 Optimization of the Nanostructure Geometry

In order to try to maximize temperatures, I then expanded these simulations by doing a particle swarm optimization. In this type of optimization, a range of tunable parameters are selected that define a variable space. For an initial point, a figure of merit is evaluated, and then the next point in picked in variable space where the same figure of merit is again calculated. By measuring whether that figure of merit is getting larger or smaller, the next point in variable space is picked to attempt to approach the global maximum. To avoid finding local maxima, several initial points are chosen that all move through variable

space independently to each move towards the maximum. In the case of our simulations, the variable space is defined by the geometrical parameters of a metal nanostructure such as pitch or lateral dimensions. The figure of merit is the calculated temperature of the surface under solar illumination according to Eqs. (2.11)-(2.14).

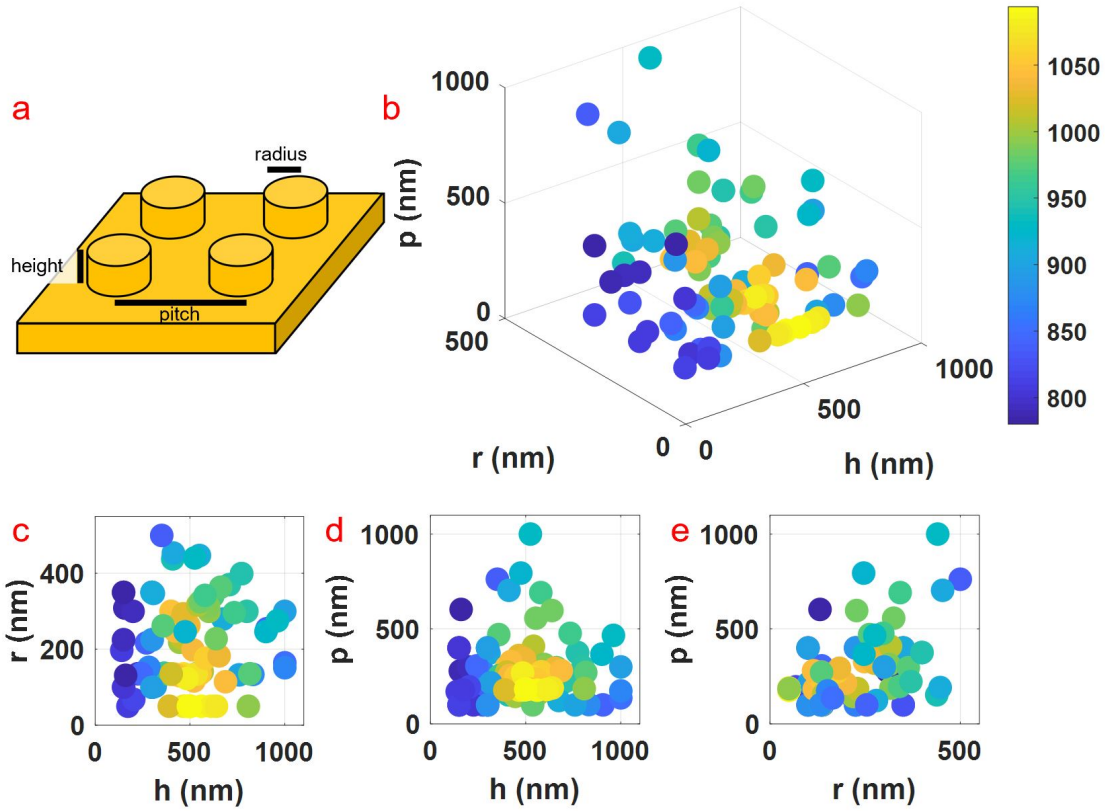

Figure 2.4: (a) Generalized schematic of a gold nanostructure used in a particle swarm optimization with three tunable parameters: disk radius, disk height, and pitch. (b) The full 4D scatter plot of every nanostructure simulated, the colorbar corresponds to calculated temperature in K. Projections of this plot along all three axes are shown in (c-e).

The starting nanostructure chosen was one that is still relatively simple, which has the benefit of also being easy to fabricate. This geometry is shown schematically in Figure 2.4a and is composed of a periodic square array of gold nanodisks on an optically thick

gold film, which in these simulations was 100 nm thick. There are three parameters to act as the variable space for the particle swarm optimization: the radius of the disks, the heights of the disks, and the center to center distance of the nanostructures. This center to center distance is also known as the pitch of the nanostructure. The lower limit of each of these parameters was set according to what would be realistic to fabricate, namely that a feature size of 50 nm or less is extremely difficult to achieve lithographically.

Starting with 9 initial points, a total of 81 individual simulations were run. The temperatures calculated for each of these simulations are shown in Figure 2.4b. The three axes correspond to the three design parameters demonstrated in Figure 2.4a while the color of each point is the calculated temperature in K. In order to more easily draw conclusions, the projections of this plot along each of the three axes are shown in Figure 2.4c-e. In general it can be seen in Figure 2.4c and d that structures which are taller and with smaller radii reach the highest temperatures. This is due to these structures essentially being a pillar structure which have been shown to provide better angular control of the absorptivity.[70, 71, 72] As was shown in Section 2.3.2, careful control of the angle of emission leads to much higher temperatures. Additionally, structures with radii or pitches on the larger side red-shift the plasmon resonances which in addition to increasing the absorptivity in the near-IR portion of the spectrum, also increases the thermal emission which drastically lowers the temperature. In Figure 2.2d it can be seen that temperature falls drastically as emissivity in the IR increases, therefore it is beneficial to stay with smaller nanostructure dimensions, both in radius and pitch.

2.4.3 Best Structure

From the results of the optimization, it is possible to narrow in on the specific geometrical parameters for this gold nanostructure that provide the highest temperature. This structure matches the schematic in Figure 2.4a with dimensions of radius = 123 nm, height

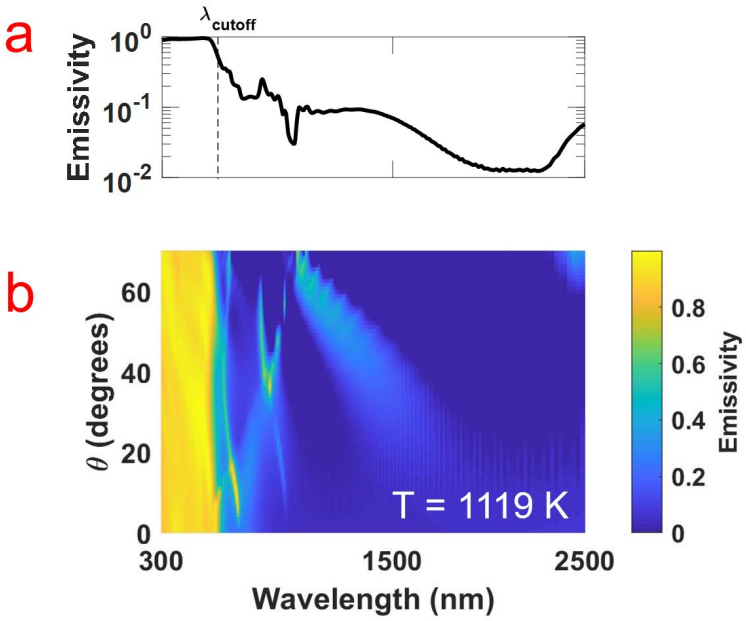

Figure 2.5: (a) The integrated emissivity function of a nanostructure following the schematic in Figure 2.4a with radius = 123 nm, height = 484 nm, and pitch = 513 nm as a function of wavelength along with (b) the full angle and wavelength dependent emissivity function.

= 484 nm, and pitch = 513 nm. The integrated emissivity function as a function of wavelength is shown in Figure 2.5a which can be seen approximately corresponds to a wavelength restricted selective surface with $\lambda_{cutoff} = 590nm$ and maintains near unity absorption at wavelengths below that. Average emissivity through the IR is on the order of 0.05 which is perhaps higher than that of bulk gold, but still low enough to provide restriction of thermal emission. Despite the minimal angular restriction, seen in Figure 2.5b, the calculated temperature that can be reached by this nanostructure is 1119 K. For reference, the melting point of bulk gold is 1336 K,[73] so this type of structure may be the closest it is possible to get to the melting point without danger of destruction of the nanostructure.

2.5 Summary and Future Directions

In this chapter, it was shown how to predict the phononic temperature of the system based on its absorption and emission properties. Optimization of those properties, especially careful control of lowering the emission at long wavelengths and high angles while maintaining high absorption in the visible, allows for materials to reach 100's of K under solar illumination which shows promise for applications such as solar-thermal water heating. Using full wave optical simulations, I showed how to use particle swarm optimizations to find real nanostructures with the desired absorption properties for fabrication and use in a real device.

While not previously discussed, a major limitation of these types of surfaces is that temperatures can only be maintained up to the melting point despite the fact that ideal higher temperatures can be reached as shown in Figures 2.2 and 2.3. While it is possible to use more complex geometries in order to provide better angle restriction and reach higher theoretical temperature, it may not be worth the added fabrication difficulties when the nanostructure would not be able to practically sustain those temperatures. Better angular control has been found in materials designed to show index-near-zero properties [74] and in bullseye type structures.[75] Maintaining a higher phononic temperature allows for the material to sustain higher electronic temperatures as well. In Eqs. (1.5)-(1.6), increasing the phononic temperature also leads to increases in the possible electronic temperatures that can be maintained in the system. I've shown the desired absorption properties needed to tailor an absorbing surface to a specific light source and maximize the photothermalization to increase the phononic temperature. Extensive modeling has also allowed for extension of this into predicting what types of nanostructures will provide highest temperatures in experimental measurements.

3. MEASURING PHONONIC AND ELECTRON TEMPERATURE USING RAMAN*

3.1 Introduction

Just as important as methods for computationally determining the temperature of a surface under illumination, there need to be methods for physically measuring that temperature during an experiment. On the macroscale this is a simpler concept, often employing thermocouples that make use of the voltage generated across the junction of two metals from the thermoelectric effect.[76] To produce a meaningful voltage however, there needs to be enough of an area of overlap between the two metals. This makes using thermocouples at the nanoscale quite difficult, though not impossible and such thermocouples for nanoscale systems have been demonstrated.[77, 78, 79]

Alternatives for nanoscale thermometry often include, as in the case of a thermocouple, measuring the temperature dependent response of a material in thermal contact with the material being heated. In some cases this can be done qualitatively such as in the case of solar-thermal water heating with metal nanoarticles in which it is known when the particles reaches at least 100 °C due to the solvent boiling.[35] On a more quantitative side, one possible method is using rare earth metal dopants in nanoparticles or films in order to measure the temperature dependent luminescence.[80, 81, 82, 83] However, this type of sensor is often only responsive over a limited temperature range which can limit their utility in the case of measuring the temperature of nanostructures that can, as we saw in Chapter 2, span

*Part of this chapter is reprinted with permission from "Photothermalization and hot electron dynamics in the steady state" by Nicki Hogan, Shengxiang Wu, and Matthew Sheldon, 2020. Journal of Physical Chemistry C, 124, 4931-4945, Copyright 2020 by the American Chemical Society.

*Part of this chapter is reprinted with permission from "Comparing steady state photothermalization dynamics in copper and gold nanostructures" by Nicki Hogan and Matthew Sheldon, 2020. Journal of Chemical Physics, 152, 061101, Copyright 2020 by the American Institute of Physics.

well over 100's or 1000's of K. Other methods of temperature measurement have included techniques such as electron energy loss spectroscopy,[84, 85] nuclear magnetic ressonance spectroscopy,[86] and electron backscattering.[87] The temperature measurement that will be a focus of this work is the use of the temperature dependence of inellastic scattering in Raman spectroscopy. This has been used as a temperature probe in non-metallic materials with sharp Raman peaks,[88] with more recent developments showing that it can also be done in metals by analyzing the high energy scattering background.[33, 89, 34, 90]

It should be noted that all of these methods exclusively give measure of the phononic temperature of the system. To date, measurement of electronic temperature has been largely limited to TA studies.[91, 92, 93, 94] It is only recently that the hot electron temperature has been probed using CW measurements by considering changes in the Raman scattering signal from the metal's surface.[95]

Here, I focus specifically on Raman spectroscopy as a method for thermometry. I will begin with an introduction into Raman as a technique that measures the phononic temperature of materials with well defined transitions and continue into a discussion of how the signal can also be used to measure the temperature of electrons in equilibrium with the lattice. The focus of the chapter is how existing Raman thermometry techniques can be expanded further to encapsulate the electronic temperature, as well as give a concrete measure of the size of the sub-population of hot electrons in the material. These results are then verified using independent electrical measurements to prove the validity of this model.

3.2 Methods

FABRICATION: To prepare the nanostructures, first a sticking layer of 5 nm of chromium was thermally evaporated onto a silicon wafer followed by 150 nm of gold (Lesker PVD e-beam evaporator). A polymer mask was formed spin coating a layer of 4% 950k PMMA

in anisole (MicroChem) at 3000 rpm for 45 second followed by heating at 180 °C for 90 seconds. Electron beam lithography was performed by exposing this resist to an electron beam using a current of ~0.043 nA with varying exposure time. Development was done at room temperature in a 3:1 IPA:MIBK mixture (Sigma) for 30 seconds. A final layer of gold was thermally evaporated followed by removal of the polymer mask by flash sonication in acetone.

SPECTROSCOPY: Reflection spectra were taken using a WITec RA300 confocal microscope with a 100x 0.9NA objective and a white light source. These spectra were normalized to the source spectrum to obtain the absorptivity. All Raman spectra were obtained in a stage that allowed for both heating, in the case of the silicon and sapphire spectra, and vacuum conditions, in the case of some of the metal anti-Stokes spectra (Linkam TS1500V). Vacuum measurements were performed at a pressure of 0.010 mbar. All samples were illuminated by a 532 nm CW Nd:Yag laser which was focus on the sample using a 50x 0.55NA objective for the silicon and sapphire study and a 20x 0.4NA objective for all metal samples.

ELECTRICAL MEASUREMENTS: Credit for all electrical measurements using my samples goes to a colleague, Shengxiang Wu. The nanostructured gold and an ITO-coated glass slide were secured together in a parallel plate geometry with a 200 μm bilayer spacer composed of Kapton tape (on the ITO side) and copper tape (attached to the gold film surrounding the nanostructures). The sample was placed in the same microscope stage (Linkam TS1500V) and brought to a pressure of 0.010 mbar. A 532 nm CW diode laser was focused on the surface using a 50x 0.55NA objective and electrodes were connected to a source-measure unit (Keithley 2450) to vary the bias during current measurements. The laser light was chopped at 47 Hz and current was measured using a lock-in amplifier (Stanford Research Systems, SR830). Bias voltage was modulated between -0.2 V (accelerating bias) to 1 V (retarding bias) for each optical power.

3.3 Stokes:Anti-Stokes Ratio

Raman spectroscopy provides a measure of the inelastic scattering of photons off a material. The majority of light scattering from the material is elastic, also known as Rayleigh scattering. Raman spectra are traditionally graphed in units of relative cm^{-1} with the Rayleigh peak centered at 0. Inelastic scattering is then broadly divided into categories depending on whether it is higher or lower energy than the Rayleigh peak. Peaks that are of lower energy are Stokes shifted and appear as positive values, and peaks of higher energy are anti-Stokes shifted and are on the negative side of the spectra.

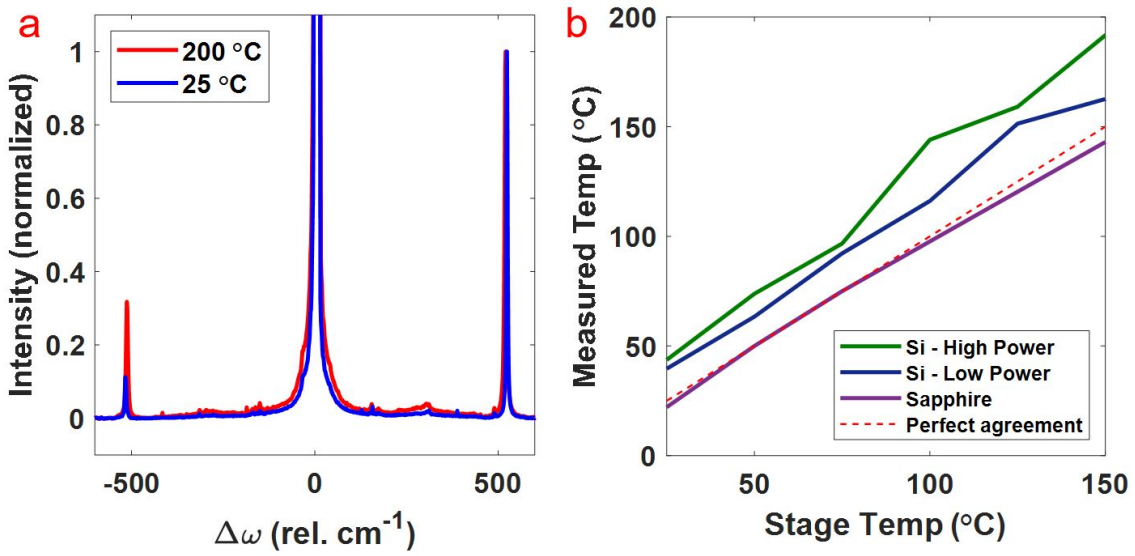

Figure 3.1: (a) The measured Raman spectra taken from a silicon wafer on a heating stage at two temperatures each normalized to the intensity of the Stokes peak at approximately 516 cm^{-1}. In (b) is the calculated temperature of Si as a function of the heating stage for low (1 mW) and high (9.5 mW) laser illumination conditions. For comparison is also the calculated function of a sapphire disk at 9.5 mW illumination.

An actual Raman scattering event occurs through use of a virtual state and involves an electron moving from one vibrational state to a virtual state upon excitation and then

falling back to another vibrational state and scattering the photon in the process. Starting and ending in the same vibrational state will produce Rayleigh scattering. Conversely, starting in an excited state and returning to a lower energy state will produce a photon with greater energy than the incident light and gives anti-Stokes shifted radiation. This happens with lower probability than returning to a higher energy state due to the relatively higher occupation of electrons at lower energy near the ground state. However, this electron occupation is thermally activated and follows a Boltzmann distribution. As the temperature of the material increases, there is increased occupation of higher energy vibrational states and thus an increase in the anti-Stokes intensity. Stokes shifted radiation still dominate, but the ratio between Stokes:anti-Stokes starts to decrease. This can be seen in Figure 3.1a which shows the Raman spectrum from a silicon wafer at two different temperatures. Each peak in the spectrum corresponds to a specific vibrational mode in the material which provides the sharp features. Therefore, it is possible to calculate the temperature of any material by taking a ratio of the Stokes:anti-Stokes peaks according to the following equation, taking into account that Raman intensity is proportional to the fourth power of the energy difference from the Rayleigh line.[88]

$$\exp \frac{-hc\omega_\mu}{kT} = \frac{I_{AS}(\omega_\mu)/(\omega_l - \omega_\mu)^4}{I_S(\omega_\mu)/(\omega_l + \omega_\mu)^4} \tag{3.1}$$

Silicon is an extremely common Raman standard due to the fact that it has a strong, sharp peak close to the Rayleigh line. The further a peak is from the Rayleigh line, the weaker the anti-Stokes signal due to the exponential decrease in occupation of higher energies according to the Boltzmann relationship. I placed a silicon wafer on a heating stage and measure the Stokes:anti-Stokes ratio and calculate the temperature according to Eq. (3.1). The results are shown in Figure 3.1b. Silicon is highly absorbing at 532 nm, therefore there is going to be some photothermalization of the laser light in addition to

scattering. This explains the constant offset from the silicon and the perfect agreement line between the stage and the measured temperature (blue curve). With an order of magnitude increase in applied laser power (green curve), there is a further offset from perfect agreement, demonstrating that the constant increase in temperature is due to laser heating of the silicon. In both cases the slope of the line matches exactly with the slope of perfect agreement implying that if there was no absorption to cause photothermalization there would be no offset. Sapphire is a similar smooth material with sharp Raman peaks near the Rayleigh line, but which additionally has near zero absorption at 532 nm. Switching the silicon for the sapphire disk shows that the measured temperature matches near perfectly with what the heater was set to. This demonstrates the reliability with which the Raman spectra can be used as an indication of sample temperature.

While accurate, this technique does have one very notable limitation. The material must have strong Raman peaks near the Rayleigh line. For a vibrational mode to be Raman active, it must have a change in polarizability. Materials such as metals have no such vibrational modes, and therefore show no Raman peaks.

3.4 Anti-Stokes Raman on Metals: One Temperature Model

While metals do not have clear Raman peaks, they do still have an inelastic scattering signal. An example of this signal is shown in Figure 3.2a. This broad background arises due to interaction of the incident radiation with the electron gas of the metal and therefore can be related back to the energetic distribution of the electrons in the metal.[34] Recent studies suggest this signal may be due to anti-Stokes photoluminscense from the recombination of the short lived photo-excited electron-hole pairs in the metal, rather than a coherent scattering process, as with conventional Raman spectroscopy described above.[34, 96] However, the exact physical origin of the anti-Stokes signal is still under debate, and may be dependent on the specific metal or nanostructure geometry under study.[96] Despite this

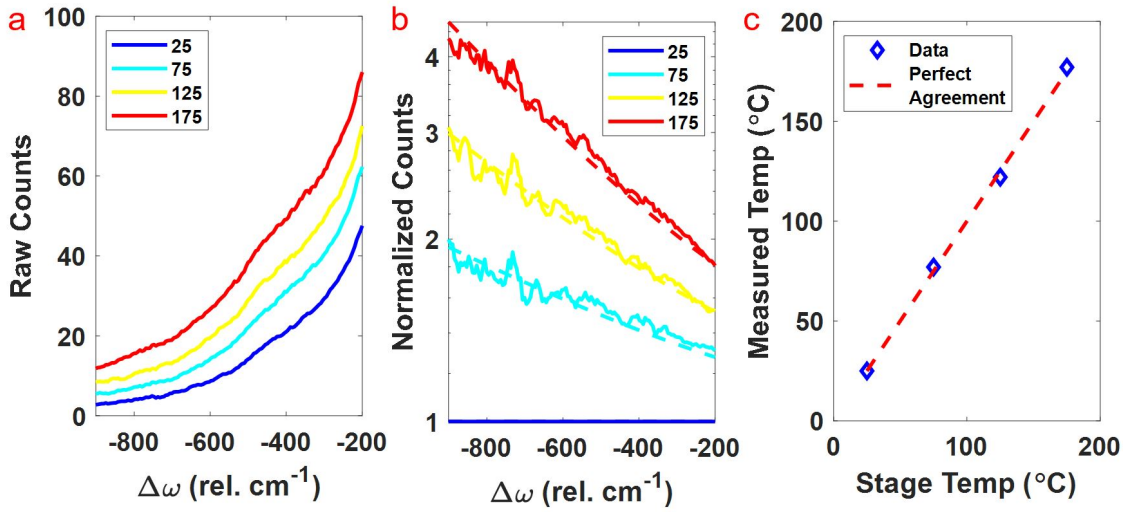

Figure 3.2: (a) The raw anti-Stokes intensity measured from a 100 nm copper film as a function of the stage temperature along with the (b) same data normalized to the lowest temperature spectrum. Dashed lines correspond to the fitted data for each curve. (c) Show the correlation between the measured temperature by this method to the temperature of the stage to show agreement.

uncertainly, it has been well established that this anti-Stokes signal is a reliable reporter of the phononic temperature of the metal.[33, 34, 90] Thus, the Bose-Einstein distribution of the phonon excitation describes the spectral trend:

$$I(\Delta\omega) = C \times D(\Delta\omega) \times \left(\frac{1}{\exp \frac{-hc\Delta\omega}{kT_p} - 1} \right) \tag{3.2}$$

Here, I is the anti-Stokes signal normalized by power and integration time as a function of the energy difference from the Rayleigh line, $\Delta\omega$, and the phononic temperature, T_p. To account for the experimental collection efficiency, a scaling factor, C, is included that is calibrated for each measurement. The density of states of the material, $D(\Delta\omega)$, can be obtained experimentally from a white light reflection spectrum.

Assuming that the scaling factor and density of states are not thermally dependent, it is

actually possible to remove their influence from the equation with a ratiometric approach. An initial spectrum is collected, using a low enough laser power that the temperature of the film can be assumed to be unperturbed by the laser beam. It is then possible to normalize the anti-Stokes spectra taken at higher temperature to that initial room temperature spectra.

$$\frac{I(\Delta\omega)}{I_{298K}(\Delta\omega)} = \frac{\exp\frac{-hc\Delta\omega}{k(298K)} - 1}{\exp\frac{-hc\Delta\omega}{kT_p} - 1} \tag{3.3}$$

The ratio of each spectra to the room temperature spectra (Figure 3.2a, blue curve) is shown in Figure 3.2b. The solid lines correspond to the data itself while dashed lines correspond to the fitted temperatures according to Eq. (3.3). There is only one fit parameter in Eq. (3.3), the phononic temperature, which means there is one unique temperature which describes the data. The comparison of the measured temperature to the temperature of the stage are given in Figure 3.2c. The line that shows perfect agreement between measured temperature and the stage is graphed, as well, to more clearly indicate that this method of using the inelastic scattering is a reliable and accurate way to report the phononic temperature under laser illumination.

3.5 Anti-Stokes Raman on Metals: Two Temperature Model

3.5.1 Developing TTM Model

One problem with this model, is that it only fits the data reliably over a limited energy range, within approximately 1000 cm^{-1} of the Rayleigh line. At higher energy shifts, there are large deviations from Eq. (3.2). To demonstrate this, I fabricated a gold nanostructure which, due to the high plasmonic field enhancement, provides higher signal to noise across the entire spectral range than a smooth film. The geometry of this nanostructure is shown schematically in Figure 3.3a with the corresponding SEM in Figure 3.3b. This geometry was chosen to approximate the selective absorber designs that were modeled in Figure 2.4.

These initial nanostructures are shorter than what was found to be the ideal height for the nanostructures due to limitations in the resist thickness during the lithography process.

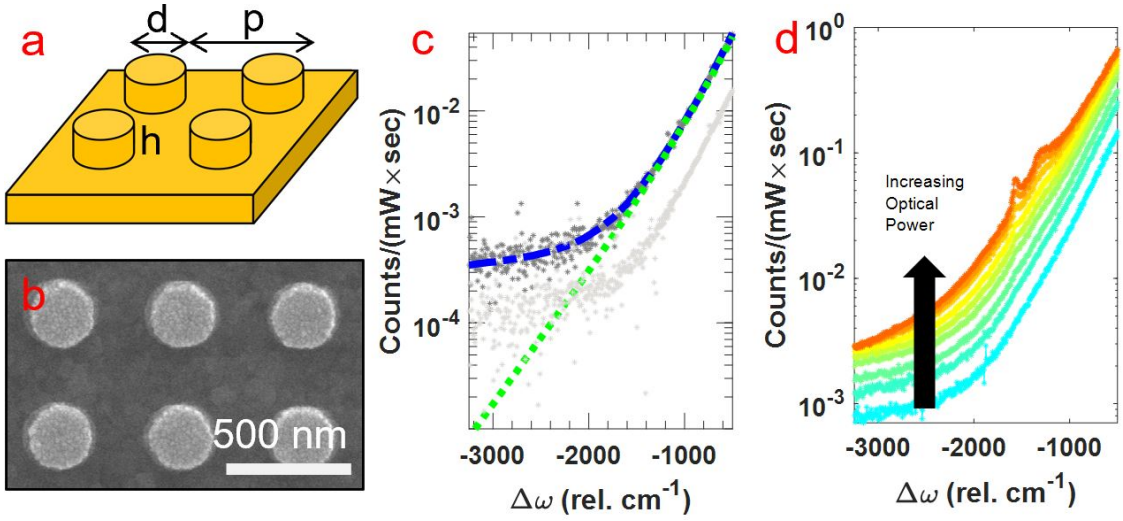

Figure 3.3: (a) Schematic of an gold nanostructure with dimensions h = 100, p = 500nm, and d = 273 nm and (b) the corresponding SEM. (C) A one-temperature fit (T_p = 505 K, green dotted) and a two-temperature fit (T_p = 456 K, T_e = 5523 K, and χ = 1.01 %, blue dashed) for an incident optical power of 4.2×10^8 Wm^{-2} on the gold nanostructure. The weaker signal (light gray dots) is from a smooth gold film. (d) The power dependent anti-Stokes Raman signal with the growth of amorphous carbon peaks around -1500 cm^{-1} at higher powers. The power range spanned is $8 \times 10^8 - 9 \times 10^9$ Wm^{-2}.

Anti-Stokes Raman signal from this nanostructure under illumination with a 532 nm laser at 4.2×10^8 Wm^{-2} is shown in Figure 3.3c in dark gray dots. The one temperature fit to this data is given in the green dotted line and it can be clearly seen that there are increasing deviations from this fit at higher energies. This deviation has been observed several times in both SERS and TERS studies.[34, 95, 89] In those studies, this high energy signal is attributed to the presence of a sustained sub-population of hot electrons in the metal that are at a much elevated temperature in comparison with the majority of the electron bath. Using this knowledge, I built a more consistent physical picture that ex-

plains the Raman signal. First, after optical absorption photo-excited electrons quickly exchange energy with other hot electrons via electron-electron scattering (~fs) to establish a distinct electronic sub-population with a well-defined temperature, T_e. Then, on a longer time scale (~ps) hot electrons within the sub-population equilibrate with the rest of the electron bath at a rate determined by the electron-phonon scattering, to achieve a distribution at temperature T_p. During illumination there will always be present some steady state population of hot electrons that is defined by the optical absorption rate as well as the magnitude of the electron-phonon coupling. Adapting the fitting method of Szczerbiński et al., I find that the additional signal at higher wavenumbers can be accounted for by including an additional term to describe the relative size of the sub-population of hot electrons, χ with temperature, T_e.

$$I(\Delta\omega) = C \times D(\Delta\omega) \times \left(\frac{1-\chi}{\exp\dfrac{-hc\Delta\omega}{kT_p} - 1} + \frac{\chi}{\exp\dfrac{-hc\Delta\omega}{kT_e} + 1} \right) \tag{3.4}$$

Carriers in equilibrium with the lattice probe the phonon distribution and therefore show the Bose-Einstein statistics of lattice excitations, while the hot electron sub-population is described by Fermi-Dirac statistics.[97] Note that the spectra can also be well described assuming that the hot electron populations obeys Boltzmann statistics, and both distributions provide similar trends for the fitted temperatures. The fit to Eq. (3.4) is also plotted in Figure 3.3c (blue dashed) and shows excellent agreement with the data over the entire spectral range. It is no longer possible use a ratiometric fit like was possible for the one temperature model. This is due to not having a way to estimate the electronic temperature of the lowest power spectrum. Instead, I now include the scaling factor, C, as an additional fit parameter. Also shown on the same axes is the signal acquired from a smooth gold film at the same laser power. It can be seen that there is an order of magnitude of decrease in

signal due to the lack of field enhancement, and is consistent with what is commonly seen in SERS measurements.[7]

In Figure 3.3d the entire power dependence of the anti-Stokes scattering obtained across laser powers spanning $8 \times 10^8 - 9 \times 10^9$ Wm^{-2} is given. At higher fluences, greater than 4×10^9 Wm^{-2}, there is the appearance of two peaks in the spectra at -1350 and -1580 cm^{-1} which indicate the formation of amorphous carbon on the surface of the gold. The amorphous carbon signal is commonly observed at high optical fluences in SERS and TERS experiments, and likely results from the photodegredation of trace amounts of organic contaminants that are absorbed to the metal surface during measurements.[95, 98] Data in this wavenumber range is excluded during analysis to prevent artifacts that are not attributed to the gold surface from interfering with the fitting routine.

As understood in an expanded TTM model it is also expected that some contribution to the signal is from non-thermalized electrons. However, based on the optical power densities probed in our experiments, it is likely that the average time between photon absorption events is greater than the timescale of electron-electron scattering. Thus, there is not a significant fraction of the electron population corresponding to the non-thermal component prevalent in the spectra, or $<< 1\%$.

The Raman signal attributed to the hot electrons is very weak compared to the signal from the thermalized electron bath, especially for thin film samples without SERS enhancement. During measurements, it is crucial to eliminate sources of error or other artifacts such as stray lights, or unwanted scattering. Additionally, long integration times of several minutes and a rigorous procedure for assessing the spectral baseline are required to obtain data that can be fitted robustly. I also cannot fully discount other small effects contributing to the signal, such as shifts in the plasmon resonances of the nanostructures due to volume expansion during heating. Nevertheless, I confirm independently using de-

vice measurements reported below in Section 3.6 that the behavior of the hot electrons is consistent with the interpretation of the Raman spectra in accordance with Eq. (3.4).

3.5.2 Power Dependence of Temperature and Hot Electrons

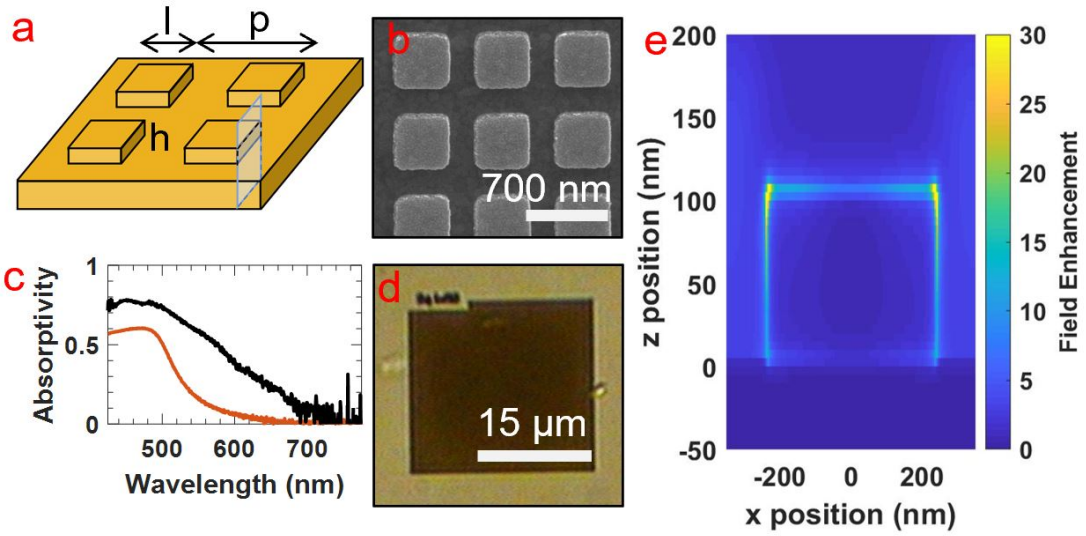

Figure 3.4: (a) Schematic of a periodic structure with strong optical field enhancement for enhancing Raman signal, with l = 225 nm, p = 500 nm, and h = 100 nm on a 150 nm thick gold film. (b) SEM and (d) optical images of the fabricated nanostructure. (c) The absorptivity at normal incidence of the nanostructure (black) compared to a smooth gold film with thickness 150 nm (red). (e) The calculated optical field enhancement on a side face of a nanocube, as depicted in (a). A maximum field enhancement of 47x at the corners is predicted.

The large increase in Raman signal from the nanostructure compared to a smooth gold film in Figure 3.3c is due to the large optical field enhancement provided by the plasmon resonance of the nanoscale cylinders. Given the importance of maximizing the Raman signal to aid interpretation of the electronic and phononic temperature in systematic studies, I turn to a nanostructure design that will maximize local field enhancements, similar

to the design of SERS substrates. It is well established that optical field concentration is strongest at corners and sharp tips in plasmonic absorbers.[6] Indeed a nanocube array shows very high field enhancement at corners, with the geometry shown schematically in Figure 3.4a along with corresponding optical and SEM images in Figure 3.4b and d. With proper tailoring of the geometry, highly absorbing structures can be made that also approximate the selective absorber behavior observed in the pillar geometry in Figure 2.4. Using FDTD simulations, I verified that this nanostructure provides strong broadband absorption and high local field enhancement. As depicted along one face (Figure 3.4e), the nanocube shows nearly 50x field enhancement at the sharp corners compared with the incident optical intensity. The fabricated structure also exhibits strong, broadband absorption in the visible (Figure 3.4c).

Using fits to the anti-Stokes Raman signal, I track the dependence of T_p, T_e, and χ on optical power for the optimized absorber in Figure 3.4 and compare the response with a smooth 150 nm thick gold film. Both samples were fabricated on a silicon wafer substrate. The results from the study of the gold film, with the fitted T_p, T_e, and χ are displayed in Figure 3.5a-c respectively. Due to the weaker Raman signal compared with the nanostructure array, the temperature can only be robustly fit for spectra obtained at a minimum incident laser power of 5×10^8 Wm^{-2}, corresponding to a significant temperature increase in both T_p and T_e. Note that above a T_p of 600 K, I observed the onset of thermal degradation of samples, further limiting the power range that can be measured. Based on Eq. (2.13) the highest phononic temperature an absorber can reach is limited by the magnitude of the $P_{non-radiative}$ term, due to effects such as convection or conduction. In order to understand the role of convection I performed anti-Stokes Raman measurements both in atmosphere and at a vacuum pressure of 0.010 mbar. Indeed, placing the gold film in vacuum significantly increases the T_p that was obtained during absorption, though the sample substrate also provided a conduction pathway of thermal energy away from the sample,

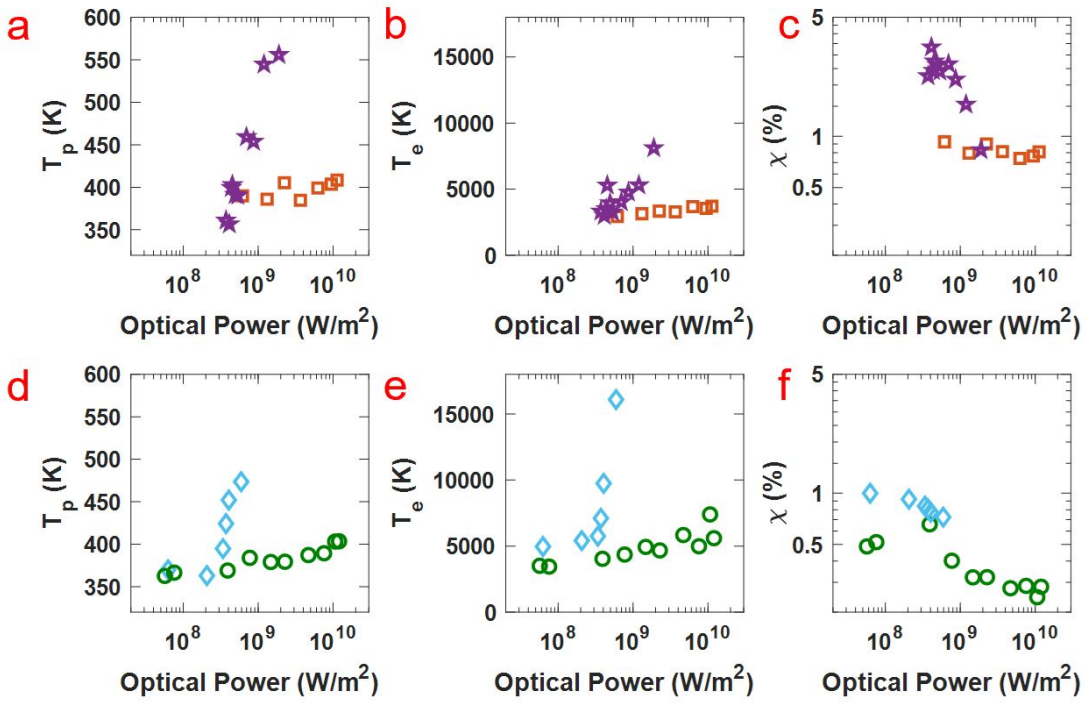

Figure 3.5: (a-c) The fitted values of T_p, T_e, and χ respectively for a 150 nm thick gold film measured in atmosphere (red squares) and in vacuum (purple stars) as a function of incident optical power. (d-f) The fitted values of T_p, T_e, and χ respectively for the gold nanostructure in Figure 3.4 measured in atmosphere (green circles) and in vacuum (blue diamonds).

significantly limiting the photothermal response. Perhaps more striking is the large dependence of T_e on the vacuum pressure, with electronic temperatures in vacuum exceeding those in atmosphere by as much as a factor of 4. This suggests that electronic temperature is also highly dependent on non-radiative loss pathways. It has been well established that gold nanostructures can interact with surface absorbed molecular species in a process known as chemical interface damping (CID).[99, 100] During CID, direct photoexcitation into adsorbate states decreases the plasmon lifetime by introducing another pathway by which it can decay. Given that I see the formation of amorphous carbon under high illumination, there is strong evidence that photoexcited electrons are interacting with adsorbed

molecules from the atmosphere either through CID or hot electron injection. Further, an observed decrease in T_e and χ is consistent with plasmon damping due to CID. A more detailed analysis of both the hot electron lifetime and the electron-phonon coupling is provided below, giving more insight into the nature of electron relaxation pathways.

Moreover, there is a monotonic increase in temperature with increasing laser power, with the magnitude of electronic temperature in both atmosphere and vacuum exceeding the phononic temperature by well over an order of magnitude. This is expected due to the ~$100\times$ smaller heat capacity of the electron gas compared to the lattice,[32] and this difference between electronic and phononic temperature has also been observed in TA studies.[89, 91, 92, 93, 94] Interestingly, I find that in both environments there is an inverse relationship between the trend in T_e and χ as the optical intensity is increased, though the trend is more pronounced when the thin film is in vacuum. It has also been established in TA studies and computational studies that there is an increase in electron-phonon coupling as electron temperature increases, resulting in faster rates of electron relaxation.[101] I similarly interpret the observed trend in χ as resulting from an increase in the rate of hot electron relaxation with temperature that outcompetes the increase in the excitation rate of hot electrons at higher laser fluences.

An analysis of the nanostructure described in Figure 3.4 with the fitted values of T_p, T_e, and χ is displayed in Figure 3.5d-f respectively. A benefit of measurements performed on nanostructures is that the field enhancement provides an increase in signal, allowing more reliable spectra at lower optical powers and decreased noise. Both in atmosphere and under vacuum, T_p and T_e are larger in comparison with the gold film at equivalent optical power, due to the increase in absorbance. However, the onset of thermal degradation occurred at somewhat lower phononic temperatures in vacuum compared with the gold film, limiting the high power range of the study. Even still, the electronic temperatures reached are nearly twice as high as the gold film at the highest optical powers.

Additionally, the nanostructure shows the same inverse relationship between T_e and χ. The much higher electronic temperature entails that the nanostructures exhibit a relatively smaller sub-population of hot electrons at the same optical powers compared with the film. However, for equivalent values of T_e the nanostructure exhibits a larger χ that the thin film, when the samples are in atmosphere. Again, this can be interpreted as resulting from changes in the electron-phonon coupling that depends on environmental factors and geometry, as is described in detail in following sections.

With the insight provided by the anti-Stokes Raman analysis, it is possible to adapt the traditional TTM given in Eq. (1.5) in order to account for the steady state behavior of the metal when it is absorbing optical power, P_{abs}. Crucially, the expression now includes a specific dependence on the size of the hot electron sub-population, χ. In Eq. (1.5) both $\frac{\partial C_e T_e}{\partial t}$ and $G(T_e - T_p)$ refer to heat transfer rates between different sub-populations in the material, and both are extensive quantities that are scaled by χ in order to accurately describe the amount of electrons participating in the thermalization process. Further, T_e refers only to the temperature of electrons within the hot electron sub-population:

$$\chi C_e \frac{\partial T_e}{\partial t} = \Delta[k_e \Delta T_e] - \chi G(T_e - T_p) + P_{abs} \tag{3.5}$$

In the steady state, the time derivative goes to zero allowing for a description for T_e in terms of the phononic temperature of the system as can be obtained from fitting the anti-Stokes Raman spectra. If local thermal gradients are neglected, then

$$T_e = T_p + \frac{P_{abs}}{\chi G} \tag{3.6}$$

The electronic temperature is larger than the phononic temperature by an additional term that accounts for the power absorbed and the electron-phonon coupling constant, G. Further, increases in electronic temperature are expected to correlate with decreases

in χ, as observed in Raman measurements. If the electron-phonon coupling observed in TA studies is also representative of electron dynamics in this regime of steady state absorption, I can make specific predictions about how electronic temperature depends on phononic temperature. Assuming a χ of 1%, a conservative estimate based on the data measured in Figure 3.5, and assuming a G of 10^{13} $\mathrm{Wm^{-3}K^{-1}}$, based on calculated and reported values for nanoscale gold,[97] when a gold thin film is absorbing solar illumination, Eq. (3.6) predicts that the steady state temperature difference between phononic and electronic temperature is only a few degrees. However, all three terms that define the increase in electronic temperature with respect to the phononic temperature, χ, G, and P_{abs} are modified by the geometry of the nanoscale absorber in our studies. In Chapter 2, I demonstrated how to design a nanostructure that has optimized absorption for maximizing T_p and P_{abs} which leads to an increase in T_e as calculated by Eq. (3.6). Another consequence of careful choice of geometry is that the optical absorption can be strongly enhanced at electromagnetic hot spots, thus effectively increasing P_{abs} locally even further in the structure, sometimes by orders of magnitude compared with the incident optical intensity. Further, in addition to the trends in χ that depend on optical power and environment as reported above, I will show later in Chapter 4 how structural features of the nanoscale absorber relate to the size of χ, and the electron-phonon coupling constant as determined by Raman measurements, thereby also providing new insight into the factors that determine the rate at which electrons thermalize with the bath. Therefore, the hot electron temperature that can be sustained in the steady state is informed by systematic analysis of the anti-Stokes Raman signal, in combination with more well-established design considerations for locally enhancing optical fields.

It is important to emphasize the distinct features of the steady state TTM model described above and the corresponding physical picture provided by the anti-Stokes Raman analysis in comparison with the traditional TTM from TA studies. In particular, it is not

usually suggested in TA studies that the electron population in the metal can be separated into two separate populations, each with well-defined temperatures. Rather, in time resolved experiments it is believe that after an optical pulse, all conduction electrons in the metal thermalize through electron-electron scattering to reach a uniform elevated temperature, before thermalizing with the lattice via electron-phonon scattering. Second, the Raman signal indicates a fractional size of the population of hot electrons that seems incredibly large, especially in light of the very short (~ps) lifetime of photo-excited electrons. That said, the high energy tail of the anti-Stokes Raman spectra is clear in several reports,[34, 95] and this work as well as others have consistently presented evidence for sustained hot electron populations on the order of ~1 % with temperatures > 1000 K during optical pumping across similar intensities.[95]

3.5.3 Error Analysis

Given that fitting to Eq. (3.4) involves four fit parameters with data across several orders of magnitude, there is not a straightforward method for assessing the statistical error or, perhaps more important, the quantitative accuracy of the results of the fitting. However, it is necessary to provide some measure of whether trends observed are outside the error in the measurement technique. To this purpose, I devise two methods for analyzing the error. The first is to determine the statistical error in the fitting routine, and the second is to determine the experimental error as given by the spread in the fitted data from the same sample across several measurements.

As a measure of the error intrinsic to the fitting routine, I calculated the percent difference between each experimental data point and the fitted value according to Eq. (3.4). For demonstration, I show the data as calculated from a gold nanostructure in Figure 3.6. The region from -500 to -1000 cm^{-1} is mostly characteristic of the phononic temperature while the region from -2500 to -4000 cm^{-1} is dominated by the electronic temperature.

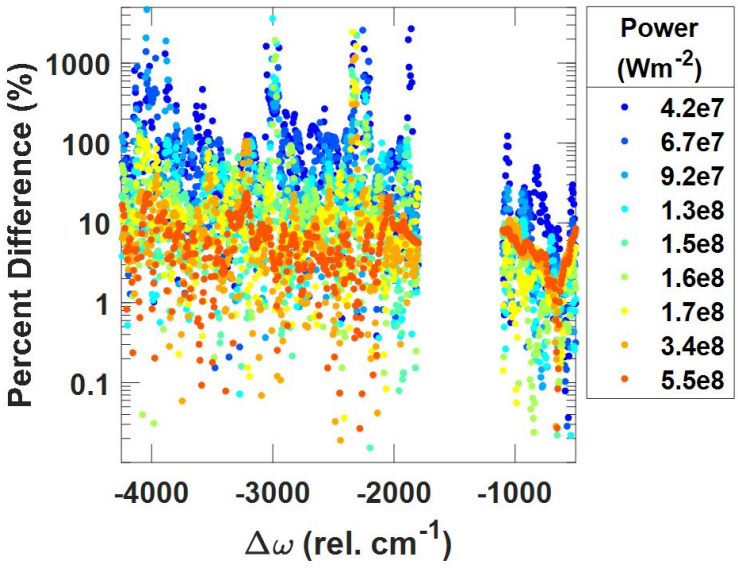

Figure 3.6: The absolute value of the percent difference between the experimental data and the corresponding fits as a function of the wavenumber for a gold nanostructure at a variety of powers. Data between -1100 and -1800 cm^{-1} is omitted due to the amorphous carbon peaks.

The average percent difference across the lower wavenumber region corresponding to the phononic temperature is 3.3 %, while it is much higher for the electronic temperature region, or about 26.4 %. Percent difference, and thus error, is highest in the electronic region of the spectrum where there was the lowest signal to noise.

I can also quantify the error for experimental measurements by collecting the Raman signal both from different nanostructures but also different positions in each nanostructure array. I used a series of gold nanocubes which had a pitch of 700 nm, height of 100 nm, and an edge length that varies. The signal was collected from four different positions in each different array. Using this data I calculated T_p, T_e, and χ for each point as shown in Figure 3.7. From these measurements, it can be calculated that across the range of samples and measurements, the error is ± 7 K for the phononic temperature, ± 275 K for the electronic temperature, and ± 0.11 % for χ. Both strategies of error analysis suggest a

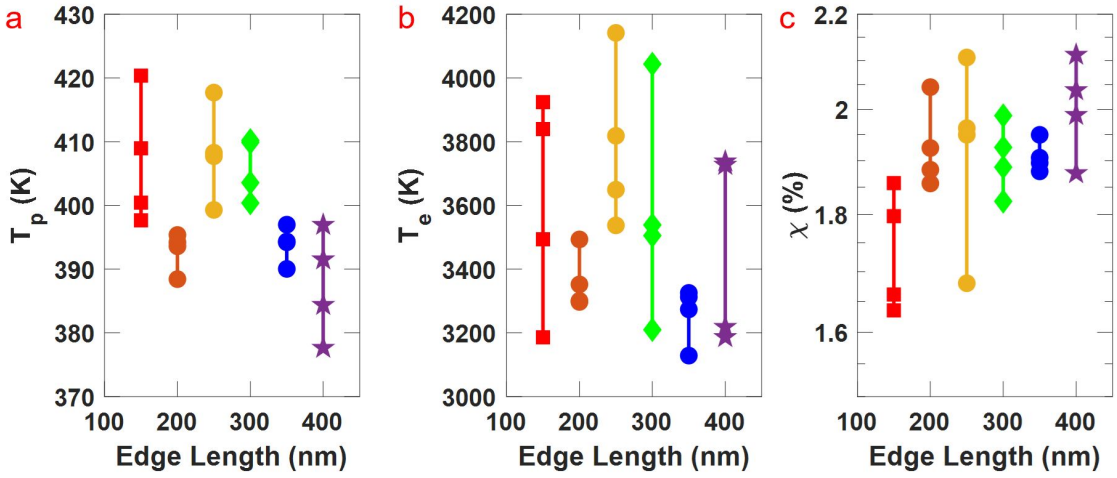

Figure 3.7: The fitted values of T_p (a), T_e (b), and χ (c) for a series of six different gold nanostructures which followed the schematic in Figure 3.4 with a pitch of 700 nm and height of 100 nm and varying edge lengths. The data points for each nanostructure were taken at the same power at different positions on the array.

similar accuracy for our fitting routine.

One other possible source of error that can be introduced during the fitting routine arises due to the number of fit parameters along with the method used to solve for them. I used a type of linear least squares analysis that solved for the set of variables that minimized the sum of the squares of the difference between the data and the fit. This type of fitting routine requires an initial guess for each of the fit parameters and it is possible to fall into a local minimum in the solution space, similar to local maxima that could have been found during the particle swarm optimization in Chapter 2. Similarly to that case, by starting with dozens of initial guesses and then taking the absolute minimum solved for using each combination allows for finding the global minimum and therefore the true best fit to the data. Code demonstrating this fitting procedure is given in Appendix C.

3.5.4 Hot Electron Lifetime and Electron-Phonon Coupling

Using the analysis of the Raman data summarized in Figure 3.5, it is possible to further provide more detailed information about both the electron-phonon coupling constant, G, and a quantity, τ, that indicates the average lifetime an excited electron resides in the hot electron sub-population. The average lifetime of hot electrons within the elevated temperature distribution can be understood by comparing the size of the steady state sub-population of hot electrons with the rate of hot electron generation. If it is assumed that every absorbed photon produces a transiently excited electron, then

$$\tau = \frac{\chi \rho V}{N \alpha} \tag{3.7}$$

where ρ is the electron density of gold,[102] V is the volume of the metal interacting with the light, N is the incident number of photons per second, and α is the experimentally measured absorptivity at normal incidence at 532 nm, and χ is the fractional hot electron population from the anti-Stokes Raman fit. The interaction volume in these calculations is based on an estimate of where the absorption is localized in the nanostructures as determined from optical simulations, similar to the depiction in Figure 3.4e. However, the actual interaction volume in the nanostructures is a complicated function of the local field concentration provided by the plasmonic resonances, and thus may be a source of a systematic offset in the reported values for τ given here. As can be seen in Figure 3.8a, for all four data sets there is a monotonic decrease in τ as the incident optical power in increased. This decrease in the lifetime with optical power can be interpreted as resulting from thermal activation of the rate of coupling between the hot electrons and the phonons. This interpretation is further supported by the analysis of the electron-phonon coupling constant that follows. Further, samples under vacuum show significantly longer τ that those at atmospheric pressure. I hypothesize that this difference may be due to surface

collisions with gas molecules or absorbed contaminates in atmosphere. The observation of the formation of amorphous carbon at higher optical power provides further evidence that electrons interact with surface species during illumination. With careful experimental design, trends in lifetime and hot electron population may allow these measurements to further distinguish mechanisms of hot electron injection or CID.[95, 99, 100]

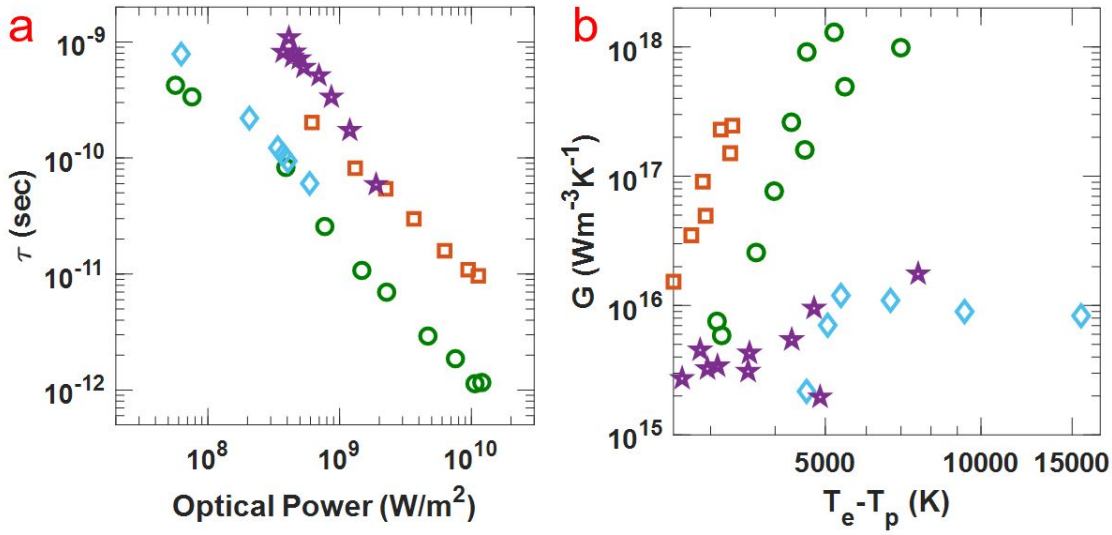

Figure 3.8: (a) Calculated lifetime and (b) coupling constant for the nanostructure under vacuum (blue diamonds), nanostructure in atmosphere (green circles), gold film under vacuum (purple stars), and a gold film in atmosphere (red squares).

However, what is very striking is the large range of τ observed, spanning three orders of magnitude. Remarkably, the data suggests that at the lowest optical powers studied, the hot electrons have high kinetic energy for nearly a nanosecond before thermalizing to the phononic temperature. At the highest optical powers, more directly comparable to the optical intensities employed in ultrafast TA studies, I see values for τ that are very similar to the lifetime values of 1-10 ps that are standardly reported for gold.[103, 91] While the comparison between the separate experiments is interesting, I caution that more

insight is required to fully interpret this data. In particular, the strong field concentration at electromagnetic hot spots may entail that hot electrons absorb photons multiple times before relaxing, thereby increasing their average lifetime during steady state excitation. As confirmed in electrical device measurements below, the large, sustained population of energetic hot electrons provided by the prolonged lifetime is advantageous for application in devices. The longer an electron has high energy, the higher chance it has to participate in chemical reactions or be used in energy conversion applications. However, if optical fluence is decreased further, below our detection limits in this study, the time between photon absorption events will begin to exceed the lifetime of a hot electron established in TA measurements, and therefore the lifetime may show a more complex dependence on decreasing power.

Further analysis of χ allows us to determine the electron-phonon coupling constant, G, independently from the lifetime as shown in Figure 3.8b. As described in Eq. (3.6), all of the fit parameters from the anti-Stokes Raman analysis allow unique determination of G based on the absorbed power into the volume of the metal interacting with the incident light. Unlike the analysis for lifetime, calculation of G requires quantification of the volumetric power absorbed, $P_{V,abs}$, in terms of the incident power, $P_{incident}$. Thus $P_{V,abs} = \dfrac{P_{incident} \times \alpha(normal, 532nm)}{V}$. I have shown that at atmospheric pressure there are significant environmental contributions to the hot electron lifetime, implying that G accounts for coupling to all relaxation pathways. However, in vacuum it is expected that electron-phonon coupling will dominate relaxation. For all examples there is an increase in G as a function of the electronic temperature, in agreement with *ab initio* calculation and experimental studies.[101] Notably, in atmosphere the gold thin film exhibits a larger G than the nanostructure at the same optical power. In vacuum the environmental influences are minimized, and within the spread of the data, the nanostructure and film show an equivalent coupling constant that agrees with calculated values for gold.[91, 92, 104]

We hypothesize this trend in G is due to a decrease in the active surface area with hot electrons, likely localized near electromagnetic hot spots, and that only molecular collisions in these locations contribute to relaxation. The net result is that the nanostructure achieves much greater T_e under equivalent optical power, and further, hot electrons have longer lifetimes compared with films at the same T_e in atmosphere. Both behaviors may be desirable in device that take advantage of hot electrons, and my results suggest optical designs that decrease the relative volume in which hot electrons are generated can further optimize this response.

3.6 Thermionic Measurements

To lend credence to the steady state TTM developed to describe the anti-Stokes Raman measurements, an independent measurement of the temperature and size of the hot electron population was devised. This technique measures the hot electrons directly by constructing a thermionic converter device. A thermionic converter is an electrical device in which a metal cathode is heated to high temperatures (> 1000's K) so that some electrons in the cathode have kinetic energy in excess of the work function, W. These electrons are emitted across a vacuum gap and collected at an anode. Instead of conventional heating, I fabricated a cathode that is plasmonically structured to be highly absorbing so that optical excitation induces heating via photothermalization. If the incident radiation has insufficient energy to promote direct photoemission via the photoelectric effect, i.e. $h\nu < W$, then the electrical signal due to vacuum emission provides information about the energetic distribution of the electrons in the cathode. Importantly, the electrons need to be at extremely elevated temperature to observe any thermionic signal, and neither our anti-Stokes Raman analysis nor other experiments[105] suggest that optical excitation can provide the increases in phononic temperature of metals that would support thermionic emission, especially without inducing melting or vaporization of the metal.

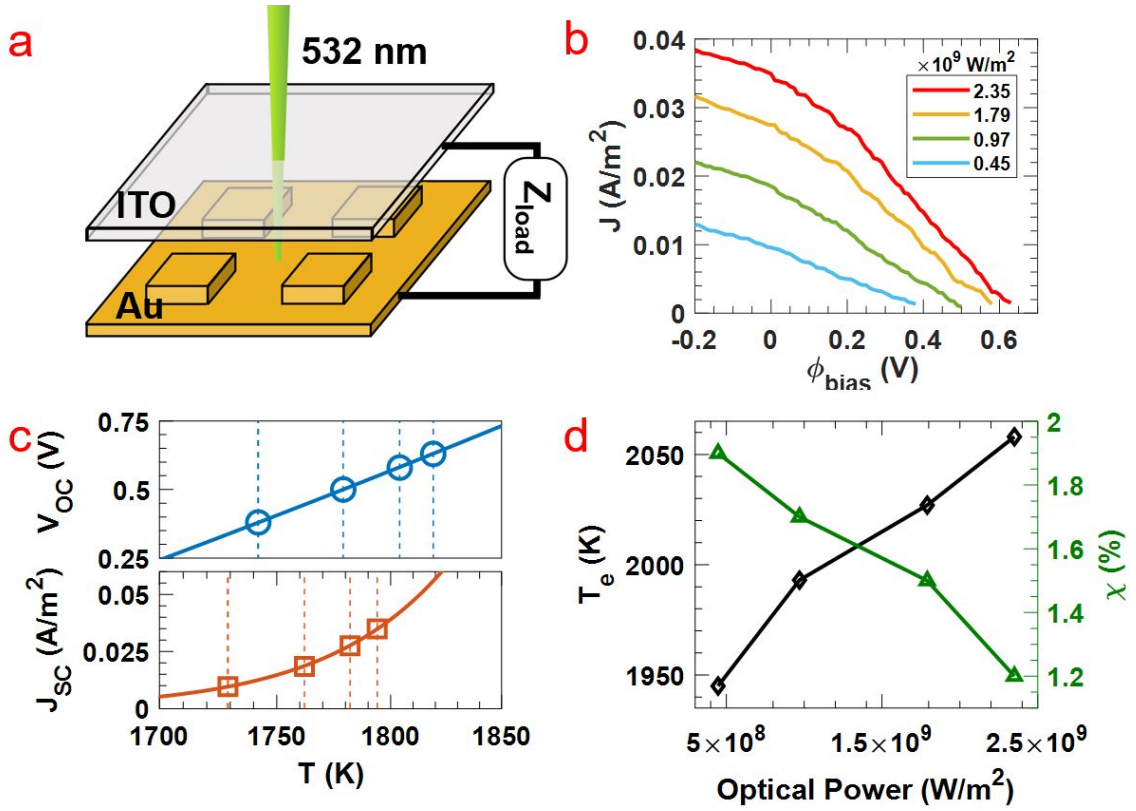

Figure 3.9: (a) A schematic of the thermionic device composed of a gold nanostructure and ITO-coated glass slide. (b) The measured J-V curves as a function of incident optical power. (c) The fitted temperatures calculated assuming a one temperature model based on V_{OC} (top) or based on J_{SC} (bottom). (d) The fitted trend in T_e and χ solved using a two temperature model.

I constructed a thermionic device using the gold nanostructure depicted in Figure 3.4 as the cathode with an ITO anode separated by 200 μm, and placed the device under vacuum (0.010 mbar). The sample was excited with 532 nm CW laser excitation, and the electrical signal was measured using lock-in amplification, as depicted in Figure 3.9a. The current-voltage (J-V) response of the device is shown in Figure 3.9b. As laser power is increased, there is both an increase in the measured short circuit current, J_{SC}, as well as the open circuit voltage, V_{OC}. Note that, because the ITO anode provides no reverse thermionic current in the experiment, the current exponentially approaches zero against an

increasing bias. Therefore, the reported V_{OC} corresponds to the maximum applied voltage that still allowed lock-in detection of the current. Given that the phononic temperature of the metal is too low to provide any electrons with kinetic energy sufficient for vacuum emission, I interpret the electrical signal as resulting only from the hot electrons in the cathode. The electrical signal can be understood in terms of Richardson's equation for thermionic emission, which I have adapted to account for the steady state TTM model.

$$J = \chi A T_e^2 \exp \frac{-(W + \phi_{bias} + \phi_{SC})}{kT_e}) \tag{3.8}$$

This equation relates the thermionic current density, J, to a retarding applied voltage, ϕ_{bias}, taking into account the work function of gold, W = 5.1 eV,[106] and the Richardson constant, A. It is also necessary to include a term to account for the space charge potential in the vacuum gap, ϕ_{SC}, which was estimated from Langmuir's space charge theory for a parallel plate geometry.[107] I assume that only the fraction of electrons in the metal, χ, at the hot electron temperature T_e give rise to the vacuum emission. Removing the dependence on χ and assuming that all electrons are at one uniform temperature, T, reproduces the standard Richardson equation.

This expression connects the J-V curves of the device with the temperature and population of the hot electrons in the cathode, and an analysis of the trends in V_{OC} and J_{SC} indicates that a TTM is required to accurately describe the electrical data. As summarized in Figure 3.9c, there is a discrepancy in the fitted temperature based on the J_{SC} compared with the temperature fit by analysis of the V_{OC}, if it is assumed that the entire electron gas is at a uniform temperature. However, for any incident optical power there is a unique combination of χ and T_e that consistently reproduces the trends in J_{SC} and V_{OC} when input into Eq. (3.8). In Figure 3.9d, I report these values, and show that the electrical data has the same inverse relationship between T_e and χ, in agreement with the trends observed

during the anti-Stokes Raman analysis of the same nanostructure. Additionally, both χ and T_e are approximately the same order of magnitude as measured by the different techniques, though the fitted electrical data indicates a somewhat lower value of T_e than the Raman studies at comparable optical power. I believe that difficulties in accurately modeling the more complex space charge field of the nanostructure may be the largest source of the discrepancy between the fitted values for T_e in the separate experiments.

3.7 Summary and Future Direction

In this chapter I showed how it is possible to use the anti-Stokes Raman signal as a probe electrons at the steady state phononic and electronic temperature as well as to measure the size of the hot electron sub-population in a metal. Using these numbers it is possible to determine the electron-phonon coupling constant and the lifetime of the hot electrons, which give insight into how the hot electrons behave under steady state illumination. It was found that while phononic and electronic temperature were of the same order of magnitude seen in ultrafast pump-probe measurements, the lifetime I measured was several orders of magnitude longer. This gives important insights into how steady state measurements may differ from TA studies. In order to verify these results, I constructed a thermionic device to measure the emission due to the hot electrons and found similar values for size and temperature of the hot electron sub-population.

While this anti-Stokes technique does seem to well describe the data and offer a new picture of hot electron dynamics in the steady state, there is room for further refinement. In these experiments the optical excitation wavelength of 532 nm served also as the probe of temperature. I believe it could be useful to decouple these two and perform a steady state pump-probe experiment where the probe is a low intensity non-perturbative 532 nm laser, and the pump could be at a different intensity and color to heat the sample. It is possible that in the extremely high power limits, this type of set up could offer insights

not only into electron-phonon interactions, but also give information about the electron-electron scattering interactions prior to thermalization. This would in essence allow us to create a steady state version of the expanded TTM that has already been described in TA studies.[36, 40, 41] Additionally, it would be possible to begin to explore if there was a spectra dependence to the hot electron dynamics.

4. TUNING TEMPERATURE AND HOT ELECTRON DYNAMICS*

4.1 Introduction

After developing a methodology for predicting the phononic temperature of a nanostructure based on its absorptivity and then demonstrating that it was possible to measure both phononic and electronic temperature, I can now make use of these techniques to start rationally designing nanostructures for specific device applications. While it was possible to measure electronic temperature prior using TA studies, those measurements use a pulsed source. Many device applications require CW excitation, and it was not yet clearly determined if there are differences in the hot electron dynamics between pulsed and CW illumination. This is of interest for understanding if hot electrons can utilized before relaxation in applications such as optical energy conversion,[24, 108] photodetection,[109] or photocatalysis.[110, 111]

As discussed in Section 3.6, one of the applications I have already explored is a thermionic power converter built using a nanostructure array as the cathode. In this type of device, the efficiency can be improved by increasing the electronic temperature such that the hot electrons have sufficient kinetic energy to overcome the work function of the material. While there are theoretical models to predict phononic temperature, as I showed in Chapter 2, it is extremely computationally expensive to do the same with electronic

*Part of this chapter is reprinted with permission from "Photothermalization and hot electron dynamics in the steady state" by Nicki Hogan, Shengxiang Wu, and Matthew Sheldon, 2020. Journal of Physical Chemistry C, 124, 4931-4945, Copyright 2020 by the American Chemical Society.

*Part of this chapter is reprinted with permission from "Comparing steady state photothermalization dynamics in copper and gold nanostructures" by Nicki Hogan and Matthew Sheldon, 2020. Journal of Chemical Physics, 152, 061101, Copyright 2020 by the American Institute of Physics.

*Part of this chapter is reprinted with permission from "Hot electron emission in plasmonic thermionic converters" by Shengxiang Wu, Nicki Hogan, and Matthew Sheldon, 2019. ACS Energy Letters, 4, 2508-2513, Copyright 2019 by the American Chemical Society.

temperature and is only practical in the case of nanoparticles (< 100 nm).[112] With the ability to now measure the electronic temperature in conditions comparable to what would be needed to operate these type of optoelectronic devices, namely low intensity CW illumination, it is possible to start understanding what types of nanostructure geometries would have the highest temperatures and highest chance of performing well in a thermionic power converter.

Another application that shows much promise is in taking advantage of high energy hot electrons for photocatalysis. Several metals with known catalytic activity have been explored for this purpose, albeit mostly with low efficiency to date, including gold,[111, 113] silver,[114, 115] and copper.[116] A variety of reactions have been demonstrated including CO_2 reduction,[117, 118] water splitting,[119, 120] and ammonia generation,[121] as well as more sophisticated chemistry using plasmonic antenna-reactor hybrid systems.[39] Perhaps of special interest are nanostructure made from copper. Copper has a lower cost as compared to other plasmonic metals, but does not sacrifice any of the tunablility in the plasmon resonance.[122, 123] Additionally, copper is currently one of the best-performing electrocatalysts for CO_2 reduction, suggesting that the high chemical potential of the photogenerated hot carriers may be used to drive the same reduction chemistry.[124] With the technique developed in Chapter 3, differences in the hot electron dynamics in copper nanostructures versus gold nanostructure such as differences in energetic distribution or lifetime of the hot electrons could be probed to understand which metals may be most beneficial for various application.

In this chapter, I explore how changes in the lateral dimensions of a nanostructure as well as its composition changes the hot electron dynamics. This is done with the goal of informing design of nanostructures with the ideal properties for use in a variety of applications.

4.2 Methods

FABRICATION: Nanostructures in Sections 4.3.1 and 4.4 were fabricated using the same method discussed in Chapter 3.

Nanostructures in Section 4.3.2 were fabricated on commercially available TEM grids (Ted Pella) with windows coated in 50 nm thick films of silicon nitride. On these grids, 5 nm of chromium followed by 150 nm of gold was thermally evaporated (Lesker PVD e-beam evaporator). The grid was secured to a 2x2 cm glass slide using a 10% PMMA in toluene solution which was let dry overnight to allow for spin coating of the small TEM grid. To improve electron beam lithography resolution and aid in liftoff of the polymer mask, a bilayer resist process was developed. A first layer of PMMA/MMA 9% in ethyl lactate (MicroChem) was spin coated at 3000 rpm for 45 second followed by heating at 165 °C for 90 seconds. Then a top layer was added by spin coating a layer of 2% 950k PMMA in anisole (MicroChem) also at 3000 rpm and heating at 180 °C for 90 seconds. The resist was exposed to an electron beam and developed in room temperature 3:1 IPA:MIBK (Sigma) for 30 seconds. Removal of both the polymer mask and the PMMA layer securing the TEM grid to the glass slide was done by soaking in acetone for several days. Etching away of the gold was done in a Xe source FIB instrument (Tescan FERA-3).

SPECTROSCOPY and ELECTRICAL MEASUREMENTS: All data was taken using the same conditions as discussed in Chapter 3.

4.3 Changing Nanostructure Geometry

4.3.1 Modifying Nanostructure Dimensions

Given the large dependence on geometry shown between a film and a nanostructure, perhaps one of the simplest parameters to systematically analyze is changing the dimensions of the nanostructure. It has been well established that changing the dimension of a nanostructure can be used to shift the plasmon resonance and change the absorption

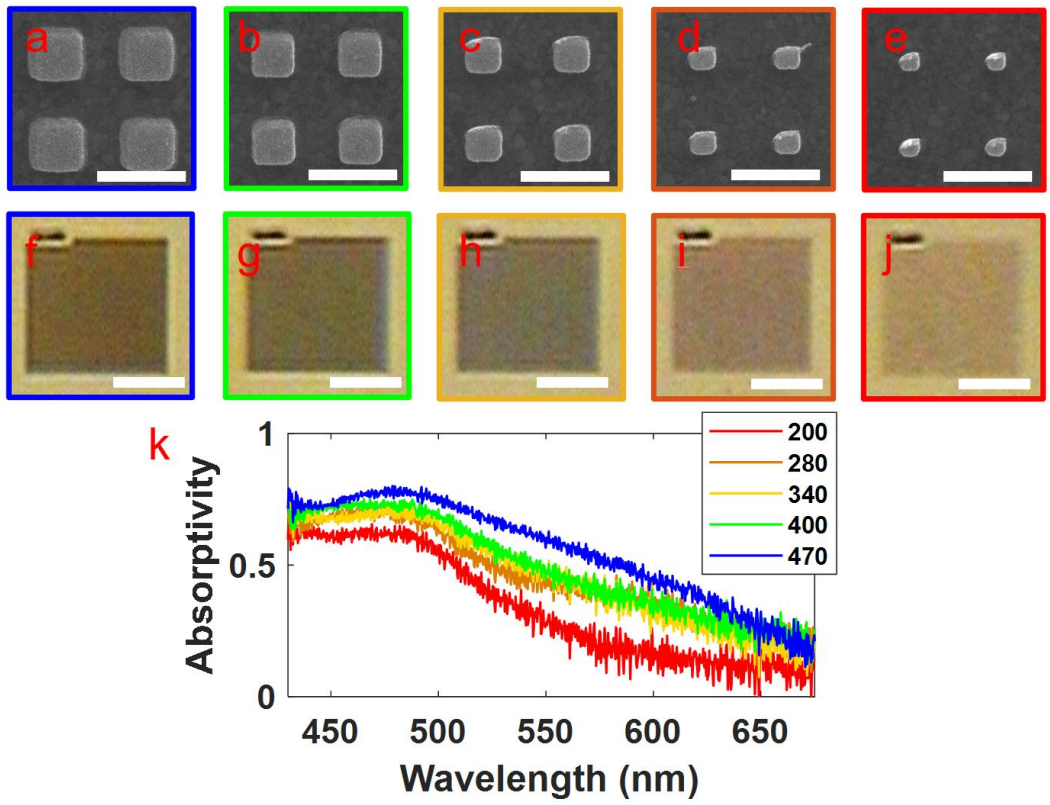

Figure 4.1: (a-e) SEMs of gold nanostructure is a constant pitch of 700 nm and height of 100 nm, and an edge length of 470, 400, 340, 280, 200 nm respectively. Scale bar is 700 nm in each SEM. (f-j) Optical images of each nanostructure in (a-e), all scale bars are 15 μm. (k) The measured absorptivity of each nanostructure in (a-e).

properties. To start, I fabricated a series of nanostructures in gold that have the general nanocube geometry shown in Figure 3.4a with a height of 100 nm, pitch of 700 nm, and varying edge lengths of 470, 400, 340, 280, and 200 nm. These nanostructures are shown in SEMs (Figure 4.1a-e) and optical images (Figure 4.1f-j) in order of decreasing edge length.

It can be seen from the optical images that as the nanocubes decrease in size, there is decreasing broadband absorption. This can be seen in Figure 4.1k where the absorptivity for each nanostructure array is shown. At 532 nm specifically, there is approximately a

factor of 2 difference in the amount of incident power absorbed. In order to account for these differences, during the Raman measurements the amount of power applied to the nanostructure arrays was modulated in a way such that there was an equivalent amount of power absorbed. In this way, the trends observed give insight into how the geometry alone affects the hot electron behavior. The power absorbed by each nanostructure was 2.8×10^8 Wm^{-2} at 532 nm, with measurements being done in atmosphere.

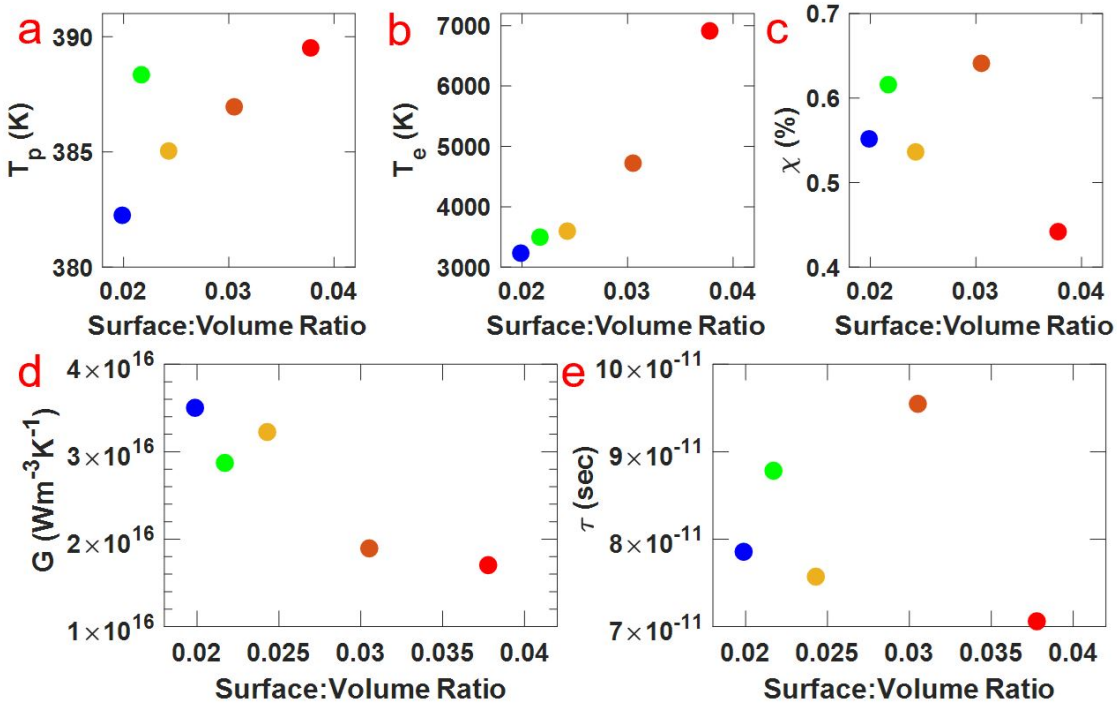

Figure 4.2: The calculated T_p (a), T_e (b), χ (c), G (d), and τ (e) for each nanostructure shown in Figure 4.1a-e as a function of their surface:volume ratio.

The fit to parameters T_p, T_e, χ, G, and τ from Eqs. (3.4), (3.6), and (3.7) described in Chapter 3 are given in Figure 4.2a-e. I found an increase in T_p and T_e with increasing surface to volume ratio. Equivalently, smaller nanostructures reach higher temperature when absorbing the same optical power. As above, T_e is systematically larger than T_p. Increases

in the electronic temperature may also be correlated with a decrease in the hot electron population, χ, as reported above. However as with the trend in lifetime, τ, interpretation of the signals in Figure 4.2c and 4.2e is difficult due to the spread in the data, and may be effectively constant across the size range of the samples studies. As predicted, I also found that the coupling constant, G, decreases with increasing surface to volume ratio. This indicates that smaller nanostructures provide better isolation from environmental factors that accelerate the relaxation of hot electrons. In combination with the increase in T_e, these results suggest that applications taking advantage of hot electrons may need to trade off the higher electronic temperature provided by the more localized hot spots in smaller structures, against better access to hot electrons produced in larger structures with less localization.

4.3.2 Changing Substrate and Nanostructure Design

It was discussed in Chapter 2 that all of the calculations of temperature were done assuming no non-radiative losses such as conduction and convection. While methods of minimizing those two factors were discussed, experimentally to this point there has been no major effort is reach the limit of minimal non-radiative losses. As demonstrated in Figure 3.5, a vacuum environment of 0.010 mbar minimizes losses to convection and increases both phononic and electronic temperature. This vacuum pressure was limited by what was attainable in our experimental configuration, though to truly minimize convection it would be necessary to run experiments at ultrahigh vacuum pressures ($> 10^{-7}$ mbar).

Minimizing conduction requires additional fabrication steps. I targeted a nanostructure design shown schematically in Figure 4.3a. The nanostructure is fabricated using thermal deposition of a metal film followed by electron beam lithography as has been described in the methods section, however instead of fabricating on a silicon wafer, lithography is performed on a commercially available TEM grid that has windows which are covered

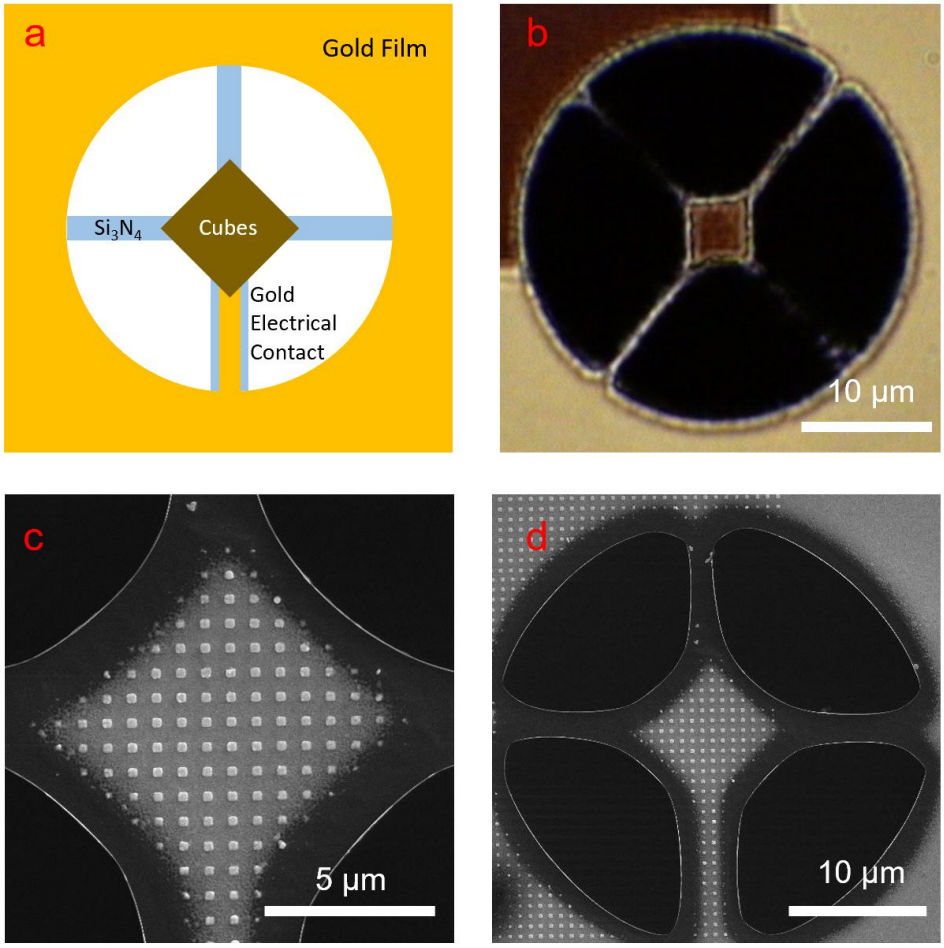

Figure 4.3: (a) Schematic of a nanostucture design that minimizes convection losses along with an optical image (b) as well as a the SEM of the active area (c) and the entire structure (d).

with a 50 nm thick silicon nitride film. Nanostructures fabricated over these windows will lose minimal thermal energy into the substrate. However, there is still lateral conduction into the metal film that was deposited beneath the nanocubes themselves. Lateral conduction can be minimized by etching using a focused ion beam (FIB) instrument around the nanostructure to disconnect it from the surrounding substrate so that the nanostructure in the center is only connected to the rest of the TEM grid by small bridges. I used a Xe source FIB instrument to minimize intercollation of the large Xe ions into the metal lattice,

which could change the refractive index. The metal on these bridges can then be etched away leaving only the silicon nitride. Silicon nitride is an insulator and has a thermal conductivity that is is several orders of magnitude lower than gold.[101] Assuming that the optical spot is larger than the nanostructure array in the center, there is no metal not being heated, and therefore conduction away from the structure is only possible through those thin bridges. A structure following this design scheme is shown in Figure 4.3b-d in optical and SEM images.

This method does successfully minimize non-radiative loss pathways, however it is no longer possible to use the anti-Stokes Raman thermometry method in order to measure the hot electron dynamics. Raman is inherently a low efficiency process, which is why SERS has been so widely adopted. However, this does mean there is a minimum laser power at which there is sufficient signal collected by the detector in order to reliably analyze both phononic and electronic temperature. This minimum power is what set the lower bound of data presented in Figure 3.5 and 4.7. However, the lowest laser power from which I could reliably measure temperature in those cases, approximately 10^8 Wm^2, was already increasing the temperature of the isolated nanostructures well above the point of thermal degradation, which was observed in non-isolated samples for phononic temperatures greater than 600 K. Therefore, qualitatively it is clear the isolation is serving to cut down non-radiative losses and increase temperature, but to get a more quantitative measure it is necessary to utilize electrical measurements.

On a 50 nm thick silicon nitride membrane on a TEM grid, a gold nanostructure was fabricated according to the schematic in Figure 4.4a with dimension of l = 160 nm, p = 380 nm, and h = 100 nm on a 150 nm thick gold film. The corresponding SEM image for this nanostructure is shown in Figure 4.4b with the absorptivity as compared to a gold film is given in Figure 4.4e. The surrounding membrane is etched away, and the gold on three of the silicon nitride bridges is etched away completely. However, due to this being an

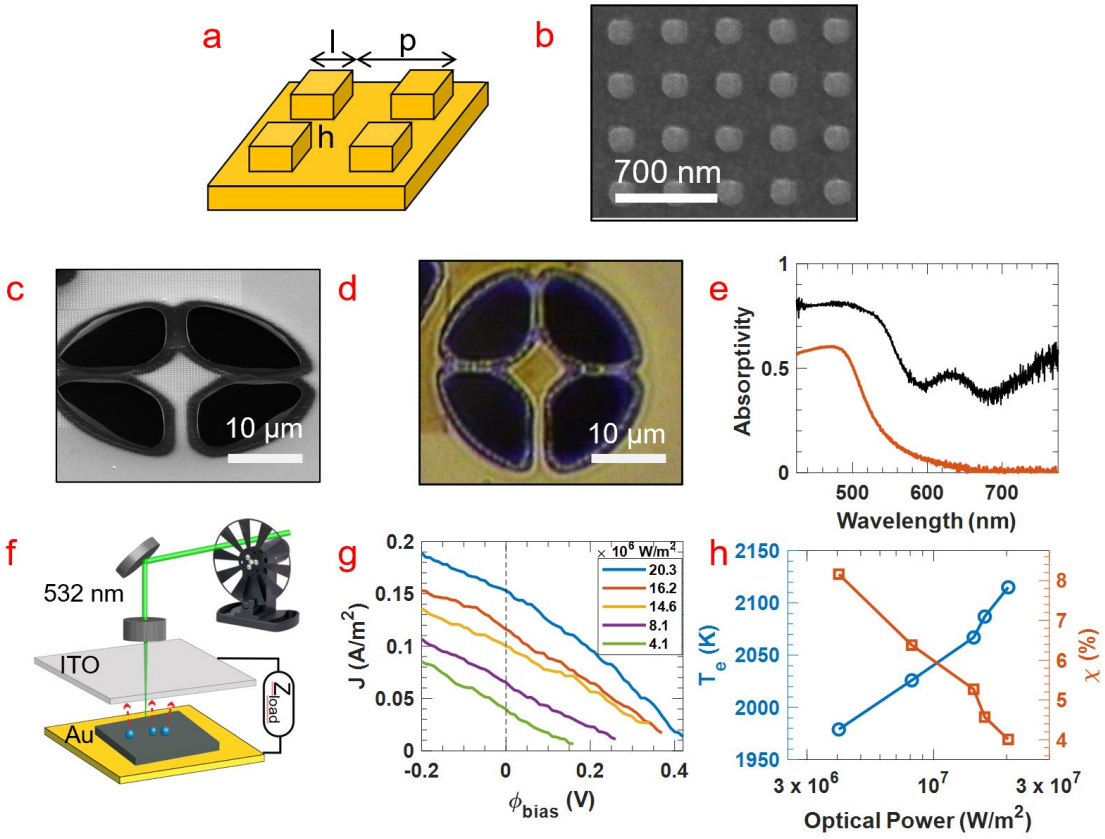

Figure 4.4: (a) Schematic and (b) SEM of a gold nanocube array with l = 160 nm, p = 380 nm, and h = 100 nm. (c) and (d) show the entire isolated nanostructure area after FIB milling of the surrounding substrate. The absorption of this nanostructure array (black) is shown as compared to a gold film (red). The generalized schematic of the thermionic device is shown in (f) along with the power dependent J-V curves in (g). The calculated T_e and χ are given in (h).

electric device there needs to be electrical contact between the nanostructured array and the wire soldered to the TEM grid. For this reason one of the bridges is left with a gold film on it, though this film is made to be as narrow as possible to minimize possible thermal conduction away from the nanostructure. The remaining nanostructured area measures approximately 6x6 μm. The SEM (Figure 4.4c) and optical image (Figure 4.4d) show the end product.

This isolated nanostructure was then used as the cathode in a thermionic power con-

verter with an ITO-coated glass slide as the counter electrode. Chopped 532 nm light was applied and signal was collected through a lock-in amplification scheme, as shown schematically in Figure 4.4f. The measured current-voltage, J-V, curves are given in Figure 4.4g. As was the case in earlier measurements, there was a monotonic increase in both J_{SC} and V_{OC} as the applied power increased. Electronic temperature and fraction of the hot electrons calculated using Eq. (3.8) using these values of J_{SC} and V_{OC} are graphed as a function of applied power in Figure 4.4h. While electronic temperatures are comparable to what was observed previously in non-isolated nanostructures, it is done at powers with are 2 orders of magnitude lower in intensity. It is also noted that even despite the lower fluences, χ is nearly 4$\times$ higher than what was observed previously. This is approaching the power regime which is comparable to what has been achieved in solar-thermal power conversion schemes, where solar concentration factors are commonly between 1500$\times$ and 4000$\times$. Despite the promise for solar applications, the device as it currently is fabricated has an optical power conversion efficiency of 10^{-8} % at these fluences. This is largely due to the extremely large work function of gold, W = 5.1 eV. However methods could be devised to improve this device even further by lowering the work function of the surface and decreasing the space charge effect.[125, 126, 127]

4.4 Changing Nanostructure Material

Another simple to change parameter is what metal the nanostructure is fabricated from. There are a variety of plasmonic metals with individual benefits. For example, gold is frequently used in photothermal applications, where as copper is often used in catalytic applications. It is now possible to explore differences in the hot electron behavior in each of these metals in order to understand for which applications each might be more well suited.

I used electron beam lithography to fabricate nanostructures of the same geometry

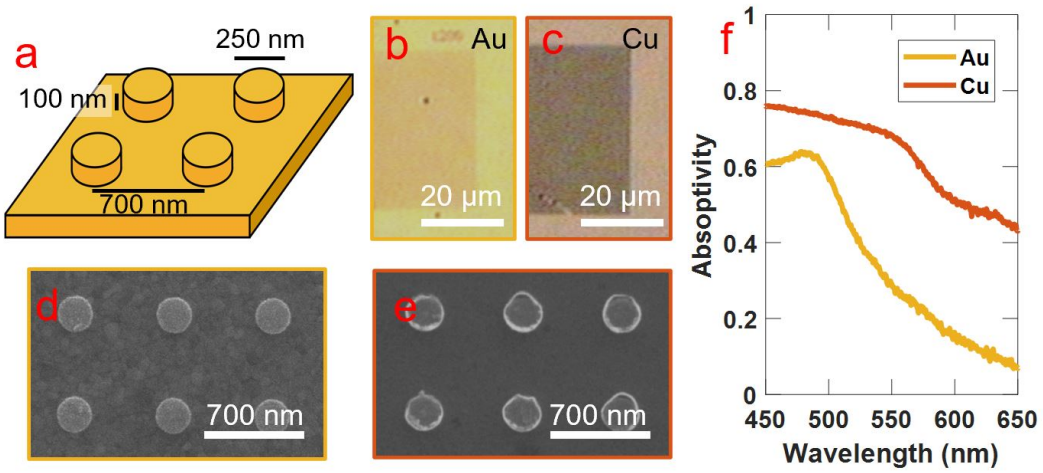

Figure 4.5: (a) A schematic of the fabricated nanostructure with a pitch of 700 nm, height of 100 nm, and cylinder diameter of 250 nm on top of the film with thickness 150 nm. Optical and SEM images of the nanostructure are shown in (b), (d) for gold and (c), (e) for copper respectively. (f) The absorptivity of the two nanostructures.

made from both metals. This should help to avoid differences in their surface to volume ratio that were identified in the prior section from affecting the temperature and coupling constant of the nanostructure array. The chosen nanostructure consisted of nanopillars with a diameter of 250 nm, height of 100 nm, and a pitch of 700 nm on a metal film of 150 nm as shown schematically in Figure 4.5a. Optical and SEM images of the nanostructures are displayed in Figure 4.5b-e. Both the gold and copper nanostructure arrays are more absorbing that their respective films, however the copper nanostructure array is approximately twice as absorbing as the gold nanostructure array for this particular geometry. The benefit of studying nanostructures, rather than smooth films, is that the nanostructures provide extremely large SERS enhancement, as was discussed earlier. This enhancement ensures maximum signal to noise and the ability to measure the hot electron dynamics over a wider power range.

I show the power-dependent series of anti-Stokes Raman spectra for both gold and cop-

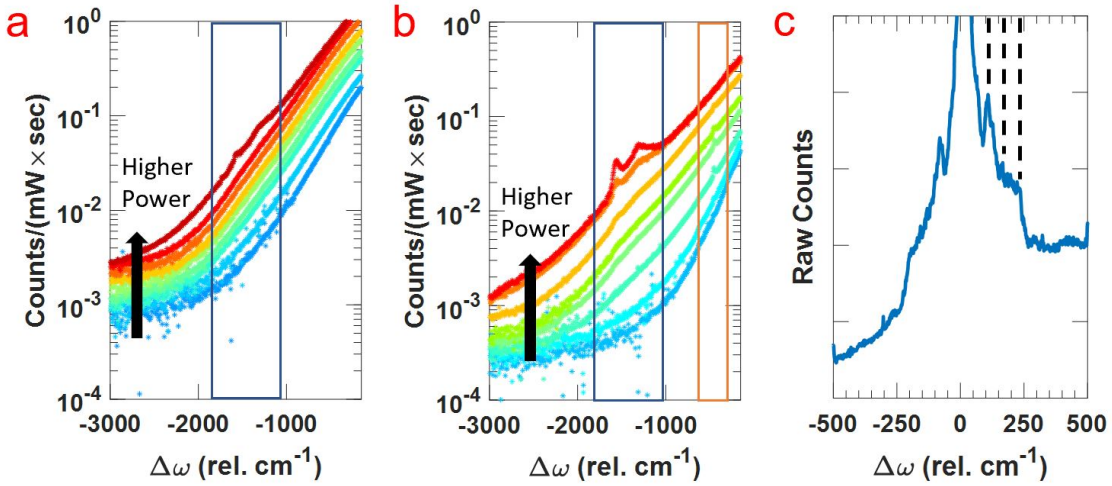

Figure 4.6: The power dependent trends of the Raman signal from the gold (a) and copper (b) nanostructure arrays over a power range of 1.5×10^8 - 1.0×10^{10} Wm^2. The blue box indicates the spectral region of amorphous carbon peaks and the orange box indications the spectral region of copper oxide. In (c) the zoomed in spectra of the species of copper oxide formed at high incident powers, Cu_2O.

per nanostructures in Figure 4.6a and 4.6b, respectively, over the same range of incident optical powers. At higher fluences, in both metals, two peaks grow in at -1350 and -1585 cm^{-1}. This signal is due to the formation of amorphous carbon on the surface, and has been observed previously in TERS and other SERS studies.[95, 98] In gold these peaks are less pronounced, especially at lower powers, however this signal is much more apparent from the copper samples. This is a qualitative indication that the copper is reacting more readily with organic impurities in the vacuum atmosphere that have adsorbed onto the metal surface.

An additional feature in the copper signal is due to the formation of copper oxide at elevated temperatures during photothermalization. This peak can be seen growing in at -485 cm^{-1} and corresponds to the formation of Cu_4O_3.[128] At higher laser powers, this peak disappears and is replaced by broader peaks at -60-200 cm^{-1} due to the formation of Cu_2O replacing the Cu_4O_3.[128] This is more clearly visible on the Stokes side of the

spectrum as seen in Figure 4.6c. This reduction of the copper oxide on the surface may well be the result of hot electron injection from the metal into the oxide at higher optical fluences. I note that measurements were performed in a vacuum atmosphere of 0.010 mbar in order to minimize the formation of these oxide peaks, and to improve signal-to-noise further for the Raman spectral analysis.

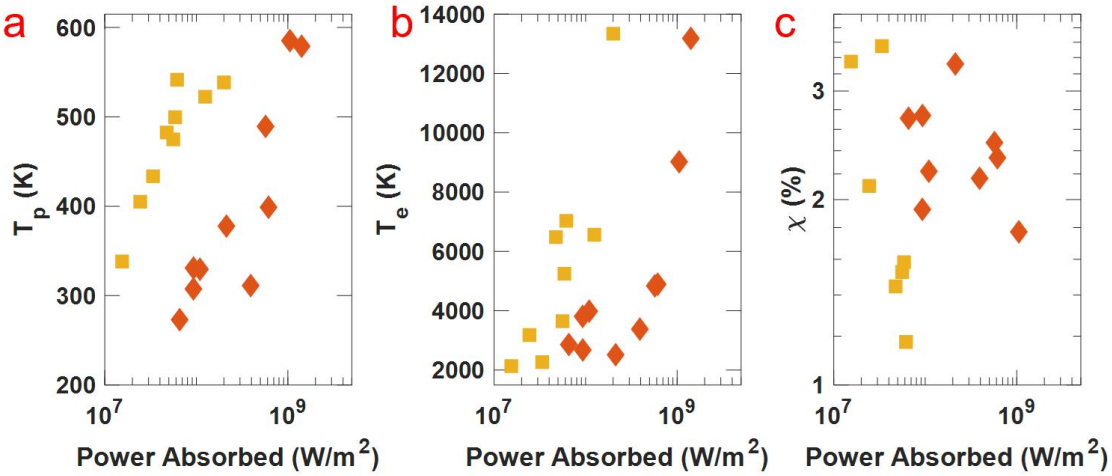

Figure 4.7: Fitted values of T_p, T_e, and χ are shown in (a), (b), and (c) respectively for gold (in gold squares) and copper (in orange diamonds).

I used Eq. (3.4) to calculate T_p, T_e and χ as a function of the power absorbed, shown in Figure 4.7a-c respectively for both gold and copper. As with the different sizes of nanostructure I removed the influence of the fact that the copper is twice as absorbing as the gold at 532 nm by graphing instead against power absorbed versus incident power. When graphed in terms of incident power, there is no meaningful difference in the observed trends. As with the gold nanostructures shown previously, the copper nanostructure also shows signs of thermal degredation when T_p exceeds 600 K, providing an upper limit for the optical power that could be studied.

For both nanostructures, there is a monotonic increase in both T_p and T_e as the power absorbed increases. At the same power absorbed, the gold nanostructure reaches T_p that is 200 K in excess of the copper. The gold also reached a higher T_e than the copper. As observed earlier, there is still an inverse relationship between the electronic temperature and the size of the hot electron sub-population in copper as well as gold. This can once again be explained as a thermal activation of electron-phonon coupling above electronic temperatures of 2000 K. I observed that the copper nanostructure has a higher percentage of hot electrons compared to the gold nanostructure at the same powers.

From these values, I can once again extend the understanding of the system by calculating the coupling constant, G, from Eq. (3.6). In the traditional TTM, G is interpreted specifically as an electron-phonon coupling constant that is an intrinsic property of the metal. In the limit that this experiment could be performed in ultra-high vacuum, the G solved for would be this intrinsic electron-phonon coupling of the metals. This is because the only way a hot electron could lose its energy and return from T_e to T_p would be through electron-phonon coupling, assuming negligible photoluminescence. Thermal energy transfer to a substrate could also impact the relaxation dynamics, if the nanostructure and substrate are strongly vibrationally coupled.[129] However, at the relatively low vacuum pressure in my study, I understand that multiple additional relaxation pathways exist for the hot electrons. Specifically that the hot electrons can participate in chemical reactions with surface adsorbates and gas molecules. Indeed, in Section 3.5.4 I showed that moving a gold nanostructure from vacuum to ambient atmospheric pressure increased the coupling constant, G, dramatically by 2 orders of magnitude at an electronic temperature of 10,000 K, due to increased interaction with chemical adsorbates and gas molecules in the environment. Thus, trends in G, as shown here, also serve as an indication of trends in the chemical reactivity of hot electrons with surface absorbed species. This interpretation is further supported by the observation of the formation of amorphous carbon and copper

oxide when samples are subjected to higher laser fluence.

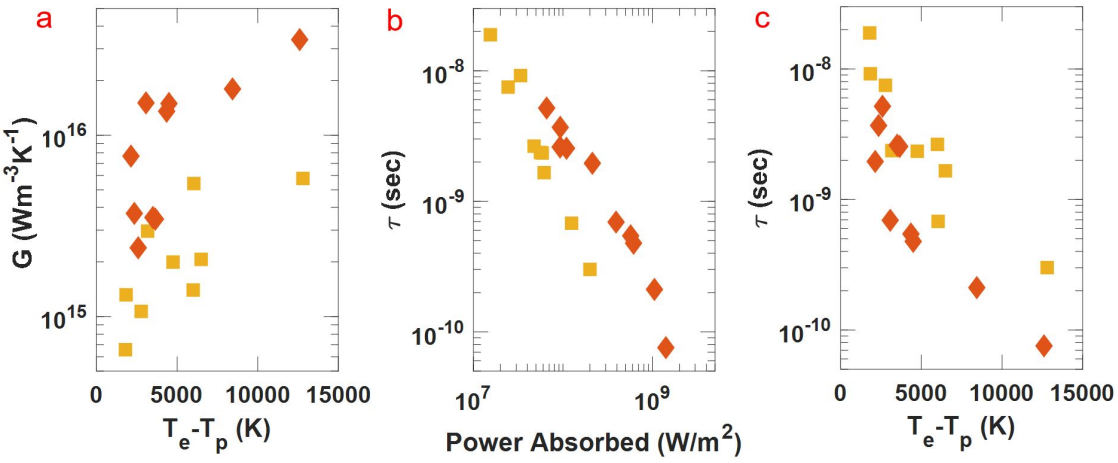

Figure 4.8: (a) Coupling constant, G, as a function of the temperature difference between T_e and T_p. (b) The hot electron lifetime as a function of absorbed power and (c) as a function of the temperature difference for gold (gold squares) and copper (orange diamonds).

The fitted values of G are plotted in Figure 4.8a for both the copper and gold as a function of the temperature difference between T_e and T_p. The magnitude of G is thermally activated.[101] Because the gold and copper reached different temperature when the same optical power was absorbed, I compared the trends in G when hot electrons have the same degree of excitation compared with the metal lattice. Under these more equivalent conditions, I found the coupling constant for copper is higher than that for gold. This implies that the hot electrons in the copper are more reactive that those in gold and thus are more likely to participate in chemistry at the copper surface, even thought both populations of hot electrons in the separate metals are at the same temperature. Again, this interpretation is supported by the larger amounts of deposited amorphous carbon and greater copper oxidation indicated by the Raman spectra. Given that the hot electrons in copper are using their energy to participate in chemistry, rather than increase the temperature of the system,

this can also explain why the copper obtains a drastically lower phononic and electronic temperature than gold when the same optical power is absorbed.

Additionally, in Figure 4.8b I present the hot electron lifetimes calculated used Eq. (3.7) as a function of the power absorbed by the nanostructure. For any given power the copper has a significantly longer lifetime than the gold. This is at first surprising, since trends in G suggest the hot electrons in copper are more reactive and thus are expected to be shorter-lived. However, this apparent contradiction is resolved when lifetime is analyzed in terms of the temperature difference between the hot electrons and the lattice, as seen in Figure 4.8c. As mentioned above, the rate of hot electron relaxation is thermally activated, and the large differences in lifetimes between hot electrons in copper and gold reflect the significantly higher temperature gold reaches compared to copper when absorbing the same optical power. When hot electrons at the same temperature are compared, I see that hot electrons in copper are indeed shorter lived by approximately half an order of magnitude, consistent with the interpretation that the hot electrons in copper are more likely to relax by participating in surface chemical reactions. Future experiments with samples in ulta-high vacuum can also be used to deduce how much of the difference in lifetime may be due to the intrinsic differences between the electron-phonon coupling in the metals, when there are not relaxation pathways provided by surface adsorbates.

4.5 Summary and Future Directions

Using the above studies, it is now possible to begin rational design of nanostructures for a variety of plasmonic hot electron applications without resorting to lengthy fabrication of test structures without ideal properties or time intensive calculations to predict behavior. To begin, I showed that by tuning surface to volume ratio of nanocube arrays it was possible to change the electronic temperature and coupling constant by over a factor of 2. It showed that while smaller structures reached higher temperatures from better isolation

from environmental relaxation pathways, that needs to be balanced against better access to the hot electrons given in larger structures. Through further removing relaxation pathways by isolating the nanostructures from the substrate and surrounding film it was possible to increase temperature and the size of the hot electron sub-population even further to give meaningful thermionic current at fluences comparable to concentrated solar radiation. Another important design parameter that can be changed is the metal used in fabrication of the nanostructure, for which I compared two common plasmonic metals: copper and gold. It was discovered that copper had a larger population of hot electrons that more efficiently coupled to the environment, which has promising implications for the use of copper nanostructures in photocatalysis, while gold reached much higher temperatures, which is more promising for thermal applications.

These results are the beginning of more expansive studies to explore hot electron dynamics under CW illumination. One promising avenue is to explore the behavior of the hot electrons not only in copper and gold, but also in a variety of other plasmonic metals. Silver is an extremely common plasmonic metal that is popular is SERS studies due to the strength of its resonances and large electromagnetic field enhancement.[7] Perhaps most interesting, however, is that under high laser illumination, silver nanostructures luminesce,[130, 131] something that was not observed in gold or copper. Understanding this property and how it relates to the two temperature model developed using anti-Stokes Raman spectroscopy may give better insights into if hot electrons are responsible for this behavior and how it may be utilized in practical applications.

Another important direction would be to consider the dependence of hot electron behavior on the electromagnetic field enhancement around hot spots in the nanostructure. I proposed that the reason the smaller nanostructures in Figure 4.2 reached higher temperatures was due to the smaller localized hot spots being isolated from the environment. Given this knowledge it would be possible to design nanostructures with smaller, or per-

haps with more, electromagnetic hot spots, which may increase the temperature or size of the hot electron sub-population. I began with the simplest geometry, nanocubes, due to ease of fabrication and also due to the knowledge that corners would provide for higher field enhancement. There have, however, been more complex structures which have been designed with many sharp corners for maximum field enhancement, one example being nanostars used in SERS studies,[132, 133] which if studied could provide more information on how hot electron dynamics are related to electric field enhancement.

5. CONCLUSION

I began by showing how it was possible to predict the phononic temperature of a material based on its absorption and emission properties. Through Planck's law, it is possible to calculate power emitted by a surface as a function of the emissivity and the spectrally dependent intensity of the source. Of specific interest is what the limits in temperature are, based on various experimentally attainable emissivity functions under solar radiation. It was found that by both restricting the emission at long wavelengths and at oblique angles, it is theoretically possible to reach phononic temperatures well in excess of 2000 K. Using simulations it is then possible to use those ideal emissivity functions in order to design real nanostructures showing those properties that can theoretically reach temperatures nearly at the melting point of the material. Thermal degradation is an upper limit for temperatures allowed in real nanostructures, even if the calculations show that further restriction may allow for higher temperatures. There is still room for further improvement in the nanostructure design, however, given that minimizing thermal emission becomes even more important when alternate loss pathways, such as conduction or convection, are included that will bring temperature down further.

Having designed structures to reach high temperatures, it was then necessary to develop a thermometry technique with which I could confirm the temperature of the surface. I showed that a broad inelastic scattering signal found in anti-Stokes Raman spectra is thermally activated and can be fit to a thermal distribution that describes not only the electrons in equilibrium with the phonons at the lattice temperature, but also gives information about the hot electrons, including the size of the hot electron sub-population and the electronic temperature. In order to verify these values, thermionic power converters using the hot electrons were fabricated to independently confirm the size of the hot

electron sub-population. Further analysis shows that information can be gained about the electron-phonon coupling and the lifetime of hot electrons, information that was previously predominately measured in ultrafast TA measurements. The values I measured were of comparable magnitude to what was found in pulsed studies, but I was able to show that, in the limit of lower powers not able to be reached in TA spectroscopy, hot electrons are extremely long lived by several orders of magnitude. This has promising applications for using hot electrons in devices under low intensity illumination such as solar fluences.

Just as design of nanostructures to maximize phononic temperature was shown, I ended by showing the ways to consider maximizing electronic temperature or modifying the hot electron dynamics by considering changes in the nanostructure. The data presented here showed how electronic temperature changes based on the size of the nanostructure, and additionally its isolation from the environment. Furthermore, the metal composing the nanostructure also plays a large role in the hot electron populations. This can be seen in copper and gold, where gold showed higher temperatures as opposed to more reactive hot electrons in copper. This merely scratches the surface of possible studies that can be done to further explore dependence of temperature on more complex geometries, electric field enhancement, or color of excitation.

In conclusion, I've given some insight into the steady state temperature and hot electron behavior in plasmonic metal nanostructures. While the two temperature model has been well established in pulsed pump-probe experiments, continuous wave excitation is of particular interest due to its use in applications such as energy conversion and catalysis. A better understanding of how these nanostructures behave under illumination can open the pathway for better rational design of nanostructures for use in emerging applications.

REFERENCES

[1] J. M. Pitarke, V. M. Silkin, E. V. Chulkov, and P. M. Echenique, "Theory of surface plasmons and surface-plasmon polaritons," *Reports on Progress in Physics*, vol. 70, pp. 1–87, 1 2007.

[2] K. A. Willets and R. P. Van Duyne, "Localized surface plasmon resonance spectroscopy and sensing," *Annual Review of Physical Chemistry*, vol. 58, no. 1, pp. 267–297, 2007.

[3] E. Kretschmann and H. Raether, "Radiative decay of non radiative surface plasmons excited by light," *Zeitschrift für Naturforschung A*, vol. 23, pp. 2135–2136, 12 1968.

[4] A. Otto, "Excitation of nonradiative surface plasma waves in silver by the method of frustrated total reflection," *Zeitschrift für Physik A Hadrons and nuclei*, vol. 216, pp. 398–410, 8 1968.

[5] H. Raether, *Surface Plasmons on Smooth and Rough Surfaces and on Gratings, Vol. 111 of Springer Tracts in Modern Physics*. Berlin: Springer, 1988.

[6] J. Reguera, J. Langer, D. Jiménez De Aberasturi, and L. M. Liz-Marzán, "Anisotropic metal nanoparticles for surface enhanced Raman scattering," *Chemical Society Review*, vol. 46, no. 13, pp. 3866–3885, 2017.

[7] D. Cialla, A. März, R. Böhme, F. Theil, K. Weber, M. Schmitt, and J. Popp, "Surface-enhanced Raman spectroscopy (SERS): progress and trends," *Analytical and Bioanalytical Chemistry*, vol. 403, pp. 27–54, 4 2012.

[8] K. A. Willets, "Supercharging superlocalization microscopy: how electrochemical charging of plasmonic nanostructures uncovers hidden heterogeneity," *ACS Nano*, vol. 13, pp. 6145–6150, 6 2019.

[9] M. E. Stewart, C. R. Anderton, L. B. Thompson, J. Maria, S. K. Gray, J. A. Rogers, and R. G. Nuzzo, "Nanostructured plasmonic sensors," *Chemical Reviews*, vol. 108, pp. 494–521, 2 2008.

[10] E. C. Le Ru and P. G. Etchegoin, "Single-molecule surface-enhanced Raman spectroscopy," *Annual Review of Physical Chemistry*, vol. 63, pp. 65–87, 5 2012.

[11] P. Verma, "Tip-enhanced Raman spectroscopy: Technique and recent advances," *Chemical Reviews*, vol. 117, pp. 6447–6466, 5 2017.

[12] K. Aydin, V. E. Ferry, R. M. Briggs, and H. A. Atwater, "Broadband polarization-independent resonant light absorption using ultrathin plasmonic super absorbers," *Nature Communications*, vol. 2, p. 517, 2011.

[13] W. J. Padilla, D. N. Basov, and D. R. Smith, "Negative refractive index metamaterials," *Materials Today*, vol. 9, pp. 28–35, 7 2006.

[14] D. Vestler, I. Shishkin, E. A. Gurvitz, M. E. Nasir, A. Ben-Moshe, A. P. Slobozhanyuk, A. V. Krasavin, T. Levi-Belenkova, A. S. Shalin, P. Ginzburg, G. Markovich, and A. V. Zayats, "Circular dichroism enhancement in plasmonic nanorod metamaterials," *Optics Express*, vol. 26, p. 17841, 7 2018.

[15] N. M. Litchinitser, "Nonlinear optics in metamaterials," *Advances in Physics: X*, vol. 3, p. 1367628, 1 2018.

[16] Z.-Y. Yang, S. Ishii, T. Yokoyama, T. D. Dao, M.-G. Sun, P. S. Pankin, I. V. Timofeev, T. Nagao, and K.-P. Chen, "Narrowband wavelength selective thermal emitters by confined Tamm plasmon polaritons," *ACS Photonics*, vol. 4, pp. 2212–2219, 9 2017.

[17] K. Manthiram and A. P. Alivisatos, "Tunable localized surface plasmon resonances in tungsten oxide nanocrystals," *Journal of the American Chemical Society*,

vol. 134, no. 9, pp. 3995–3998, 2012.

[18] U. Guler, V. M. Shalaev, and A. Boltasseva, "Nanoparticle plasmonics: Going practical with transition metal nitrides," *Materials Today*, vol. 18, no. 4, pp. 227–237, 2015.

[19] M. Kumar, N. Umezawa, S. Ishii, and T. Nagao, "Examining the performance of refractory conductive ceramics as plasmonic materials: A theoretical approach," *ACS Photonics*, vol. 3, pp. 43–50, 1 2016.

[20] S. Link and M. A. El-Sayed, "Shape and size dependence of radiative, non-radiative and photothermal properties of gold nanocrystals," *International Reviews in Physical Chemistry*, vol. 19, pp. 409–453, 7 2000.

[21] A. Doughty, A. Hoover, E. Layton, C. Murray, E. Howard, and W. Chen, "Nanomaterial applications in photothermal therapy for cancer," *Materials*, vol. 12, p. 779, 3 2019.

[22] R. S. Riley and E. S. Day, "Gold nanoparticle-mediated photothermal therapy: applications and opportunities for multimodal cancer treatment," *Wiley Interdisciplinary Reviews: Nanomedicine and Nanobiotechnology*, vol. 9, no. 4, 2017.

[23] X. Huang and M. A. El-Sayed, "Gold nanoparticles: Optical properties and implementations in cancer diagnosis and photothermal therapy," *Journal of Advanced Research*, vol. 1, no. 1, pp. 13–28, 2010.

[24] S. Wu and M. T. Sheldon, "Optical power conversion via tunneling of plasmonic hot carriers," *ACS Photonics*, vol. 5, pp. 2516–2523, 6 2018.

[25] K. W. Mauser, S. Kim, S. Mitrovic, D. Fleischman, R. Pala, K. C. Schwab, and H. A. Atwater, "Resonant thermoelectric nanophotonics," *Nature Nanotechnology*, vol. 12, pp. 770–775, 8 2017.

[26] M. Thirugnanasambandam, S. Iniyan, and R. Goic, "A review of solar thermal technologies," *Renewable and Sustainable Energy Reviews*, vol. 14, pp. 312–322, 1 2010.

[27] J.-J. Greffet, P. Bouchon, G. Brucoli, and F. Marquier, "Light emission by nonequilibrium bodies: Local Kirchhoff law," *Physical Review X*, vol. 8, p. 021008, 4 2018.

[28] P. K. Jain and L. K. Sharma, "The physics of blackbody radiation: A review," *Journal of Applied Science in Southern Africa*, vol. 4, 2 1998.

[29] G. V. Hartland, "Optical studies of dynamics in noble metal nanostructures," *Chemical Reviews*, vol. 111, pp. 3858–3887, 6 2011.

[30] X. Li, D. Xiao, and Z. Zhang, "Landau damping of quantum plasmons in metal nanostructures," *New Journal of Physics*, vol. 15, p. 023011, 2 2013.

[31] J. B. Khurgin, "How to deal with the loss in plasmonics and metamaterials," *Nature Nanotechnology*, vol. 10, pp. 2–6, 1 2015.

[32] L. Jiang and H.-L. Tsai, "Improved two-temperature model and its application in ultrashort laser heating of metal films," *Journal of Heat Transfer*, vol. 127, pp. 1167–1173, 10 2005.

[33] X. Xie and D. G. Cahill, "Thermometry of plasmonic nanostructures by anti-Stokes electronic Raman scattering," *Applied Physics Letters*, vol. 109, p. 183104, 10 2016.

[34] J. T. Hugall and J. J. Baumberg, "Demonstrating photoluminescence from Au is electronic inelastic light Scattering of a plasmonic metal: The origin of SERS backgrounds," *Nano Letters*, vol. 15, pp. 2600–2604, 4 2015.

[35] O. Neumann, A. S. Urban, J. Day, S. Lal, P. Nordlander, and N. J. Halas, "Solar vapor generation enabled by nanoparticles," *ACS Nano*, vol. 7, pp. 42–49, 1 2013.

[36] L. V. Besteiro, P. Yu, Z. Wang, A. W. Holleitner, G. V. Hartland, G. P. Wiederrecht, and A. O. Govorov, "The fast and the furious: Ultrafast hot electrons in plasmonic metastructures. Size and structure matter," *Nano Today*, vol. 27, pp. 120–145, 8 2019.

[37] J. L. Brooks, C. L. Warkentin, D. Saha, E. L. Keller, and R. R. Frontiera, "Toward a mechanistic understanding of plasmon-mediated photocatalysis," *Nanophotonics*, vol. 7, no. 11, pp. 1697–1724, 2018.

[38] J. Yang, Y. Guo, W. Lu, R. Jiang, and J. Wang, "Emerging applications of plasmons in driving CO 2 reduction and N 2 fixation," *Advanced Materials*, vol. 30, p. 1802227, 11 2018.

[39] D. F. Swearer, H. Zhao, L. Zhou, C. Zhang, H. Robatjazi, J. M. P. Martirez, C. M. Krauter, S. Yazdi, M. J. McClain, E. Ringe, E. A. Carter, P. Nordlander, and N. J. Halas, "Heterometallic antennareactor complexes for photocatalysis," *Proceedings of the National Academy of Sciences*, vol. 113, pp. 8916–8920, 8 2016.

[40] C.-K. Sun, F. Vallée, L. H. Acioli, E. P. Ippen, and J. G. Fujimoto, "Femtosecond-tunable measurement of electron thermalization in gold," *Physical Review B*, vol. 50, pp. 15337–15348, 11 1994.

[41] G. Della Valle, M. Conforti, S. Longhi, G. Cerullo, and D. Brida, "Real-time optical mapping of the dynamics of nonthermal electrons in thin gold films," *Physical Review B*, vol. 86, p. 155139, 10 2012.

[42] G. Della Valle, F. Scotognella, A. R. S. Kandada, M. Zavelani-Rossi, H. Li, M. Conforti, S. Longhi, L. Manna, G. Lanzani, and F. Tassone, "Ultrafast optical mapping of nonlinear plasmon dynamics in Cu2– x Se nanoparticles," *The Journal of Physical Chemistry Letters*, vol. 4, pp. 3337–3344, 10 2013.

[43] L. Guo and X. Xu, "Ultrafast spectroscopy of electron-phonon coupling in gold," *Journal of Heat Transfer*, vol. 136, pp. 1–6, 12 2014.

[44] K. Wu, J. Chen, J. R. McBride, and T. Lian, "Efficient hot-electron transfer by a plasmon-induced interfacial charge-transfer transition," *Science*, vol. 349, pp. 632–635, 8 2015.

[45] W. Shockley and H. J. Queisser, "Detailed balance limit of efficiency of p-n junction solar cells," *Journal of Applied Physics*, vol. 32, pp. 510–519, 3 1961.

[46] P. Bermel, J. Lee, J. D. Joannopoulos, I. Celanovic, and M. Soljacie, "Selective solar absorbers," *Annual Review of Heat Transfer*, vol. 15, no. 15, pp. 231–254, 2012.

[47] C. M. Lampert, "Coatings for enhanced photothermal energy collection II. Non-selective and energy control films," *Solar Energy Materials*, vol. 2, pp. 1–17, 9 1979.

[48] A. Donnadieu and B. O. Seraphin, "Optical performance of absorber-reflector combinations for photothermal solar energy conversion," *Journal of the Optical Society of America*, vol. 68, p. 292, 3 1978.

[49] A. Narayanaswamy and G. Chen, "Thermal emission control with one-dimensional metallodielectric photonic crystals," *Physical Review B*, vol. 70, p. 125101, 9 2004.

[50] A. Narayanaswamy, "1D Metallo-dielectric photonic crystals as selective emitters for thermophotovoltaic applications," *AIP Conference Proceedings*, vol. 738, no. 2004, pp. 215–220, 2004.

[51] X.-F. Li, Y.-R. Chen, J. Miao, P. Zhou, Y.-X. Zheng, L.-Y. Chen, and Y.-P. Lee, "High solar absorption of a multilayered thin film structure," *Optics Express*, vol. 15, p. 1907, 2 2007.

[52] J. C. C. Fan and S. A. Spura, "Selective black absorbers using rf-sputtered Cr2O3/Cr cermet films," *Applied Physics Letters*, vol. 30, pp. 511–513, 5 1977.

[53] C. M. Lampert and J. Washburn, "Microstructure of a black chrome solar selective absorber," *Solar Energy Materials*, vol. 1, pp. 81–92, 2 1979.

[54] H. Sai, Y. Kanamori, K. Hane, and H. Yugami, "Numerical study on spectral properties of tungsten one-dimensional surface-relief gratings for spectrally selective devices," *Journal of the Optical Society of America A*, vol. 22, p. 1805, 9 2005.

[55] A. Heinzel, V. Boerner, A. Gombert, B. Bläsi, V. Wittwer, and J. Luther, "Radiation filters and emitters for the NIR based on periodically structured metal surfaces," *Journal of Modern Optics*, vol. 47, pp. 2399–2419, 11 2000.

[56] J. Wang, Z. Chen, and D. Li, "Simulation of two-dimensional Mo photonic crystal surface for high-temperature solar-selective absorber," *Physica Status Solidi (a)*, vol. 207, pp. 1988–1992, 8 2010.

[57] C.-H. Chang, J. A. Dominguez-Caballero, H. J. Choi, and G. Barbastathis, "Nanostructured gradient-index antireflection diffractive optics," *Optics Letters*, vol. 36, p. 2354, 6 2011.

[58] A. Ghobadi, H. Hajian, M. Gokbayrak, S. A. Dereshgi, A. Toprak, B. Butun, and E. Ozbay, "Visible light nearly perfect absorber: An optimum unit cell arrangement for near absolute polarization insensitivity," *Optics Express*, vol. 25, p. 27624, 10 2017.

[59] S. Anu Mary Ealia and M. P. Saravanakumar, "A review on the classification, characterisation, synthesis of nanoparticles and their application," *IOP Conference Series: Materials Science and Engineering*, vol. 263, p. 032019, 11 2017.

[60] P. B. Johnson and R. W. Christy, "Optical constants of the noble metals," *Physical Review B*, vol. 6, no. 12, pp. 4370–4379, 1972.

[61] E. Palik, *Handbook of Optical Constants: Volume I*. Elsevier, 1997.

[62] M. A. Green, *Third Generation Photovoltaics: Advanced Solar Energy Conversion*. New York: Springer Berlin Heidelberg, 2003.

[63] W. Li and S. Fan, "Nanophotonic control of thermal radiation for energy applications," *Optics Express*, vol. 26, p. 15995, 6 2018.

[64] D. Costantini, A. Lefebvre, A.-L. Coutrot, I. Moldovan-Doyen, J.-P. Hugonin, S. Boutami, F. Marquier, H. Benisty, and J.-J. Greffet, "Plasmonic metasurface for directional and frequency-selective thermal emission," *Physical Review Applied*, vol. 4, p. 014023, 7 2015.

[65] P. Yu, L. V. Besteiro, Y. Huang, J. Wu, L. Fu, H. H. Tan, C. Jagadish, G. P. Wiederrecht, A. O. Govorov, and Z. Wang, "Broadband metamaterial absorbers," *Advanced Optical Materials*, vol. 7, p. 1800995, 2 2019.

[66] M. Najiminaini, F. Vasefi, B. Kaminska, and J. J. L. Carson, "Experimental and numerical analysis on the optical resonance transmission properties of nano-hole arrays," *Optics Express*, vol. 18, p. 22255, 10 2010.

[67] K. Bae, G. Kang, S. K. Cho, W. Park, K. Kim, and W. J. Padilla, "Flexible thin-film black gold membranes with ultrabroadband plasmonic nanofocusing for efficient solar vapour generation," *Nature Communications*, vol. 6, p. 10103, 12 2015.

[68] L. Li, L. Sun, J. S. Gomez-Diaz, N. L. Hogan, P. Lu, F. Khatkhatay, W. Zhang, J. Jian, J. Huang, Q. Su, M. Fan, C. Jacob, J. Li, X. Zhang, Q. Jia, M. Sheldon, A. Alù, X. Li, and H. Wang, "Self-assembled epitaxial Au–oxide vertically aligned

nanocomposites for nanoscale metamaterials," *Nano Letters*, vol. 16, pp. 3936–3943, 6 2016.

[69] J. Huang, X. Wang, N. L. Hogan, S. Wu, P. Lu, Z. Fan, Y. Dai, B. Zeng, R. Starko-Bowes, J. Jian, H. Wang, L. Li, R. P. Prasankumar, D. Yarotski, M. Sheldon, H.-T. Chen, Z. Jacob, X. Zhang, and H. Wang, "Nanoscale artificial plasmonic lattice in self-assembled vertically aligned nitride-metal hybrid metamaterials," *Advanced Science*, vol. 5, p. 1800416, 7 2018.

[70] X. Xiang, C. Yang, Y. Zhang, Z. Peng, Z. Cao, H. Zhao, P. Zhang, and L. Xuan, "Experimental realization of hyperbolic dispersion metamaterial for the whole visible spectrum based on liquid crystalline phase soft template," *Optics Express*, vol. 23, p. 21343, 8 2015.

[71] K. Ito, Y. Yamada, A. Miura, and H. Iizuka, "High-aspect-ratio mushroom-like silica nanopillars immersed in air: epsilon-near-zero metamaterials mediated by a phonon-polaritonic anisotropy," *RSC Advances*, vol. 9, no. 29, pp. 16431–16438, 2019.

[72] R. Verre, M. Svedendahl, N. O. Länk, Z. J. Yang, G. Zengin, T. J. Antosiewicz, and M. Käll, "Directional light extinction and emission in a metasurface of tilted plasmonic nanopillars," *Nano Letters*, vol. 16, pp. 98–104, 1 2016.

[73] J. Sambles, "An electron microscope study of evaporating small particles: The Kelvin equation for liquid lead and the mean surface energy of solid silver," *Proceedings of the Royal Society of London. A. Mathematical and Physical Sciences*, vol. 318, pp. 507–522, 9 1970.

[74] L.-G. Wang, G.-X. Li, and S.-Y. Zhu, "Thermal emission from layered structures containing a negative-zero-positive index metamaterial," *Physical Review B*, vol. 81, p. 073105, 2 2010.

[75] J. H. Park, S. E. Han, P. Nagpal, and D. J. Norris, "Observation of thermal beaming from tungsten and molybdenum bull's eyes," *ACS Photonics*, vol. 3, pp. 494–500, 3 2016.

[76] N. Jaziri, A. Boughamoura, J. Müller, B. Mezghani, F. Tounsi, and M. Ismail, "A comprehensive review of Thermoelectric Generators: Technologies and common applications," *Energy Reports*, 12 2019.

[77] A. Balčytis, M. Ryu, S. Juodkazis, and J. Morikawa, "Micro-thermocouple on nanomembrane: thermometer for nanoscale measurements," *Scientific Reports*, vol. 8, p. 6324, 12 2018.

[78] S. Sadat, A. Tan, Y. J. Chua, and P. Reddy, "Nanoscale thermometry using point contact thermocouples," *Nano Letters*, vol. 10, pp. 2613–2617, 7 2010.

[79] G. P. Szakmany, A. O. Orlov, G. H. Bernstein, and W. Porod, "Single-metal nanoscale thermocouples," *IEEE Transactions on Nanotechnology*, vol. 13, pp. 1234–1239, 11 2014.

[80] M. N. Getz, O. Nilsen, and P.-A. Hansen, "Sensors for optical thermometry based on luminescence from layered YVO4: Ln3+ (Ln = Nd, Sm, Eu, Dy, Ho, Er, Tm, Yb) thin films made by atomic layer deposition," *Scientific Reports*, vol. 9, p. 10247, 12 2019.

[81] R. G. Geitenbeek, J. C. Vollenbroek, H. M. H. Weijgertze, C. B. M. Tregouet, A.-E. Nieuwelink, C. L. Kennedy, B. M. Weckhuysen, D. Lohse, A. van Blaaderen, A. van den Berg, M. Odijk, and A. Meijerink, "Luminescence thermometry for in situ temperature measurements in microfluidic devices," *Lab on a Chip*, vol. 19, no. 7, pp. 1236–1246, 2019.

[82] S. Wang, S. Westcott, and W. Chen, "Nanoparticle luminescence thermometry," *Journal of Physical Chemistry B*, vol. 106, no. 43, pp. 11203–11209, 2002.

[83] M. G. Nikolic, M. S. Rabasovic, J. Krizan, S. Savic-Sevic, M. D. Rabasovic, B. P. Marinkovic, A. Vlasic, and D. Sevic, "Luminescence thermometry using Gd2Zr2O7:Eu3+," *Optical and Quantum Electronics*, vol. 50, p. 258, 6 2018.

[84] C. Colliex, "Taking temperature at the nanoscale," *Science*, vol. 347, pp. 611–612, 2 2015.

[85] M. Mecklenburg, W. A. Hubbard, E. R. White, R. Dhall, S. B. Cronin, S. Aloni, and B. C. Regan, "Nanoscale temperature mapping in operating microelectronic devices," *Science*, vol. 347, pp. 629–632, 2 2015.

[86] N. N. Jarenwattananon, S. Glöggler, T. Otto, A. Melkonian, W. Morris, S. R. Burt, O. M. Yaghi, and L.-S. Bouchard, "Thermal maps of gases in heterogeneous reactions," *Nature*, vol. 502, pp. 537–540, 10 2013.

[87] X. Wu and R. Hull, "A novel nano-scale non-contact temperature measurement technique for crystalline materials," *Nanotechnology*, vol. 23, p. 465707, 11 2012.

[88] T. Yamaguchi, M. Ohkubo, N. Ikeda, and T. Nomura, "Measurement of semiconductor surface temperature using Raman spectroscopy," *Furukawa Review*, pp. 73–77, 1999.

[89] J. Huang, W. Wang, C. J. Murphy, and D. G. Cahill, "Resonant secondary light emission from plasmonic Au nanostructures at high electron temperatures created by pulsed-laser excitation," *Proceedings of the National Academy of Sciences*, vol. 111, pp. 906–911, 1 2014.

[90] A. Carattino, M. Caldarola, and M. Orrit, "Gold nanoparticles as absolute nanothermometers," *Nano Letters*, vol. 18, pp. 874–880, 2 2018.

[91] W. Farm, R. Storz, H. Tom, and J. Bokor, "Direct measurement of nonequilibrium electron-energy distributions in sub-picosecond laser-heated gold films," *Surface Science*, vol. 283, pp. 221–225, 3 1993.

[92] J. Hohlfeld, S.-S. Wellershoff, J. Güdde, U. Conrad, V. Jähnke, and E. Matthias, "Electron and lattice dynamics following optical excitation of metals," *Chemical Physics*, vol. 251, pp. 237–258, 1 2000.

[93] R. Groeneveld, R. Sprik, and A. Lagendijk, "Ultrafast relaxation of electrons probed by surface plasmons at a thin silver film," *Physical Review Letters*, vol. 64, pp. 784–787, 2 1990.

[94] S. S. Wellershoff, J. Hohlfeld, J. Güdde, and E. Matthias, "The role of electron-phonon coupling in femtosecond laser damage of metals," *Applied Physics A: Materials Science and Processing*, vol. 69, no. 7, 1999.

[95] J. Szczerbiński, L. Gyr, J. Kaeslin, and R. Zenobi, "Plasmon-driven photocatalysis leads to products known from E-beam and X-ray-induced surface chemistry," *Nano Letters*, vol. 18, pp. 6740–6749, 11 2018.

[96] Y.-Y. Cai, E. Sung, R. Zhang, L. J. Tauzin, J. G. Liu, B. Ostovar, Y. Zhang, W.-S. Chang, P. Nordlander, and S. Link, "Anti-Stokes emission from hot carriers in gold nanorods," *Nano Letters*, vol. 19, pp. 1067–1073, 2 2019.

[97] N. SINGH, "Two-temperature model of nonequilibrium electron relaxation: A review," *International Journal of Modern Physics B*, vol. 24, pp. 1141–1158, 4 2010.

[98] K. F. Domke, D. Zhang, and B. Pettinger, "Enhanced Raman spectroscopy: Single molecules or carbon?," *The Journal of Physical Chemistry C*, vol. 111, pp. 8611–8616, 6 2007.

[99] B. Foerster, A. Joplin, K. Kaefer, S. Celiksoy, S. Link, and C. Sönnichsen, "Chemical interface damping depends on electrons reaching the surface," *ACS Nano*, vol. 11, no. 3, pp. 2886–2893, 2017.

[100] A. J. Therrien, M. J. Kale, L. Yuan, C. Zhang, N. J. Halas, and P. Christopher, "Impact of chemical interface damping on surface plasmon dephasing," *Faraday Discussions*, vol. 214, pp. 59–72, 2019.

[101] A. M. Brown, R. Sundararaman, P. Narang, W. A. Goddard, and H. A. Atwater, "Ab initio phonon coupling and optical response of hot electrons in plasmonic metals," *Physical Review B*, vol. 94, p. 075120, 8 2016.

[102] F. Hanke and J. Björk, "Structure and local reactivity of the Au(111) surface reconstruction," *Physical Review B*, vol. 87, p. 235422, 6 2013.

[103] C. Bauer, J.-P. Abid, and H. H. Girault, "Size dependence investigations of hot electron cooling dynamics in metal/adsorbates nanoparticles," *Chemical Physics*, vol. 319, pp. 409–421, 12 2005.

[104] J. L. Hostetler, A. N. Smith, D. M. Czajkowsky, and P. M. Norris, "Measurement of the electron-phonon coupling factor dependence on film thickness and grain size in Au, Cr, and Al," *Applied Optics*, vol. 38, p. 3614, 6 1999.

[105] D. Jaque, L. Martínez Maestro, B. del Rosal, P. Haro-Gonzalez, A. Benayas, J. L. Plaza, E. Martín Rodríguez, and J. García Solé, "Nanoparticles for photothermal therapies," *Nanoscale*, vol. 6, no. 16, pp. 9494–9530, 2014.

[106] R. R. Ford and J. Pritchard, "Work functions of gold and silver films," *Transactions of the Faraday Society*, vol. 67, p. 216, 1971.

[107] G. Hatsopoulos and E. Gyftopoulos, *Thermionic Energy Conversion, Volume 2 :Theory, Technology, and Application*. Cambridge, U.K.: MIT Press, 1979.

[108] S. Linic, P. Christopher, and D. B. Ingram, "Plasmonic-metal nanostructures for efficient conversion of solar to chemical energy," *Nature Materials*, vol. 10, no. 12, pp. 911–921, 2011.

[109] M. W. Knight, H. Sobhani, P. Nordlander, and N. J. Halas, "Photodetection with active optical antennas," *Science*, vol. 332, pp. 702–704, 5 2011.

[110] P. Nordlander, L. Henderson, H. Robatjazi, L. Dong, E. A. Carter, C. Zhang, D. F. Swearer, N. J. Halas, L. Zhou, H. Zhao, and P. Christopher, "Quantifying hot carrier and thermal contributions in plasmonic photocatalysis," *Science*, vol. 362, no. 6410, pp. 69–72, 2018.

[111] S. Mukherjee, F. Libisch, N. Large, O. Neumann, L. V. Brown, J. Cheng, J. B. Lassiter, E. A. Carter, P. Nordlander, and N. J. Halas, "Hot electrons do the impossible: Plasmon-induced dissociation of H 2 on Au," *Nano Letters*, vol. 13, pp. 240–247, 1 2013.

[112] J. G. Liu, H. Zhang, S. Link, and P. Nordlander, "Relaxation of plasmon-induced hot carriers," *ACS Photonics*, vol. 5, pp. 2584–2595, 7 2018.

[113] L. Shen, G. N. Gibson, N. Poudel, B. Hou, J. Chen, H. Shi, E. Guignon, N. C. Cady, W. D. Page, A. Pilar, and S. B. Cronin, "Plasmon resonant amplification of hot electron-driven photocatalysis," *Applied Physics Letters*, vol. 113, no. 11, 2018.

[114] P. Christopher, H. Xin, and S. Linic, "Visible-light-enhanced catalytic oxidation reactions on plasmonic silver nanostructures," *Nature Chemistry*, vol. 3, no. 6, pp. 467–472, 2011.

[115] W. Xie and S. Schlücker, "Hot electron-induced reduction of small molecules on photorecycling metal surfaces," *Nature Communications*, vol. 6, no. May, pp. 1–6, 2015.

[116] A. Marimuthu, J. Zhang, and S. Linic, "Tuning selectivity in propylene epoxidation by plasmon mediated photo-switching of Cu oxidation state," *Science*, vol. 340, no. 6127, pp. 1590–1593, 2013.

[117] J. S. DuChene, G. Tagliabue, A. J. Welch, W.-H. Cheng, and H. A. Atwater, "Hot hole collection and photoelectrochemical CO 2 reduction with plasmonic Au/p-GaN photocathodes," *Nano Letters*, vol. 18, pp. 2545–2550, 4 2018.

[118] S. Yu, A. J. Wilson, J. Heo, and P. K. Jain, "Plasmonic control of multi-electron transfer and C–C coupling in visible-light-driven CO2 reduction on Au nanoparticles," *Nano Letters*, vol. 18, pp. 2189–2194, 4 2018.

[119] J. Lee, S. Mubeen, X. Ji, G. D. Stucky, and M. Moskovits, "Plasmonic photoanodes for solar water splitting with visible light," *Nano Letters*, vol. 12, no. 9, pp. 5014–5019, 2012.

[120] S. Mubeen, J. Lee, N. Singh, S. Krämer, G. D. Stucky, and M. Moskovits, "An autonomous photosynthetic device in which all charge carriers derive from surface plasmons," *Nature Nanotechnology*, vol. 8, no. 4, pp. 247–251, 2013.

[121] M. Thangamuthu, C. Santschi, and O. J. Martin, "Photocatalytic ammonia production enhanced by a plasmonic near-field and hot electrons originating from aluminium nanostructures," *Faraday Discussions*, vol. 214, pp. 399–415, 2019.

[122] G. H. Chan, J. Zhao, E. M. Hicks, G. C. Schatz, and R. P. Van Duyne, "Plasmonic properties of copper nanoparticles fabricated by nanosphere lithography," *Nano Letters*, vol. 7, no. 7, pp. 1947–1952, 2007.

[123] I. Fabijanić, V. Janicki, J. Ferré-Borrull, M. Bubaš, V. B. Bregović, L. F. Marsal, and J. Sancho-Parramon, "Plasmonic nanoparticles and Island films for solar energy

harvesting: A comparative study of Cu, Al, Ag and Au performance," *Coatings*, vol. 9, no. 6, 2019.

[124] J. Wu, Y. Huang, W. Ye, and Y. Li, "CO2 reduction: From the electrochemical to photochemical approach," *Advanced Science*, vol. 4, p. 1700194, 11 2017.

[125] G. Xiao, G. Zheng, M. Qiu, Q. Li, D. Li, and M. Ni, "Thermionic energy conversion for concentrating solar power," *Applied Energy*, vol. 208, pp. 1318–1342, 12 2017.

[126] J. Huang, Z. Xu, and Y. Yang, "Low-work-function surface formed by solution-processed and thermally deposited nanoscale layers of cesium carbonate," *Advanced Functional Materials*, vol. 17, pp. 1966–1973, 8 2007.

[127] K. A. Abdul Khalid, T. J. Leong, and K. Mohamed, "Review on thermionic energy converters," *IEEE Transactions on Electron Devices*, vol. 63, pp. 2231–2241, 6 2016.

[128] L. Debbichi, M. C. Marco de Lucas, J. F. Pierson, and P. Krüger, "Vibrational properties of CuO and Cu4O3 from first-principles calculations, and Raman and infrared spectroscopy," *The Journal of Physical Chemistry C*, vol. 116, pp. 10232–10237, 5 2012.

[129] T. Vasileiadis, L. Waldecker, D. Foster, A. Da Silva, D. Zahn, R. Bertoni, R. E. Palmer, and R. Ernstorfer, "Ultrafast heat flow in heterostructures of Au nanoclusters on thin films: Atomic disorder induced by hot electrons," *ACS Nano*, vol. 12, no. 8, pp. 7710–7720, 2018.

[130] C. D. Geddes, A. Parfenov, I. Gryczynski, and J. R. Lakowicz, "Luminescent blinking from silver nanostructures," *The Journal of Physical Chemistry B*, vol. 107, pp. 9989–9993, 9 2003.

[131] N. Nedyalkov, A. Dikovska, M. Koleva, N. Stankova, R. Nikov, E. Borisova, T. Genova, L. Aleksandrov, R. Iordanova, and M. Terakawa, "Luminescence properties of laser-induced silver clusters in borosilicate glass," *Optical Materials*, vol. 100, p. 109618, 2 2020.

[132] X. Meng, J. Dyer, Y. Huo, and C. Jiang, "Greater SERS activity of ligand-stabilized gold nanostars with sharp branches," *Langmuir*, vol. 36, pp. 3558–3564, 4 2020.

[133] C. G. Khoury and T. Vo-Dinh, "Gold nanostars for surface-enhanced Raman scattering: Synthesis, characterization and optimization," *The Journal of Physical Chemistry C*, vol. 112, pp. 18849–18859, 12 2008.

APPENDIX A

MIE THEORY CALCULATIONS

What follows is the full Matlab code for estimating the temperature increase of a spherical metal nanoparticle using Mie theory as described in Chapter 2. The code was run in Matlab 2018a.

```
function [ sph_yn ] = sph_yn(nmax,z)
%Spherical bessel Y function
sph_yn = zeros(1, nmax+1);

a = (pi/2/z) ^.5;

for k=0:nmax
    sph_yn(k+1) = bessely(k+.5,z) * a;
end

function [ sph_jn ] = sph_jn(nmax,z)
%Spherical bessel J function
sph_jn = zeros(1, nmax+1);

a = (pi/2/z) ^.5;

for k=0:nmax
    sph_jn(k+1) = besselj(k+.5,z) * a;
end

function [Qabs, sigma_abs] = mie_abs(r,wavelength_array, ...
```

```
    n_medium, n_relative)
%Caclulates mie theory absorbance efficiency and
%absorbtion cross section for a given radius (r),
%wavelength range (wavelength_array), refractive
%index of the medium (n_medium), and complex relative
%refractive index of the particle (n_relative).


nmax = 5;

%zero array section
Qscat = zeros(1,length(wavelength_array));
Qabs = zeros(1,length(wavelength_array));
Qext = zeros(1, length(wavelength_array));


for k=1:length(wavelength_array)
    wavelength = wavelength_array(k);

    x = (2 * pi * r * n_medium) / wavelength;   %size parameter
    mx = x * n_relative(k);
    m = n_relative(k);  %relative refractive index

    n = 1:nmax;

    jn_0_all = sph_jn(nmax, x);
    jn_0 = jn_0_all(2:end);
    jn_0_1 = jn_0_all(1:(end-1));

    yn_0_all = sph_yn(nmax,x);
    yn_0 = yn_0_all(2:end);
```

```
52      yn_0_1 = yn_0_all(1:(end-1));
53
54      jn_1_all = sph_jn(nmax, mx);
55      jn_1 = jn_1_all(2:end);
56      jn_1_1 = jn_1_all(1:(end-1));
57
58      hn_0 = jn_0 + 1j.*yn_0;
59      hn_1 = jn_0_1 + 1j.*yn_0_1;
60
61      jn_0_d = x.*jn_0_1 - n.*jn_0;
62      jn_1_d = mx.*jn_1_1 - n.*jn_1;
63      hn_0_d = x.*hn_1 - n.*hn_0;
64
65      a = (m^2.*jn_1.*jn_0_d - jn_0.*jn_1_d)./(m^2.*jn_1.*hn_0_d - ...
            hn_0.*jn_1_d);
66      b = (jn_1.*jn_0_d - jn_0.*jn_1_d)./(jn_1.*hn_0_d - ...
            hn_0.*jn_1_d);
67
68      Qscat(k) = (2/x^2)*sum((2*n+1).*(abs(a).^2 + abs(b).^2));
69      Qext(k) = (2/x^2)*sum((2*n+1).*real(a+b));
70      Qabs(k) = Qext(k) - Qscat(k);
71  end
72
73  sigma_abs = Qabs.*(pi*r^2);
74  end
75
76
77  element = 'aluminum';   %picks element:gold, silver, aluminum, ...
        copper
78  n_medium = 1;   %refrac index of the medium: water=1.330, vacuum=1
79  T_ambient = 298;    %ambient temp (room temp) in K
```

```
80
81 wavelength_array = linspace(280,2500,1000);   %range of ...
       wavelengths probed
82 r_array = linspace(5,150,25); %picks the radius of the particles
83
84 %loads solar spectrum and interp it to the right wavelengths
85 load('sun_spectrum_AM15Global');
86 sun_wavelength_all = sun_spectrum(:,1);
87 sun_irradiance_all = sun_spectrum(:,2);
88 sun_irradiance = interp1(sun_wavelength_all, sun_irradiance_all, ...
       wavelength_array, 'spline');
89
90 %pre-set empty arrays
91 e=zeros(1,length(wavelength_array));
92 n_particle = zeros(1,length(wavelength_array));
93 n_relative = zeros(1,length(wavelength_array));
94 temp_array = zeros(1,length(r_array));
95
96 %refractive index calculation
97 %loads in the experimental refractive index and saves it for later
98 %calculations depending on the element
99 if strcmpi(element, 'gold')
100     %johnson and christy data
101         load('JC_data_gold');
102         nr = data(:,2);
103         ni = data(:,3);
104         wavelengths = data(:,1);
105         re = interp1(wavelengths, nr, wavelength_array, 'spline');
106         img = interp1(wavelengths, ni, wavelength_array, 'spline');
107         for k=1:length(wavelength_array)
108             n_particle(k) = complex(re(k), img(k));
```

```
109         end
110 elseif strcmpi(element, 'silver')
111     %palik data
112         load('palik_data_silver');
113         nr = data(:,2);
114         ni = data(:,3);
115         wavelengths = data(:,1);
116         re = interp1(wavelengths, nr, wavelength_array, 'spline');
117         img = interp1(wavelengths, ni, wavelength_array, 'spline');
118         for k=1:length(wavelength_array)
119             n_particle(k) = complex(re(k), img(k));
120         end
121 elseif strcmpi(element, 'aluminum')
122     %palik data
123         load('palik_data_aluminum');
124         nr = data(:,2);
125         ni = data(:,3);
126         wavelengths = data(:,1);
127         re = interp1(wavelengths, nr, wavelength_array, 'spline');
128         img = interp1(wavelengths, ni, wavelength_array, 'spline');
129         for k = 1:length(wavelength_array)
130             n_particle(k) = complex(re(k), img(k));
131         end
132 elseif strcmpi(element, 'copper')
133     %palik data
134         load('palik_data_copper');
135         nr = data(:,2);
136         ni = data(:,3);
137         wavelengths = data(:,1);
138         re = interp1(wavelengths, nr, wavelength_array, 'spline');
139         img = interp1(wavelengths, ni, wavelength_array, 'spline');
```

```
140         for k = 1:length(wavelength_array)
141             n_particle(k) = complex(re(k), img(k));
142         end
143 end
144
145 %define relative refractive index
146 for k=1:length(wavelength_array)
147     n_relative(k) = n_particle(k) / n_medium;
148 end
149
150 %define average emissivity
151 if strcmpi(element, 'gold')
152     emissivity = .02;
153 elseif strcmpi(element, 'silver')
154     emissivity = .02;
155 elseif strcmpi(element, 'copper')
156     emissivity = .04;
157 elseif strcmpi(element, 'aluminum')
158     emissivity = .03;
159 end
160
161 %For every radius calculate the absorption cross section and ...
       temperature
162 for k=1:length(r_array)
163     r = r_array(k);
164
165     %Calculate absorption cross section
166     [Qabs, sigma_abs] = mie_abs(r,wavelength_array, n_medium, ...
           n_relative);
167
168     %Calculate power absorbed
```

```
169     power = trapz(wavelength_array, sigma_abs.*sun_irradiance);
170
171     %Calculate temperature
172     temp_array(k) = ((power + ...
            4*pi*r^2*5.67e-8*emissivity*T_ambient^4)./ ...
            (4*pi*r^2*5.67e-8*emissivity)).^.25;
173 end
174
175 %Plot the results
176     hold on
177     plot(r_array, temp_array)
178     xlabel('Radius in nm')
179     ylabel('Temperature in K')
180 end
```

APPENDIX B

CALCULATION OF TEMPERATURE FROM EMISSIVITY

What follows is the full Matlab code for calculating the temperature of a surface given a specific angular and wavelength dependent emissivity function as defined in Figures 2.2 and 2.3. The code was run in Matlab 2018a.

```
function [T_surface] = ...
    temp_calc(cutoff_wavelength,cutoff_angle,Δ_1,Δ_2,gamma_1,gamma_2)
%Calculates the temperature of a surface based on the following ...
    parameters:
%cutoff_wavelength in nm
%cutoff_angle in degrees
%Δ_1 >> deviation from one emissivity at small wavelengths
%Δ_2 >> deviation from zero emissivity and high wavelengths
%gamma_1 >> deviation from one emissivity at small angles
%gamma_2 >> deviation from zero emissivity at high angles

T_amb = 298; %ambient temperature around particle
l_nm = linspace(280,100000,10000); %defines wavelengths of ...
    analysis in nm
l_m = l_nm.*1e-9; %saves wavelengths in m units
cutoff_angle_upper_value = 90; %limits analysis to hemispherical ...
    emission

%Angular Integration
    %transforms into radius
    cutoff_angle = cutoff_angle.*(pi/180);
```

```
18      cutoff_angle_upper_value = cutoff_angle_upper_value.*(pi/180);
19
20      %inegrates over angle theta
21      fun = @(x) abs(cos(x).*sin(x));
22      q = integral(fun,0, cutoff_angle);
23      q2 = integral(fun,cutoff_angle,cutoff_angle_upper_value);
24
25      %scales by emissivity and the phi integration
26      angle_factor_amb = 2*pi*q*(1-gamma_1) + 2*pi*q2*gamma_2;
27      angle_factor_emit = 2*pi*q*(1-gamma_1) + 2*pi*q2*gamma_2;
28
29  %Loading in solar spectrum
30      %loads in solar spectrum already angle corrected and all that
31      load('sun_spectrum_AM15Global');
32
33      %AM1.5 Spectrum is only measured to 4000 nm, so the rest of the
34      %spectrum is approximated as a blackbody at 5770
35      l_bb_nm = linspace(4005,l_nm(end),1000);
36      bb_approx = blackbody_spectrum(l_bb_nm.*1e-9,5770) ...
            *pi*sind(.26)^2.*1e-9;
37      l_sun = [sun_spectrum(:,1)', l_bb_nm];
38      I_sun = [sun_spectrum(:,2)', bb_approx];
39
40      %interps to the right wavelengths
41      sun_approx = interp1(l_sun,I_sun,l_nm); %W/m^2/nm
42
43  %Define emissivity in the wavelength dimension
44      %define zero array
45      emissivity = zeros(1, length(l_nm));
46
47      %Pick the specific cutoff from the cutoff array
```

```
48      cutoff_l = cutoff_wavelength; %nm
49
50      %Loop over every wavelength in the range to define emissivity
51      for k=1:length(l_nm)
52          l = l_nm(k); %pick wavelength
53          index = l-cutoff_l; %find the difference of the ...
                wavelength from the cutoff
54          a = heaviside(index);
55          if a>.4 %If heaviside returned 1 (l greater than cutoff) ...
                set emissivity to zero
56              emissivity(k) = a_2;
57          else %If heaviside returned 0 (l less than cutoff) set ...
                emissivity to one
58              emissivity(k) = (1-a_1);
59          end
60      end
61
62      %Kirchoff's law
63      absorbtivity = emissivity;
64
65  %Calculate power absorbed
66      %Correct intensity absorbed by multiplying by absorbtivity
67      sun_approx = sun_approx.*absorbtivity.*gamma_2; %W/m^2/nm
68
69      %Integrate to get power
70      P_sun = trapz(l_nm, sun_approx); %W/m^2
71
72      %Define ambient power absorbed from the surface being at 298 K;
73      I_amb = blackbody_spectrum(l_m, ...
            T_amb).*absorbtivity.*angle_factor_amb; %W/m^3
74
```

```
75      %Integrate to get power
76      P_amb = trapz(l_m, I_amb); %W/m^2
77
78      %Total absorbed power is power from the sun plus power from ...
            ambient
79      P_abs = P_sun + P_amb; %W/m^2
80
81  %Calculate temperature
82      %define initial temperature guess
83      T = 300; %K
84
85      %calculate blackbody spectra
86      I = blackbody_spectrum(l_m, T); %W/m^3/sr
87
88      %multiply bb spectrum by emissivity to get real spectrum
89      I = I.*emissivity; %W/m^3/sr
90
91      %multiply by correct angle factor
92      I = I.*angle_factor_emit; %W/m^3
93
94      %integrate to get power emitted
95      P_emit = trapz(l_m, I); %W/m^2
96
97      %Loop until correct temperature is found
98      tolerance = .00001;
99      iteration=0;
100     while (P_emit < P_abs-P_abs*tolerance) || (P_emit > ...
            P_abs+P_abs*tolerance)
101          if iteration > 20000 %keeps it from going infinetly just ...
                in case
102              break
```

```
103         end
104         iteration = iteration+1;
105
106         if (P_emit < P_abs-P_abs*tolerance)
107             T = T*1.001;
108         elseif (P_emit > P_abs+P_abs*tolerance)
109             T = T*.999;
110         end
111
112         %calculate blackbody spectra
113         I = blackbody_spectrum(l_m, T); %W/m^3/sr
114
115         %multiply bb spectrum by emissivity to get real spectrum
116         I = I.*emissivity; %W/m^3/sr
117
118         %multiply by correct angle factor
119         I=I.*angle_factor_emit; %W/m^3
120
121         %integrate to get power emitted
122         P_emit = trapz(l_m, I); %W/m^2
123     end
124 T_surface = T;
125 end
```

APPENDIX C

FITTING THE ANTI-STOKES RAMAN SPECTRA

What follows is the full Matlab code for fitting the anti-Stokes Raman spectra from a metal film as described in Chapter 3. The code was run in Matlab 2018a.

```
clear;
close all;


%% Import data

%In the workspace there needs to be a experimental data named:
% l >> wavelength in inv cm (correspondingly l_inv_cm in inv cm ...
    and l_nm in nm)
% all_data >> all of the data that is already divided by ...
    integration time and background corrected
% power_array >> all of the powers in W

%l_reflection >> wavelength data for Reflection spectrum in nm
%R >> Reflection spectrum

%% Setting Fit Parameters

smooth_data = 0; %True False for smoothing the experimental data
meta_analysis = 0; %True False for running an analysis to avoid ...
    local minima during fitting
one_temp_model = 0; %True False for running a one temp model ...
```

```
    instead of two temp
20
21 %Fitting range:
22 %Either over one range, or over two ranges that correspond to ...
    cutting out a
23 %section in the middle of the data to avoid the amorphous carbon ...
    peaks
24 min_wavenumber_1 = 500; %inv cm
25 max_wavenumber_1 = 3250; %inv cm
26
27 fitting_two_ranges = 0;
28 min_wavenumber_2 = 1800; %inv cm
29 max_wavenumber_2 = 3500; %inv cm
30
31 %% Interp data and define constants for math
32
33 %changing up graphing color presets for graphing
34     set(0,'DefaultAxesColorOrder',jet(length(power_array)))
35
36 %sort data to be in increasing power order and convert power to ...
    mW and
37 %calculates power density
38     [power_array, order] = sort(power_array);
39     power_array = power_array*1e3;
40     all_data = all_data(:,order);
41     power_density = power_array./1e3./(pi*(0.8e-6)^2);
42
43 %save unnormalized data for math later
44     all_data_raw = all_data;
45
46 %power normalize the data
```

```
47      for i = 1:length(power_array)
48          all_data(:,i) = all_data(:,i)./power_array(i);
49      end
50
51  %% Calculate the Stokes:anti-Stokes ratio
52
53  %pick the possible stokes to antistokes region
54      if abs(l(1)) > abs(l(end)) %pick which one is smaller
55          endpoint = round(abs(l(end)), -1) - 10; %round the ...
                smaller one to ten and subtract 10 just in case it ...
                rounded up
56      else
57          endpoint = round(abs(l(1)), -1) - 10;
58      end
59
60  %define the interpolation wavenumber arrays
61      l_interp = -endpoint:10:endpoint; %wavenumber in rel. inv cm
62      l_inv_cm_interp = l_interp + laser_inv_cm; %wavenumber in ...
            inv cm
63
64  %pick the stokes and antistokes region
65      stokes_length = floor(length(l_interp)/2); %Half the length ...
            of l_interp not counting zero
66      l_stokes = fliplr(l_interp(1:stokes_length)); %in rel. inv cm
67      l_antistokes = l_interp(stokes_length+2:end); %in rel. inv cm
68      l_stokes_inv_cm = l_stokes + laser_inv_cm; %in inv cm
69      l_antistokes_inv_cm = l_antistokes + laser_inv_cm; % in inv cm
70
71  %interp the stokes and antistokes regions
72      all_data_stokes = zeros(length(l_stokes),length(power_array));
73      all_data_antistokes = ...
```

```
        zeros(length(l_antistokes),length(power_array));
    for i = 1:length(power_array)
        all_data_stokes(:,i) = interp1(l,all_data(:,i),l_stokes);
        all_data_antistokes(:,i) = ...
            interp1(l,all_data(:,i),l_antistokes);
    end

%calculate stokes:antistokes ratio
    stokes_antistokes_ratio = all_data_stokes./all_data_antistokes;

%function used if fitting one temp model ratiometrically
%     ambient_temp = 25;
%     func = @(T,omega)((exp(-1*h*c*omega/k/(ambient_temp+273))-1)./
%                   ... (exp(-1*h*c*omega/k/(T+273))-1));


%% Define DOS

%Interp the wavelengths to wavenumber regions
    l_reflection_nm = l_reflection; %saves data in nm for later ...
        graphing
    l_reflection_inv_cm = 1e7./l_reflection; %Goes from nm to ...
        inv cm
    l_reflection = l_reflection_inv_cm - laser_inv_cm; ...
        %wavenumber in rel. inv cm
    R = smooth(smooth(smooth(R))); %smooth the reflection data ...
        to get rid of some noise

%Calculate the DOS (A for the  S:AS ratio, alpha for absolute) ...
    by interping refleciton
    A_stokes = interp1(l_reflection,R,l_stokes);
```

```
98      A_antistokes = interp1(l_reflection,R,l_antistokes);
99
100     A = A_stokes./A_antistokes;
101
102     alpha = interp1(l_reflection,R,l);
103
104 %% Define equations
105
106 %Constants
107     h = 6.626e-34; %m^2 * kg / sec
108     c = 3e8; %m / s
109     k = 1.38e-23; %m^2 * kg / sec^2 / K
110
111 %Set is so fit routine doesn't spam the command line
112     opts = optimset('Display','off');
113
114 %Four equations
115
116 %Anti-stokes phononic
117     %This is a bose einstein
118     AS_p = @(T,l) (1./(exp(h*c*(l-laser_inv_cm*100)/k/T)-1)); ...
            %for T in K and l in inv m
119     %This is a boltzmann
120 %     AS_p = @(T,l) exp(-h*c*(l-laser_inv_cm*100)/k/T); %for T ...
        in K and l in inv m
121
122 %Stokes phononic
123     %This is a bose einstein with the sign flipped so there is ...
            positives
124     %and also plus one at the end
125     S_p = @(T,l) (1./(exp(h*c*(l-laser_inv_cm*100)/k/T)-1)) + 1; ...
```

```
        %for T in K and l in inv m
126
127 %Anti-stokes electronic
128     %This is just a boltzmann
129 %     AS_e = @(T,l) exp(-h*c*(l-laser_inv_cm*100)/k/T); %for T ...
        in K and l in inv m
130     %This is a fermi dirac
131     AS_e = @(T,l) (1./(exp(h*c*(l-laser_inv_cm*100)/k/T)+1)); ...
            %for T in K and l in inv m
132
133 %Stokes electronic
134     %This is just one
135     S_e = @(T,l) ones(1,length(l));
136
137
138 %% Fitting only the anti-stokes side of the spectrum
139
140 %Smooth the data or not?
141 if smooth_data == 1
142     for i = 1:length(power_array)
143         all_data(:,i) = smooth(smooth(all_data(:,i)));
144     end
145 end
146
147
148
149 %Set wavenumber region to fit over using parameters set in beginning
150     range_1 = [];
151     range_2 = [];
152
153     [¬, index_min] = min(abs(l-(min_wavenumber_1)));
```

```
154     [¬, index_max] = min(abs(l-(max_wavenumber_1)));
155     range_1 = index_max:index_min;
156
157 if fitting_two_ranges ==1
158     [¬, index_min] = min(abs(l-(min_wavenumber_2)));
159     [¬, index_max] = min(abs(l-(max_wavenumber_2)));
160     range_2 = index_max:index_min;
161 end
162
163     range = [range_2,range_1];
164
165 %Adjust DOS to the right length
166     if length(alpha)≠1
167         alpha = alpha(range);
168     end
169
170 %Prevent NaN by making sure both the log and the log^2 of the ...
      data isn't zero
171     all_data(all_data==0)=0.001;
172
173 %Function for fitting to the log squared of the data
174     T0 = [298 500 0.5 1]; %tp te chi C
175     func = @(T,l) log10(abs(log10(T(4)*alpha.* ...
          ((1-T(3)).*(AS_p(T(1),l)) + T(3).*(AS_e(T(2),l))))));
176     func_graphing = @(T,l) log10(T(4)*alpha.* ...
          ((1-T(3)).*(AS_p(T(1),l)) + T(3).*(AS_e(T(2),l))));
177     if one_temp_model == 1 %forces chi to zero which means ...
          electronic temperature term is zero
178         lower_bound = [273, 273, 0, 0];
179         upper_bound = [5e3, 1e5, 0, 1e10];
180     else
```

```
181          lower_bound = [273, 273, 0, 0];
182          upper_bound = [5e3, 1e5, 0.5, 1e10];
183      end
184
185  %fitting
186      calc_temp_array = zeros(length(T0),length(power_array));
187      for i = 0:(length(power_array)-1) %Done in high to lower ...
             power order due to an old fitting strategy, makes no ...
             difference
188          calc_temp_array(:,end-i) = lsqcurvefit(func, T0, ...
                 l_inv_cm(range)*100, ...
                 log10(abs(log10(all_data(range,end-i)))), ...
                 lower_bound, upper_bound,opts);
189      end
190
191  %% Graphing AS side of spectrum
192
193      if meta_analysis == 0 %if meta analysis wasn't run
194
195          figure('unit', 'normalized','Position', [0 0 0.7 0.7]) ...
                 %in normalized values, left bottom width height
196
197          subplot(2,4,[1,4])
198              hold on
199              for i = 1:length(power_array) %plots experimental data
200                  plot(l(range), ...
                         real(squeeze(log10(all_data(range,i)))), ...
                         '*-', 'linewidth', 0.5, 'markersize', 3)
201              end
202
203              for i = 1:length(power_array) %plots the fits
```

```
204                 plot(l(range),func_graphing(calc_temp_array(:,i), ...
                        l_inv_cm(range)*100), '--', 'linewidth',2)
205             end
206
207             xlabel('Rel. wavenumbers (cm^-^1)');
208             ylabel('Log(Antistokes counts)');
209             hold off;
210
211         subplot(2,4,5)
212             plot(power_array,calc_temp_array(1,:), '*-')
213             xlabel('Applied power (mW)')
214             ylabel('T_p')
215         subplot(2,4,6)
216             plot(power_array,calc_temp_array(2,:), '*-')
217             xlabel('Applied power (mW)')
218             ylabel('T_e')
219         subplot(2,4,7)
220             plot(power_array,calc_temp_array(3,:), '*-')
221             xlabel('Applied power (mW)')
222             ylabel('\chi')
223         subplot(2,4,8)
224             plot(power_array,calc_temp_array(4,:), '*-')
225             xlabel('Applied power (mW)')
226             ylabel('Scaling factor')
227     end
228
229 %% Meta analysis for AS side of spectrum
230
231     if meta_analysis == 1
232
233         calc_temp_no_meta = calc_temp_array;
```

```
234
235         %Set the range of initial guesses for each variable to test
236         scale_factor = 1;
237         temporary_loop = linspace(273,3000,6); %T_p
238         temporary_loop_2 = logspace(2.45,9,6); %T_e
239         temporary_loop_3 = logspace(-5,0,6); %chi
240
241         %Create zero arrays
242         calc_best_array = zeros(length(power_array), length(T0));
243         residual_best_array = zeros(1, length(power_array));
244         calc_temp_array = zeros(length(power_array), ...
                length(temporary_loop), length(temporary_loop_2), ...
                length(temporary_loop_3), length(T0));
245         residual_array = zeros(length(power_array), ...
                length(temporary_loop), length(temporary_loop_2), ...
                length(temporary_loop_3));
246
247         for i = 0:(length(power_array)-1)
248
249             %loops over ever set of initial gueses and solves ...
                   for temp at each point
250             for j = 1:length(temporary_loop)
251                 for k = 1:length(temporary_loop_2)
252                     for m = 1:length(temporary_loop_3)
253                         %prints where you are in the loops to ...
                               keep track of progress
254                         iteration = [i,j,k,m]
255
256                         %sets the initial guess and runs fitting ...
                               routine
257                         T0 = [temporary_loop(j), ...
```

```
                        temporary_loop_2(k), ...
                        temporary_loop_3(m), scale_factor];
258                     [a, b] = lsqcurvefit(func, T0, ...
                        l_inv_cm(range)*100, ...
                        log10(abs(log10(all_data(range,end-i)))), ...
                        lower_bound, upper_bound,opts);
259
260                     %Save results to pull out of the loops
261                     calc_temp_array(end-i,j,k,m,:) = a;
262                     residual_array(end-i,j,k,m) = b;
263
264
265                 end
266             end
267         end
268
269         %solves for the absolute minimum residual from every ...
            initial
270         %guess set and saves it
271         temporary = squeeze(residual_array(end-i,:,:,:));
272         [a,b] = min(squeeze(temporary(:)));
273         residual_best_array(end-i) = a;
274
275         %uses the position of the best fit in order to also ...
            pull out
276         %the fit parameter solved for when minimum residual ...
            was found
277         [bj,bk,bm] = ind2sub(size(temporary),b);
278         b = squeeze(calc_temp_array(end-i,bj,bk,bm,:));
279
280         %saves for pulling out of loop
```

```
281             calc_best_array(end-i,:) = b;
282
283         end
284
285     %Graphs the AS data from the meta analysis
286
287         figure('unit', 'normalized','Position', [0 0 0.7 0.7]) ...
                %in normalized values, left bottom width height
288
289         subplot(2,4,[1,4])
290             hold on
291             for i = 1:length(power_array) %plots the ...
                    experimental data
292                 plot(l(range), ...
                        real(squeeze(log10(all_data(range,i)))),  ...
                        '*-', 'linewidth', 0.5, 'markersize', 3)
293             end
294
295             for i = 1:length(power_array) %plots the best fits
296                 plot(l(range), ...
                        func_graphing(calc_best_array(i,:), ...
                        l_inv_cm(range)*100), '--', 'linewidth',2)
297             end
298
299             xlabel('Rel. wavenumbers (cm^-^1)');
300             ylabel('Stokes:Antistokes ratio');
301             hold off;
302
303         subplot(2,4,5)
304             plot(power_array,calc_best_array(:,1), '*-')
305             xlabel('Applied power (mW)')
```

```
306             ylabel('T_p')
307             set(gca,'xscale','log')
308         subplot(2,4,6)
309             plot(power_array,calc_best_array(:,2), '*-')
310             xlabel('Applied power (mW)')
311             ylabel('T_e')
312             set(gca,'xscale','log')
313         subplot(2,4,7)
314             plot(power_array,calc_best_array(:,3), '*-')
315             xlabel('Applied power (mW)')
316             ylabel('Fraction of hot electrons')
317             set(gca,'xscale','log')
318         subplot(2,4,8)
319             plot(power_array,calc_best_array(:,4), '*-')
320             xlabel('Applied power (mW)')
321             ylabel('Scaling Factor')
322             set(gca,'xscale','log')
323
324     end %end of the meta analysis
```